FABRICATION AND ANALYSIS OF MULTILAYER STRUCTURES FOR COHERENT THERMAL EMISSION

A Dissertation
Presented to
The Academic Faculty

by

Bong Jae Lee

In Partial Fulfillment
of the Requirements for the Degree of
Doctor of Philosophy in the
George W. Woodruff School of Mechanical Engineering

Georgia Institute of Technology
December 2007

FABRICATION AND ANALYSIS OF MULTILAYER STRUCTURES FOR COHERENT THERMAL EMISSION

Approved by:

Dr. Zhuomin Zhang, Advisor
George W. Woodruff School of Mechanical Engineering
Georgia Institute of Technology

Dr. David S. Citrin
School of Electrical and Computer Engineering
Georgia Institute of Technology

Dr. Samuel Graham
George W. Woodruff School of Mechanical Engineering
Georgia Institute of Technology

Dr. Benjamin K. Tsai
Optical Technology Division, Physics Laboratory
National Institute of Standards and Technology

Dr. Peter J. Hesketh
George W. Woodruff School of Mechanical Engineering
Georgia Institute of Technology

Date Approved: October 12, 2007

ACKNOWLEDGEMENTS

I would like to express my wholehearted appreciation to my advisor, Dr. Zhuomin Zhang, for his endless support, encouragement, and guidance during my Ph.D. study. His invaluable advice and constructive suggestions have motivated me to further improve myself and excel in my research. I would also like to thank Dr. Benjamin Tsai (my supervisor during the summer internship program) of the National Institute of Standards and Technology (NIST) for his continuous support and willingness to serve as a committee member. In addition, I want to thank my other dissertation committee members, Dr. Peter Hesketh, Dr. Samuel Graham, and Dr. David Citrin, for sharing their breadth of expertise and knowledge.

The late Professor David DeWitt deserves a special thank for his encouragement during my internship at NIST and his collaboration and support on my earlier work. I also thank Dr. Leonard Hanssen and Dr. Edward Early of NIST for sharing their expertise in spectroscopy.

Much appreciation is expressed to all my former and current colleagues. I am grateful to Dr. Ceji Fu for his invaluable suggestions in the surface polariton research, and Dr. Hyunjin Lee and Dr. Keunhan Park for their continuous help in research as well as in daily life. Fruitful collaborations with Vinh Khuu, Dr. Yu-bin Chen, Soumyadipta Basu, and Qinghe Li are also appreciated. I also thank Dr. Heungjoo Shin, Dr. Jungchul Lee, and Arnab Choudhury for sharing their experiences in microfabrication.

Finally, I wish to extend my deepest appreciation to my parents, for their great support, dedication, and endless love.

TABLE OF CONTENTS

LIST OF FIGURES

NOMENCLATURE

1D	one dimensional
2D	two dimensional
3D	three dimensional
AFM	atomic force microscope
ATR	attenuated total reflection
BR	Brewster mode
BRDF	bidirectional reflectance distribution function, 1/sr
CR	cavity resonance mode
DNG	double negative
ESL	energy streamline
FDTD	finite-difference time-domain
FIB	focused ion beam
FTIR	Fourier-transform infrared
FWHM	full-width-at-half-minimum (or maximum)
IR	infrared
LO	longitudinal optical
PC	photonic crystal
PECVD	plasma enhanced chemical vapor deposition
SNG	single negative
SW	surface wave
TE	transverse electric

TO	transverse optical
TM	transverse magnetic
A, C	amplitude of forward propagating (or decaying) wave
B, D	amplitude of backward propagating (or decaying) wave
c	speed of light in vacuum, 2.998×10^{8} m/s
$\mathbf{D}$	dynamical matrix
d	layer thickness, m
$\mathbf{E}$	electric field vector, V/m
G	one-dimensional reciprocal lattice vector, 1/m
$\bar{\bar{\mathbf{G}}}_{\mathrm{e}}$	dyadic electric Green's function, $1/\mathrm{m}^2$
$\bar{\bar{\mathbf{G}}}_{\mathrm{m}}$	dyadic magnetic Green's function, 1/m
$\mathbf{H}$	magnetic field vector, A/m
h	Planck constant divided by 2π, 1.055×10^{-34} J s
$\mathbf{I}$	unit matrix
i	$\sqrt{-1}$
j	jth medium
$\mathbf{j}$	electric current density, $\mathrm{A/m}^2$
K	one-dimensional Bloch wavevector, 1/m
$\mathbf{k}$	wavevector, 1/m
k	magnitude of wavevector, 1/m
k_{B}	Boltzmann constant, 1.1381×10^{-23} J / K
k_x, k_y, or k_z	x, y, or z component of wavevector, 1/m

L_{coh}	coherence length, m
N	total number of unit cells in a photonic crystal
N_l	total number of layers
n	refractive index
$\mathbf{P}$	propagation matrix
Q	quality factor
R	spectral-directional reflectance
$\mathbf{r}$	vector in the radial direction, m
$\overline{r}$	Fresnel reflection coefficient
$\mathbf{S}$	Poynting vector, $\mathrm{W\,m^{-2}\,rad\,s^{-1}}$
T	spectral-directional transmittance
t	time, s
$\overline{t}$	Fresnel transmission coefficient
$\mathbf{z}$	vector in the normal direction to surfaces, m

Greek Symbols

β	parallel wavevector component, 1/m
Γ	damping coefficient, 1/m
δ	lateral shift of energy pathways, m
ε	relative electric permittivity
ε_0	electric permittivity of vacuum, 8.854×10^{-12} F/m
ε_∞	relative electric permittivity at high frequency
ε_λ	spectral-hemispherical emissivity
$\varepsilon_{\lambda,\theta}$	spectral-directional emissivity

Θ	mean energy of the Planck oscillator, J
θ	polar angle, rad
θ_{E}	energy propagation angle, rad
$\Delta\theta$	full-width-at-half-minimum (or maximum), rad
κ	extinction coefficient
Λ	period of one-dimensional photonic crystals, m
λ	wavelength in vacuum, m
$\Delta\lambda$	full-width-at-half-minimum (or maximum), m
μ	relative magnetic permeability
μ_0	magnetic permeability of vacuum, $4\pi\times10^{-7}$ N/A^2
ϕ	azimuthal angle in the cylindrical coordinate, rad
ϕ_{ps}	phase shift, 1/m
ν	frequency (or wavenumber), 1/m
ν_{LO}	wavenumber of longitudinal optical phonon, 1/m
$\Delta\nu$	full-width-at-half-minimum (or maximum), 1/m
ω	angular frequency, rad/s

Subscript

c	center
E	energy propagation
H	high-refractive-index layer
L	low-refractive-index layer
p	*p* polarization
s	*s* polarization

SiC	Silicon carbide film
ter	surface termination
x, *y*, or *z*	*x*, *y*, or *z* direction in the Cartesian coordinate

Superscript

inv	inverse
ord	ordinary
*	complex conjugate
+	forward propagating (or decaying) waves
–	backward propagating (or decaying) waves

SUMMARY

Tailoring thermal radiative properties using micro- and nano-structured surfaces has become a new frontier of radiation heat transfer research due to its important applications in energy conversion devices, space thermal management, and infrared radiation detection. A large number of recent publications dealt with enhanced emission properties from surface relief gratings by exciting surface polaritons. The present dissertation describes a comprehensive investigation on the coherent thermal emission from thin-film multilayer structures.

A novel multilayer structure consisting of a one-dimensional photonic crystal and a polar material (or a metal) is proposed as a coherent thermal-emission source. A salient feature of a photonic crystal is the existence of a photonic band gap, where effective evanescent waves exist inside the structure. When the thicknesses and dielectric properties of the photonic crystal are adjusted, surface electromagnetic waves can be excited at the edge of photonic crystal, enabling coherent emission characteristics (i.e., spectral- and directional-selectivity in the emissivity). Based on the modeling results, the coherent emission source is optimally designed for the near-infrared and fabricated using vacuum deposition techniques. Experimental demonstration of coherent emission has been conducted by measuring the spectral reflectance using a Fourier-transform infrared spectrometer as well as the angle-resolved reflectance using a laser scatterometer. Furthermore, the dispersion relation of surface waves at the edge of a photonic crystal is calculated using the supercell method with modified matrix equations. The agreement between the resonance conditions obtained from experiments and the calculated

dispersion relation confirms that surface waves at the photonic crystal-metal interface can be utilized to build coherent thermal-emission sources.

Besides the large enhancement in the far-field emissivity with the use of coherent emission sources, the spectral energy flux can be greatly enhanced via photon tunneling, i.e., the coupling of evanescent waves by placing the emitter and absorber in close proximity. The second part of this dissertation focuses on the energy propagation direction in near-field thermal radiation. The energy streamline method based on the Poynting vector of coupled forward and backward waves is used to investigate photon tunneling phenomenon and its associated lateral shift of light paths. The energy streamline method has been extended to near-field thermal radiation by incorporating the fluctuational electrodynamics. It is shown that the Poynting vector is decoupled for each parallel wavevector component due to the random nature of thermal radiation. The spectral radiative energy travels in infinite directions along curved lines. The present dissertation elucidates the fundamental characteristics of near-field thermal radiation that is important for applications such as near-field optical sensors and energy conversion devices.

CHAPTER 1

INTRODUCTION

Thermal radiation has drawn much attention since several decades ago due to its applications in combustion, furnace, remote sensing, incandescent lamp, and radiometric temperature measurement. In classical radiation theory, thermal emission from a hot object is understood as a surface phenomenon with the radiative property of emissivity to account for real surfaces being different from a blackbody. It has been widely accepted that thermal emission usually exhibits broadband spectrum and quasi-isotropic angular behavior; thus, it is known for being incoherent [1]. However, rapid advancement in technologies of micro/nanofabrication has enabled the control of thermal emission characteristics by modifying surface structures [2-4]. Surface microstructure, whose length scale is comparable to the characteristic wavelength of thermal radiation, can strongly affect the directional behavior of emission due to multiple reflections [5] and diffraction [6,7]. In fact, enhancement of thermal emission and control of its direction are crucial for engineering applications, such as thermophotovoltaic devices [8], radiation filters [9], space thermal management, and infrared radiation detection. Because of the important applications to radiative energy transfer and energy conversion devices, the study of engineered micro/nanostructures with desired thermal emission characteristics has become a new frontier of radiation heat transfer research [10-21].

Coherent thermal emission is manifested by sharp spectral peaks (i.e., temporal coherence) and/or narrow angular lobes in well-defined directions (i.e., spatial coherence). Recently, coherent thermal emission has been demonstrated using gratings made of a

metal [22,23] or a polar material [24] by exciting surface polaritons. Surface polaritons (or surface waves) are electromagnetic waves that propagate along the interface and decay into both media [25]. To excite surface waves from gratings, a magnetic field component parallel to grating grooves is required. Such a magnetic field component exists in one or both of the transverse magnetic (TM) and transverse electric (TE) waves depending on the direction of emission [26]. In the case when the direction of emission is perpendicular to grooves, coherent emission from grating structures is inevitably restricted to TM waves. Metamaterials with a refractive index much less than unity [27] or single negative materials (with alternative negative permittivity and negative permeability layers) [17] have also been proposed as coherent emission sources; however, these materials have not been fabricated for the near-infrared and mid-infrared spectral regions, where thermal radiation is the most important.

Recently, photonic crystals were extensively investigated to control radiative properties for specific applications [15,28-31]. A photonic crystal (PC) is a periodic array of unit cells (i.e., photonic lattices in analog to those in real crystals), which replicate infinitely in one-, two-, or three-dimensions. Analogously to electron movement in crystals [32], electromagnetic wave propagation in PCs should also satisfy the Bloch condition [33]. Similarly, due to the periodicity, a PC exhibits band structures consisting of pass bands and stop bands when the frequency is plotted against the wavevector. In the pass band, for instance, electromagnetic waves can propagate through a PC. In the stop band, however, no energy-carrier waves can exist inside a PC and only an oscillating but evanescently decaying field may exist. The existence of stop bands enables a PC to be used in many optoelectronic devices such as band-pass filters [34] and waveguides [35].

One-dimensional (1D) PCs are usually made of alternating layers with two lossless dielectrics. Since no energy can transmit into the PC in the stop band, the 1D PC composed of several unit cells can be used as an excellent reflector in the resonance cavity [16]. In 1970s, Yeh et al. [36,37] showed that a 1D PC can support a surface wave for both TM and TE waves in the stop band. Since surface waves are non-radiative, an attenuated total reflection (ATR) configuration [25] was employed to excite the surface waves at the interface between a PC and air. Later, Robertson and May [38,39] also performed experiments to demonstrate the existence of surface waves at the edge of 1D PC, considering surface-termination effects. Recently, Gaspar-Armenta and Villa [40] suggested that, if a metallic layer is coated on a 1D PC, surface waves can be directly excited by propagating waves in air, resulting in a sharp reduction in the reflectance. Therefore, the gratingless multilayer structure may be used for constructing coherent thermal sources for both polarizations. Although coherent characteristics of thermal emission can also be found from a two-dimensional (2D) micro-cavity [4,41], a 2D PC [20,21,42], or a three-dimensional (3D) PC made of tungsten [43], the fabrication of these structures is much more complicated than the planar structure.

In addition to the large enhancement on the far-field emissivity with the use of coherent emission sources, for the application in the energy conversion devices the energy transfer can also be enhanced by placing the emitter to the absorber in close proximity. It has been shown that radiative heat transfer in the proximity, comparable to or smaller than the characteristic wavelength, exhibits complex wave features such as interference, photon tunneling, and surface-polariton excitation [44-48]. The photon tunneling phenomenon, also called frustrated total internal reflection, has been known

since Newton's time and was extensively studied by Hall in 1902 [49]. While tunneling can be understood as a class of quantum phenomena, the well-established explanation of photon tunneling in classical wave optics is the coupling of two oppositely decaying evanescent waves [50]. Due to the coupling, the resulting Poynting vector has a nonzero normal component, suggesting that energy transmission between the media is possible as long as the distance of the gap is smaller than the wavelength. Furthermore, if materials support surface polaritons, photon tunneling at the polariton-excitation frequencies dominates the near-field energy transfer due to amplified evanescent waves [11].

Recent studies have shown that the near-field effects can realize emerging technologies, such as superlens [51], sub-wavelength light source [52], and polariton-assisted nanolithography [53]. Particularly, near-field thermal radiation has been intensively investigated for potential applications of a highly sensitive near-field thermal microscopy [54-56] and a near-field thermophotovoltaic energy conversion system [57,58]. To facilitate these applications, it is crucial to determine the near-field energy flow, especially the lateral shift of energy pathways. In the far field, the directional dependence of radiation leaving a surface is well described by the intensity [59]. In the near field, however, the ray optics fails to describe the energy propagation direction because the refraction angle is not readily defined in the real space during photon tunneling. Meanwhile, the lateral shift accompanied with photon tunneling is described as a Goos-Hänchen type of shift due to the phase differences between different incidence angles of a wave packet [60-64]. Another approach is to use numerical simulations such as the finite-difference time-domain (FDTD) method to determine the local field and Poynting vector distributions for a plane wave or Gaussian beam incidence [65-67]. In

most of these studies, however, the coupling between the forward and backward waves was not completely addressed, and further the direction of energy propagation in nanoscale thermal radiation has not been fully understood.

The objective of this dissertation is two-fold: to identify and fabricate a novel multilayer structure with coherent emission characteristics and perform an experimental demonstration, and to gain a fundamental understanding of photon tunneling and near-field thermal radiation. Chapter 2 describes the theoretical background necessary for subsequent chapters, including thin-film optics, Fabry-Pérot resonance cavity, photonic crystals, surface electromagnetic waves, and energy streamline. Chapter 3 presents a theoretical analysis of coherent thermal emission from a multilayer structure made of a SiC film coated on a semi-infinite 1D PC. The conditions that enable a spectral- and directional-selectivity in the calculated emissivity are thoroughly investigated. In Chapter 4, thin-film structures are optimally designed for exhibiting coherent emission in the near-IR and are fabricated for experimental demonstration. Chapter 5 provides a detailed experimental investigation of coherent emission characteristics from the fabricated structure. A Fourier-transform infrared spectrometer and a laser scatterometer are used to measure the spectral and angle-resolved reflectance of the sample, respectively. In Chapter 6, the energy streamline method based on the Poynting vector of coupled plane waves is employed to study photon tunneling with the presence of single-negative or double-negative materials. By using the fluctuational electrodynamics, the energy streamline method is extended to near-field thermal radiation to investigate the lateral shift of energy pathways. Finally, Chapter 7 summarizes conclusions and provides future research recommendations.

CHAPTER 2

THEORETICAL BACKGROUND

This chapter provides a summary of the basic theories relevant to subsequent chapters of this dissertation. Thin-film optics is discussed based on the transfer matrix formulation and employed to the Fabry-Pérot resonator to calculate radiative properties. One-dimensional photonic crystals are introduced, and the basic concept of photonic band gap is explained using the transfer matrix formulation. Surface waves at the edge of photonic crystals and the effect of surface termination are discussed with the use of the supercell method. Furthermore, the net energy flux of electromagnetic waves is explained based on the Poynting vector and the energy streamline is introduced.

Thin-Film Optics and the Fabry-Pérot Resonance Cavity

It has been known that thin films can greatly modify the radiative properties of surfaces, such as reflectance, transmittance, and emissivity. When the thickness of each layer is comparable or less than the wavelength of incident radiation, the wave interference effects inside each layer become important to correctly predict the radiative properties of multilayer structure of thin films. The transfer matrix formulation provides a convenient way to calculate the radiative properties of multilayer structures [10]. For the *j*th medium (refer to Fig. 2.1), the relative electric permittivity (or dielectric function) is ε_j and the relative magnetic permeability is μ_j. For simplicity, each layer is set to be nonmagnetic (i.e., $\mu_j = 1$), such that $\sqrt{\varepsilon_j} = n_j + i\kappa_j$ with n_j being the refractive index and κ_j being the extinction coefficient. The thickness of the *j*th layer is denoted by d_j.

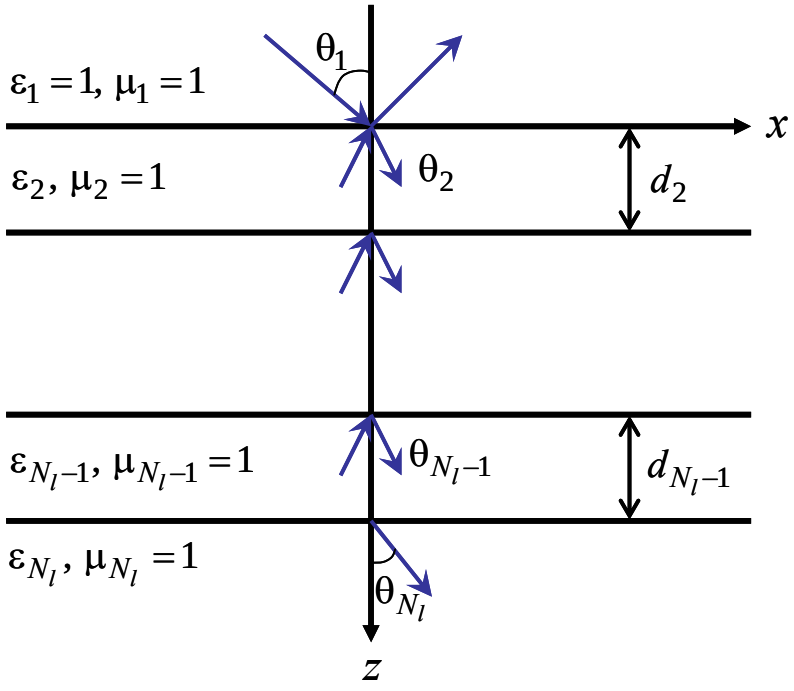

Figure 2.1 The geometry for calculating the radiative properties of a multilayer structure.

It is assumed that $\varepsilon_1 = 1$ (i.e., the top semi-infinite medium is air). For the calculation, the optical properties of air are assumed to be the same as those of vacuum. The electromagnetic wave is incident from the first medium (air) at an angle of incidence θ_1 and is reflected from or transmitted through the following layers. For TE (or *s*-polarized) waves, the *y*-component of electric field in the *j*th medium can be expressed as a summation of forward and backward waves in the *z*-direction:

$$E_y(x,z) = \begin{cases} \left[A_1 e^{ik_{1z}z} + B_1 e^{-k_{1z}z} \right] e^{i(k_x x - \omega t)}, & j = 1 \\ \left[A_j e^{ik_{jz}(z - z_{j-1})} + B_j e^{-k_{jz}(z - z_{j-1})} \right] e^{i(k_x x - \omega t)}, & j = 2, 3, ..., N_l \end{cases} \tag{2.1}$$

where A_j and B_j are the amplitudes of forward and backward waves in the *j*th layer, respectively, $z_1 = 0$ and $z_j = z_{j-1} + d_j \left(j = 2,3,..,N_l - 1 \right)$, ω is the angular frequency, and

k_x and k_{jz} are parallel and perpendicular components of the wavevector, respectively. Notice that k_x is conserved throughout the layers due to the phase-matching condition, and k_{jz} is given by $k_{jz} = \sqrt{(\omega/c)^2 \varepsilon_j - k_x^2}$, where c is the speed of light in vacuum. The magnetic field can be obtained from the electric field using Maxwell's equation. From the boundary conditions at the interface, field amplitudes of adjacent layers can be related as

$$\begin{pmatrix} A_j \\ B_j \end{pmatrix} = (\mathbf{P}_j \mathbf{D}_j^{-1} \mathbf{D}_{j+1}) \begin{pmatrix} A_{j+1} \\ B_{j+1} \end{pmatrix}, \quad j = 1, 2, ..., N_l - 1 \tag{2.2}$$

Here, $\mathbf{P}_j$ is the propagation matrix given by

$$\mathbf{P}_1 = \mathbf{I} = \begin{pmatrix} 1 & 0 \\ 0 & 1 \end{pmatrix} \tag{2.3}$$

and

$$\mathbf{P}_j = \begin{pmatrix} e^{-ik_{jz}d_j} & 0 \\ 0 & e^{ik_{jz}d_j} \end{pmatrix}, \quad j = 2, 3, ..., N_l - 1$$

In addition, $\mathbf{D}_j$ is the dynamical matrix given as

$$\mathbf{D}_j = \begin{pmatrix} 1 & 1 \\ k_{jz}/\mu_j & -k_{jz}/\mu_j \end{pmatrix}, \quad j = 1, 2, ..., N_l \tag{2.4}$$

By applying Eq. (2.2) to all layers, one can obtain

$$\begin{pmatrix} A_1 \\ B_1 \end{pmatrix} = \prod_{j=1}^{N_l - 1} \mathbf{P}_j \mathbf{D}_j^{-1} \mathbf{D}_{j+1} \begin{pmatrix} A_{N_l} \\ B_{N_l} \end{pmatrix} \tag{2.5}$$

Consequently, the spectral radiative properties of the N_l-layer system are obtained by

$$R = \frac{B_1 B_1^*}{A_1^2} \tag{2.6}$$

$$T = \frac{\mathrm{Re}(k_{N_l z} / \mu_{N_l})}{\mathrm{Re}(k_{1z} / \mu_1)} \frac{A_{N_l} A_{N_l}^*}{A_1^2} \tag{2.7}$$

and

$$\varepsilon_{\lambda,\theta} = 1 - R - T \tag{2.8}$$

where R, T, $\varepsilon_{\lambda,\theta}$ represents the spectral-directional reflectance, transmittance, and emissivity, respectively, and asterisk denotes the complex conjugate. For TM (or *p*-polarized) waves, the same procedure can be applied using the magnetic field with μ_j's being replaced by ε_j's.

The Fabry-Pérot resonator usually consists of two parallel mirrors separated by the distance d_2, as shown in Fig. 2.2, and has been employed in several optical devices, such as an interferometer, filter, and laser resonator [68]. The reflection and transmission coefficients at the boundaries of the Fabry-Pérot cavity are also denoted in the figure. Based on Airy's formulae, the reflection and transmission coefficients of the resonance cavity are expressed in the form of a superposition of amplitudes of fields [69,70]:

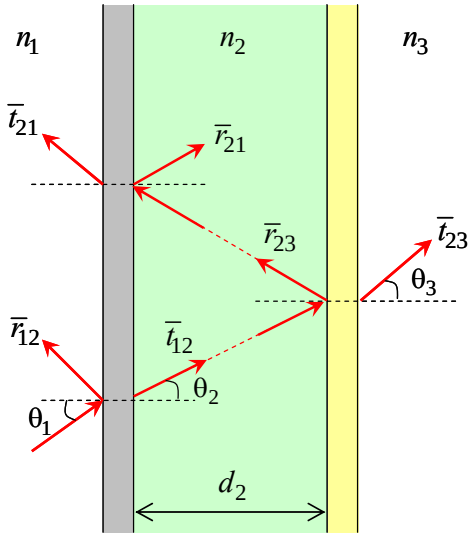

Figure 2.2 Illustration of the Fresnel reflection and transmission coefficients at the boundaries of the Fabry-Pérot resonance cavity.

$$\overline{r} = \overline{r}_{12} + \frac{\overline{t}_{12}\overline{t}_{21}\overline{r}_{23}}{1-\overline{r}_{21}\overline{r}_{23}e^{i2\phi_{ps}}} \tag{2.9}$$

$$\overline{t} = \frac{\overline{t}_{12}\overline{t}_{23}e^{i\phi_{ps}}}{1-\overline{r}_{21}\overline{r}_{23}e^{i2\phi_{ps}}} \tag{2.10}$$

where $\phi_{ps} = 2\pi n_2 d_2 \cos\theta_2 / \lambda$ is the phase shift upon traveling inside the cavity with λ being the wavelength in vacuum. Notice that the reflection and transmission coefficients are defined as the ratios of the electric fields for TE waves and the ratios of the magnetic fields for TM waves, and their expressions are generally different [69]. The spectral reflectance and transmittance of the resonance cavity are calculated from the reflection and transmission coefficients as:

$$R = \overline{r}\,\overline{r}^{*} \tag{2.11}$$

$$T = \frac{\mathrm{Re}(n_1\cos\theta_3)}{\mathrm{Re}(n_3\cos\theta_1)}\overline{t}\,\overline{t}^{*}, \text{ for TM waves} \tag{2.12}$$

$$T = \frac{\mathrm{Re}(n_3\cos\theta_3)}{\mathrm{Re}(n_1\cos\theta_1)}\overline{t}\,\overline{t}^{*}, \text{ for TE waves} \tag{2.13}$$

where n_1 and n_3 are the complex refractive index of the incident and transmitted medium, respectively. Using Eqs. (2.9) and (2.10), the square of the reflection and transmission coefficients can be expressed after simplifications as

$$\overline{r}\,\overline{r}^{*} = \frac{\left(\rho_{12}+\rho_{23}\zeta\right)^2 - 4\rho_{12}\rho_{23}\zeta\sin^2\psi_{\mathrm{I}}}{\left(1-\rho_{12}\rho_{23}\right)^2 + 4\rho_{21}\rho_{23}\sin^2\psi_{\mathrm{II}}} \tag{2.14}$$

$$\overline{t}\,\overline{t}^{*} = \frac{\tau_{12}\tau_{23}}{\left(1-\rho_{12}\rho_{23}\right)^2 + 4\rho_{21}\rho_{23}\sin^2\psi_{\mathrm{II}}} \tag{2.15}$$

where $\rho_{12} = |\bar{r}_{12}|$, $\rho_{21} = |\bar{r}_{21}|$, $\rho_{23} = |\bar{r}_{23}|$, $\zeta = |\bar{t}_{12}\bar{t}_{21} - \bar{r}_{12}\bar{r}_{21}|$, $\tau_{12} = \bar{t}_{12}\bar{t}_{12}^{*}$, $\tau_{23} = \bar{t}_{23}\bar{t}_{23}^{*}$, $\psi_{\mathrm{I}} = (2\phi_{\mathrm{ps}} - \phi_{12} + \phi_{23} + \phi_{\zeta})/2$, $\psi_{\mathrm{II}} = (2\phi_{\mathrm{ps}} + \phi_{21} + \phi_{23})/2$, $\phi_{12} = \arg(\bar{r}_{12})$, $\phi_{21} = \arg(\bar{r}_{21})$, $\phi_{23} = \arg(\bar{r}_{23})$, and $\phi_{\zeta} = \arg(\zeta)$. By examining the denominator of Eq. (2.15), it can be inferred that the maximum T occurs when the following condition is satisfied:

$$2\phi_{\mathrm{ps}} + \phi_{21} + \phi_{23} = 2m\pi \tag{2.16}$$

where m is a positive integer. Here, ϕ_{21} and ϕ_{23} are the phase shifts due to the reflection from the corresponding boundary of the resonance cavity. Consequently, Eq. (2.16) states that the resonance occurs if total phase shifts in the cavity are multiples of 2π, where standing waves form in the cavity.

Fundamentals of Photonic Crystals

While three-dimensional (3D) PCs with complicated structures can be fabricated and used in a number of applications, the fundamental physics can be illustrated using 1D PC and can be easily generalized into two-dimensional (2D) or 3D structures [33]. As illustrated in Fig. 2.3, a 1D PC is a periodic multilayer structure, whose unit cell is composed of alternating dielectrics with different refractive indices. It is assumed that the PC is infinitely extended to the right, and high-refractive-index dielectric starts at $z = 0$. Wave propagation in periodic media is analogous to the motion of electrons in crystalline materials [32]. From such analogy, the electric field vector in the 1D PC for a monochromatic electromagnetic wave of angular frequency ω should satisfy the Bloch condition given by [33]

$$\mathbf{E}(x, y, z, t) = \boldsymbol{u}(z)e^{iKz}e^{i(k_x x + k_y y - \omega t)} \tag{2.17}$$

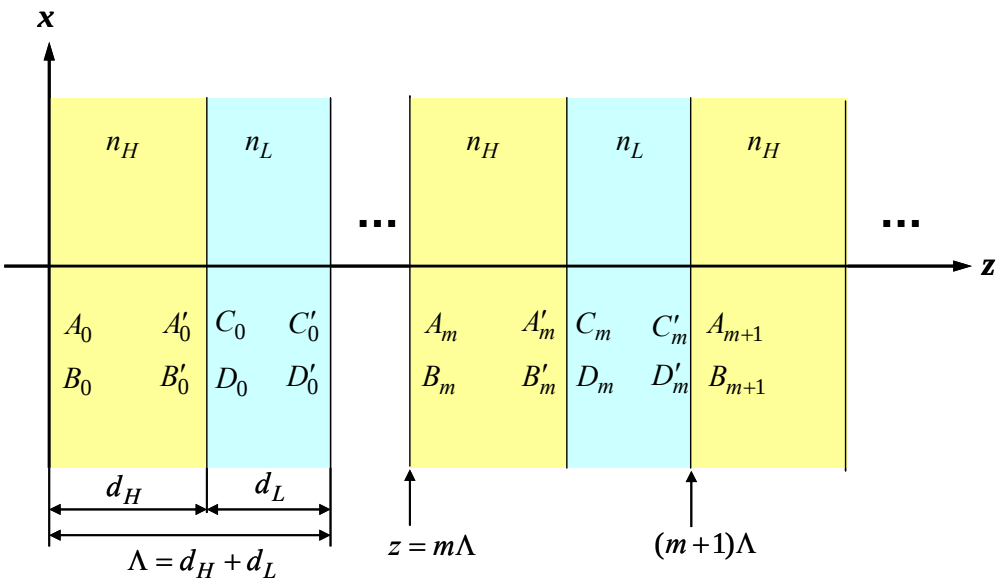

Figure 2.3 Schematic of the amplitudes of forward and backward waves in a semi-infinite 1D PC, in the right half space. The unit cell of the 1D PC is made of two dielectric layers and has a period $\Lambda = d_H + d_L$.

where $\boldsymbol{u}(z+\Lambda) = \boldsymbol{u}(z)$ is a periodic function of z, k_x and k_y are the parallel components of the wavevector and are the same in all layers as required by the phase-matching condition, and K is the magnitude of the Bloch wavevector, which is parallel to the z axis for the 1D PC. Here, K is a characteristic parameter of the PC and is the same for all layers. The wavevector components in the z direction are $k_{z,\mathrm{H}}$ (in high-refractive-index medium) and $k_{z,\mathrm{L}}$ (in low-refractive-index medium), which are determined by $k_x^2 + k_y^2 + k_{z,\mathrm{H}}^2 = n_{\mathrm{H}}^2\omega^2/c^2$ and $k_x^2 + k_y^2 + k_{z,\mathrm{L}}^2 = n_{\mathrm{L}}^2\omega^2/c^2$, respectively. From the Bloch condition, the electric field in the 1D PC satisfies

$$\mathbf{E}(x, y, z+\Lambda, t) = \mathbf{E}(x, y, z, t)e^{iK\Lambda} \tag{2.18}$$

Because of axial symmetry, the coordinate can always be rotated around the z axis to make $k_y = 0$. It is a common practice to analyze the wave propagation for two

separate polarizations. In the case of TE waves, the electric field is perpendicular to the *x*-*z* plane. Therefore, the electric field component in the *y* direction can be expressed as [36]:

$$E_y = \begin{cases} \left[A_m e^{ik_{z,\mathrm{H}}(z-m\Lambda)} + B_m e^{-ik_{z,\mathrm{H}}(z-m\Lambda)} \right] e^{ik_x x}, & m\Lambda \le z \le \left(m\Lambda + d_{\mathrm{H}}\right) \\ \left[C_m e^{ik_{z,\mathrm{L}}(z-m\Lambda-d_{\mathrm{H}})} + D_m e^{-ik_{z,\mathrm{L}}(z-m\Lambda-d_{\mathrm{H}})} \right] e^{ik_x x}, & \left(m\Lambda + d_{\mathrm{H}}\right) \le z \le (m+1)\Lambda \end{cases} \tag{2.19}$$

where the time dependence term $\exp(-i\omega t)$ is omitted for simplicity, m is a nonnegative integer, A_m and C_m are the amplitudes of forward waves, and B_m and D_m are those of backward waves at the interfaces, as shown in Fig. 2.3. Due to phase shifts from wave propagation through the medium, the amplitudes at the other interface of the corresponding layer are $A'_m = e^{ik_{z,\mathrm{H}}d_{\mathrm{H}}} A_m$, $B'_m = e^{-ik_{z,\mathrm{H}}d_{\mathrm{H}}} B_m$, $C'_m = e^{ik_{z,\mathrm{L}}d_{\mathrm{L}}} C_m$, and $D'_m = e^{-ik_{z,\mathrm{L}}d_{\mathrm{L}}} D_m$. Boundary conditions require that the tangential components of the electric and magnetic fields (E_y and H_x) be continuous at each interface. The coefficients A_m and B_m at $z = m\Lambda$ are related to those at $z = (m+1)\Lambda$ via the propagation matrix (**P**) and dynamical matrix (**D**):

$$\begin{pmatrix} A_m \\ B_m \end{pmatrix} = (\mathbf{P}_{\mathrm{H}}\mathbf{D}_{\mathrm{H}}^{-1}\mathbf{D}_{\mathrm{L}})(\mathbf{P}_{\mathrm{L}}\mathbf{D}_{\mathrm{L}}^{-1}\mathbf{D}_{\mathrm{H}}) \begin{pmatrix} A_{m+1} \\ B_{m+1} \end{pmatrix} \tag{2.20}$$

From Eq. (2.18), the ratio of the electric fields at two points separated by a period Λ along the z direction is equal to $\exp(iK\Lambda)$, thus

$$\begin{pmatrix} A_{m+1} \\ B_{m+1} \end{pmatrix} = e^{iK\Lambda} \begin{pmatrix} A_m \\ B_m \end{pmatrix} \tag{2.21}$$

The Bloch wavevector parameter K can be obtained by solving the eigenvalue equation:

$$\mathbf{M} \begin{pmatrix} A_{m+1} \\ B_{m+1} \end{pmatrix} = e^{-iK\Lambda} \begin{pmatrix} A_{m+1} \\ B_{m+1} \end{pmatrix} \tag{2.22}$$

where $\mathbf{M} = (\mathbf{P}_{\mathrm{H}}\mathbf{D}_{\mathrm{H}}^{-1}\mathbf{D}_{\mathrm{L}})(\mathbf{P}_{\mathrm{L}}\mathbf{D}_{\mathrm{L}}^{-1}\mathbf{D}_{\mathrm{H}})$. In general, K depends on the frequency ω and the parallel wavevector component k_x for a given geometry and refractive indices of constituent dielectrics.

Once K is determined, the electric field in the PC can be expressed in the Bloch wave form:

$$E_y(x,z) = u(z)\exp(iKz)\exp(ik_x x) \tag{2.23}$$

In the above equation,

$$u(z) = \left[A_0 e^{ik_{z,\mathrm{H}}(z-m\Lambda)} + B_0 e^{-ik_{z,\mathrm{H}}(z-m\Lambda)} \right] e^{-iK(z-m\Lambda)} \tag{2.24}$$

for $m\Lambda \le z \le (m\Lambda + d_{\mathrm{H}})$, where A_0 and B_0 are amplitudes of the first layer at $z = 0$ and

$$u(z) = \left[C_0 e^{ik_{z,\mathrm{L}}(z-m\Lambda-d_{\mathrm{H}})} + D_0 e^{-ik_{z,\mathrm{L}}(z-m\Lambda-d_{\mathrm{H}})} \right] e^{-iK(z-m\Lambda)} \tag{2.25}$$

for $(m\Lambda + d_{\mathrm{H}}) \le z \le (m+1)\Lambda$, where

$$\begin{pmatrix} C_0 \\ D_0 \end{pmatrix} = \left(\mathbf{P}_{\mathrm{H}}\mathbf{D}_{\mathrm{H}}^{-1}\mathbf{D}_{\mathrm{L}} \right)^{-1} \begin{pmatrix} A_0 \\ B_0 \end{pmatrix} \tag{2.26}$$

Obviously, $u(z)$ is a periodic function of z.

The expressions for the magnetic field can be obtained from the electric field using Maxwell's equations. For TM waves, the magnetic field is parallel to the y axis. The same procedure can be used to determine the magnetic field first and then the electric field [33,69,70]. The amplitudes A_0 and B_0 depend on the boundary condition at $z = 0$, that is, the interaction of the PC with the medium in the left half space.

For a given PC, the Bloch wavevector can be solved from the eigenvalue problem described by Eq. (2.22) for any real positive values of ω and k_x. In general, K is complex.

When K is purely real, i.e., $\mathrm{Im}(K) = 0$, the electric field oscillates in the z direction, and the Bloch wave propagates into the positive z direction, which is called an *extended mode*. When $\mathrm{Im}(K) \neq 0$, on the other hand, the amplitude of the Bloch wave decays exponentially into the positive z direction, and the wave is confined to the first few unit cells of the photonic crystal; this is called a *localized mode* [33,36]. Localized mode can also occur inside a PC in the stop band if defects are introduced. In analog to real crystals, a defect is a local change of material properties or geometric parameters within the PC. Further studies about the field localization effects in the disordered periodic multilayers due to the random thickness variation can be found in [71,72]. Notice that $K = K(k_x, \omega)$, and the regions with $\mathrm{Im}(K) = 0$ in the $\omega - k_x$ plane are called pass bands, and those with $\mathrm{Im}(K) \neq 0$ are called stop bands. Suppose light is incident from air (in the left half space) on the PC at $z = 0$; in the stop band, the PC will act like a perfect mirror, which is also called a Bragg reflector, especially when the thickness of each dielectric is a quarter of the wavelength in that medium. A diagram in the $\omega - k_x$ domain showing the different regions allows one to study the band structure of a PC.

Figure 2.4 shows the calculated band structure of the 1D PC for both polarizations. Here, it is assumed that $d_{\mathrm{H}} = d_{\mathrm{L}}$, so that Λ is the only geometric parameter that affects the band structure. For convenience, the refractive indices for the two types of dielectrics are assumed to be constant, $n_{\mathrm{H}} = 2.4$ and $n_{\mathrm{L}} = 1.5$, in the wavelength region of interest. These values approximate those of ZnSe ($n \approx 2.4$) and KBr ($n \approx 1.52$) near $\lambda = 11\ \mu\mathrm{m}$ [73]. The band structure is expressed by the reduced frequency and wavevector, so that Fig. 2.4 is applicable to arbitrary values of Λ. The shaded regions

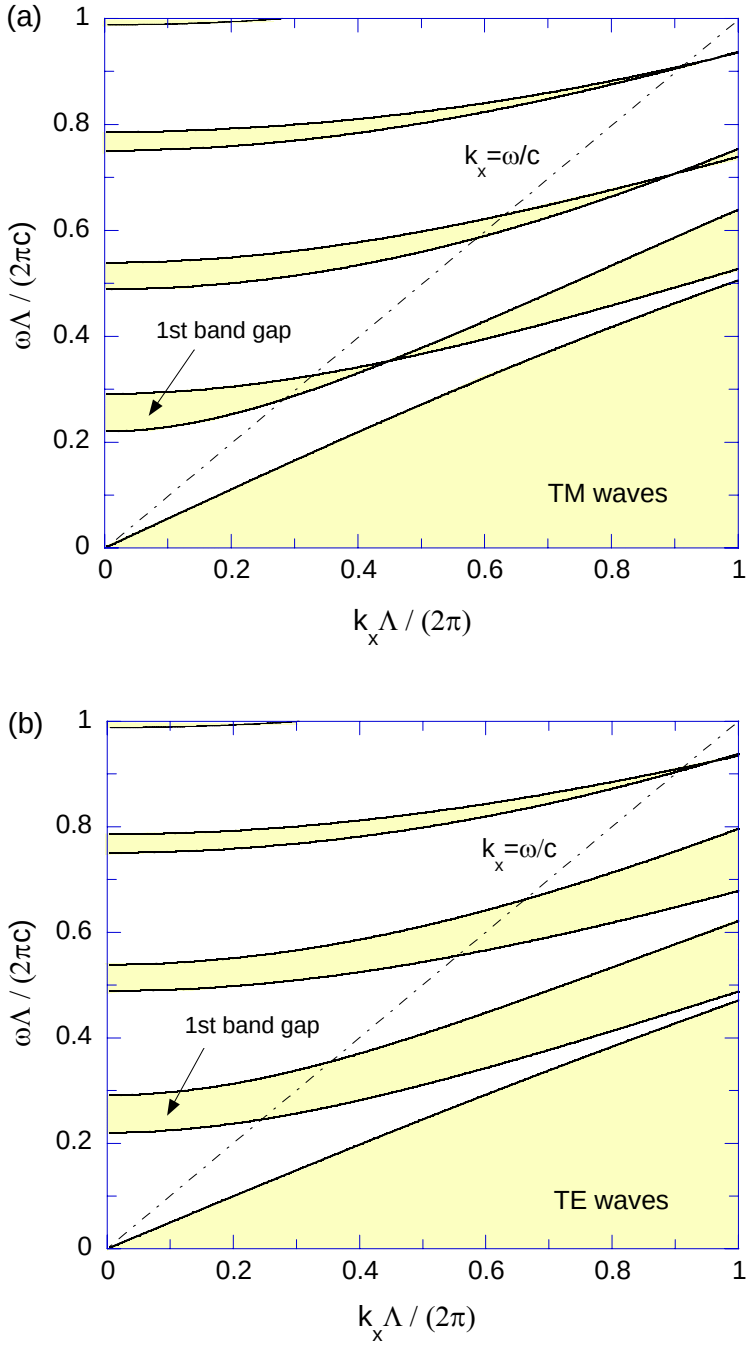

Figure 2.4 Band structure of the 1D PC shown in Fig. 2.3, with $d_H = d_L$, $n_H = 2.4$ and $n_L = 1.5$ in the reduced ω–k_x domain: (a) TM waves; and (b) TE waves. The dash-dot line denotes the light line in air. The crossovers for TM waves are due to the Brewster angle between constituent dielectrics.

represent stop bands, and the unshaded regions are for pass bands. The light line in air is plotted as a dash-dot line. On the upper-left side of this line, propagating waves exist in air. Here, the parallel component of wavevector is given by $k_x = (\omega / c)\sin\theta$, where θ is the angle of incidence. On the lower-right side of this line, evanescent waves exist in air. Alternatively, one can think that the light line corresponds to an incidence angle (or emission angle) of 90°. Note that width of the first two stop bands shrinks to zero only for TM waves. The crossover point corresponds to the Brewster angle between constituent dielectrics. At the Brewster angle, the reflectivity at the interface between the two dielectrics is zero; thus, waves can always propagate into the PC.

Surface Electromagnetic Waves in Photonic Crystals

Surface polaritons (or surface waves) are electromagnetic waves that propagate along the interface between different media and exponentially decay in both media away from the interface [25]. The excitation of surface waves is a resonance phenomenon, i.e., a coupling between electromagnetic waves and collective motions of electrons or phonons in a certain medium (e.g., a metal or a polar material). The excitation of surface waves often requires the parallel component of the incident wavevector to exceed the magnitude of the wavevector in vacuum; thus, an attenuated total reflection (ATR) configuration is commonly used to couple the incident wave and the surface wave [25,74]. In addition to prism couplers, surface relief gratings can also excite surface waves due to diffraction. Surface-wave excitation can modify the thermal-emission characteristics to achieve temporal and/or spatial coherence from binary gratings constructed with a polar material [24] or a metal [22].

Localized surface modes at the edge of a photonic crystal (PC) have been extensively studied for both 1D [37-39] and 2D structures [42,75-78]. The optical surface modes for semi-infinite PCs are analogous to the localized electronic states, at the surface of a crystalline solid, predicted by Tamm [79] in the 1930s. In essence, surface waves at the edge of the PC and another medium are due to the Bloch wave, whose amplitude exponentially decays away from the interface inside the PC in the stop band. To illustrate the Bloch wave inside the PC, let us consider a semi-infinite 1D PC in the $z > 0$ half-plane adjunct with air in the $z < 0$ half-plane. When TM-polarized plane wave is normally incident from air to the PC, the magnetic field distributions are illustrated in Fig. 2.5 for two different frequencies: one located in the pass band and the other in the stop band. The behavior of the Bloch wave in the PC depends on the Bloch wavevector K (refer to Fig. 2.7). When K is purely real, the Bloch wave will propagate through the PC, as shown in Fig. 2.5(a). In this case, the wavelike term $\exp(iKz)$ determines the oscillation of the magnetic field, and the periodic function $u(z)$ determines the envelope of the field amplitude. On the other hand, if the imaginary part of K is not zero, the amplitude of oscillation decays exponentially from the surface at $z = 0$, as shown in Fig. 2.5(b). In fact, the Bloch wave with complex K is an oscillating field, whose amplitude gradually decays to zero as z approaches infinity. In a stop band, no energy can be transmitted through the PC, and the field distribution is similar to that of an evanescent wave in a semi-infinite medium. Therefore, the Bloch wave inside the PC at the stop band is called an effective evanescent wave [80]. The advantageous feature of the PC is that stop bands exist for either polarization [33,81], so that surface wave can be supported by the PC for both polarizations.

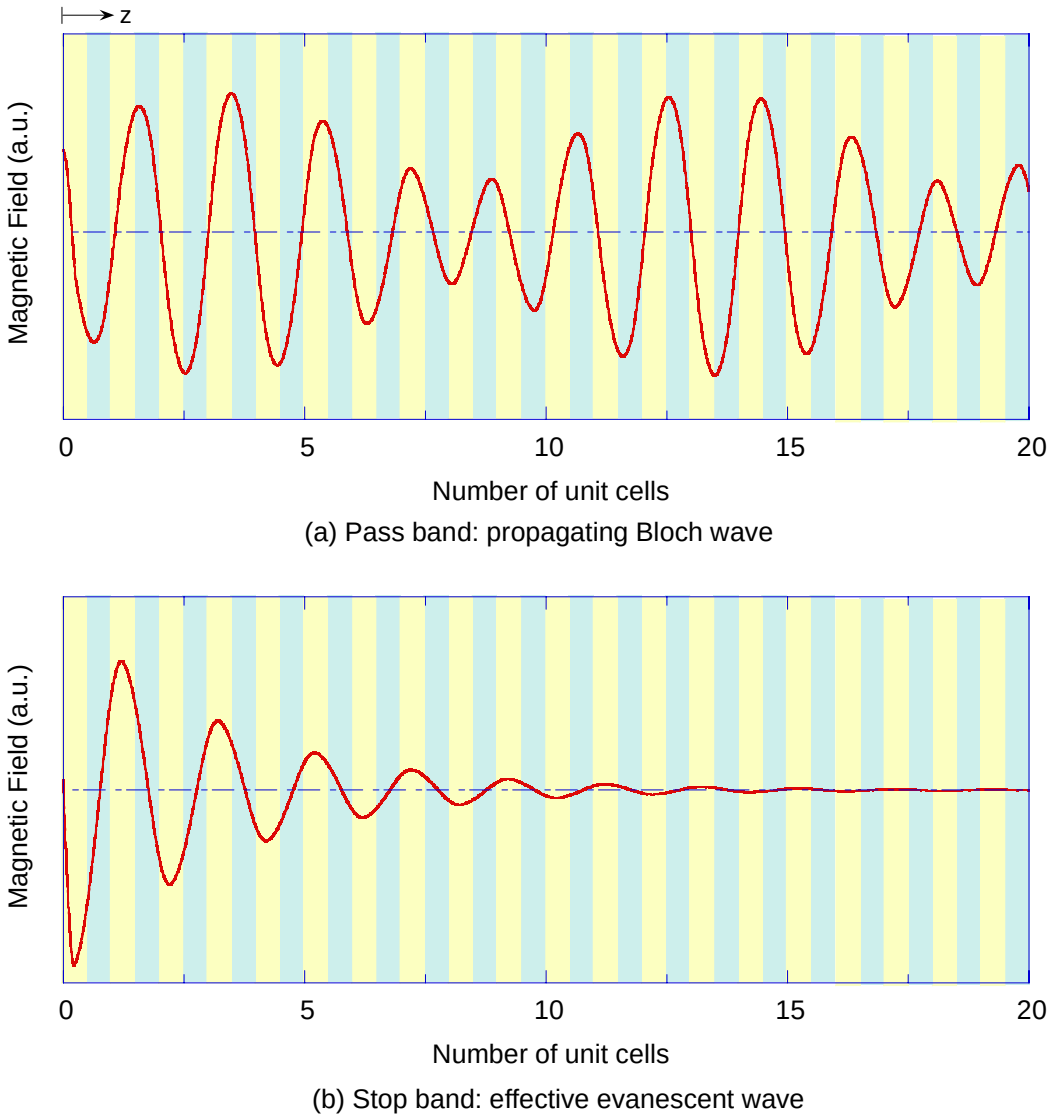

Figure 2.5 Magnetic field distribution inside a 1D PC when a plane wave is incident from air on the semi-infinite PC: (a) Bloch wave with a real K in a pass band; (b) Bloch wave with a complex K in a stop band.

In general, it is inappropriate to treat a PC structure as a homogeneous medium with equivalent ε and μ that are independent of the space. For this reason, the simple dispersion relation for surface waves at the interface between homogenous media [25] is not applicable to PCs. Nevertheless, the surface-wave dispersion relation for 1D PCs can be obtained using the supercell method [82]. The supercell method was originally developed and applied, in combination with the plane-wave expansion technique [83], to demonstrate surface waves at the edge of a truncated 2D or 3D PC [84,85]. However, the existing supercell formulation did not properly consider the mathematical rules for the Fourier expansion of the product of functions [86]. In the following, the equations are modified to improve the convergence rate of solutions, especially for TM waves when a metallic layer is involved.

For TM waves, the *y*-component of magnetic field can be expressed in the Bloch wave form similar to Eq. (2.23). Since $u(z)$ is a periodic function of *z*, the magnetic field can be expressed as a Fourier series

$$H_y(x,z) = \sum_j u_j \exp\left[i(G_j + K)z\right]\exp\left(ik_x x\right) \tag{2.27}$$

where u_j is the *j*th Fourier coefficient of $u(z)$ and G_j is a reciprocal lattice vector given by $G_j = 2\pi j/\Lambda$. The index *j* can be $j = 0, \pm 1, \pm 2,$ etc. Due to the periodicity of the PC, the dielectric function of alternating layers can also be expressed in a Fourier expansion

$$\varepsilon^{\text{ord}}(z) = \varepsilon(z) = \sum_l \varepsilon_l^{\text{ord}} \exp(iG_l z) \tag{2.28}$$

It is essential to express the inverse of the dielectric function as a separate Fourier expansion, i.e.,

$$\varepsilon^{\text{inv}}(z) = \frac{1}{\varepsilon(z)} = \sum_l \varepsilon_l^{\text{inv}} \exp(iG_l z) \tag{2.29}$$

where $\varepsilon_l^{\text{ord}}$ and $\varepsilon_l^{\text{inv}}$ are the lth Fourier coefficient for the ordinary and inverse of $\varepsilon(z)$, respectively; and it is important to notice that, in general, $\varepsilon_l^{\text{inv}} \neq 1/\varepsilon_l^{\text{ord}}$. Although j and l can be any integer, in the numerical calculation, a positive integer N is chosen so that $j = 0, \pm 1, \pm 2, ... \pm N$ and $l = 0, \pm 1, \pm 2, ... \pm 2N$. The reason will become obvious soon. Increasing N results in higher accuracy at the cost of computational time and memory. The proper usage of Eqs. (2.28) and (2.29) is critical to ensure the convergence of the series solution given in Eq. (2.27) with N Fourier terms, as explained in the following. The wave equation for the magnetic field can be obtained from Maxwell's equations:

$$\frac{\partial}{\partial z}\left(\frac{1}{\varepsilon(z)}\frac{\partial H_y}{\partial z}\right) + \frac{1}{\varepsilon(z)}\frac{\partial^2 H_y}{\partial x^2} = -\left(\frac{\omega}{c}\right)^2 H_y \tag{2.30}$$

Substituting Eqs. (2.27), (2.28), and (2.29) into Eq. (2.30), one obtains the coupled equation for u_j's . The key is to arrange Eq. (2.30) into a summation of $\exp\left[i(G_j + K)z\right]\exp\left(ik_x x\right)$ and then set its coefficient to zero for each j. In addition to H_y, both $\varepsilon^{\text{ord}}(x)$ and $\varepsilon^{\text{inv}}(x)$ are also Fourier expansion of $\exp(iG_l z)$; thus, the mathematical rules summarized in the work of Li [86] must be carefully applied when factoring the term of $\exp\left[i(G_j + K)z\right]\exp\left(ik_x x\right)$ from a product of functions. In essence, the first term in the left side of Eq. (2.30) should be expressed by the *inverse rule*; however, the second term must follow *Laurent's rule* [86]. As a result, the modified coupled equation is given by

$$\sum_m (G_j + K)(G_m + K)\,\bar{A}_{j,m}\,u_m + \sum_m k_x^2\,B_{j,m}\,u_m = (\omega/c)^2 u_j \tag{2.31}$$

where $m = 0, \pm 1, \pm 2, \ldots \pm N$, **A** and **B** are Toeplitz matrices generated by the Fourier coefficients of the dielectric function and its inverse, respectively, such that $A_{j,m} = \varepsilon_l^{\text{ord}}$ and $B_{j,m} = \varepsilon_l^{\text{inv}}$ with $l = j - m$, and $\bar{A}_{j,m}$ denotes the matrix element for $\mathbf{A}^{-1}$, i.e., the inverse matrix of **A**. The authors of Ref. [82] did not consider the inverse rule in the derivation. This does not cause any problem for the TE wave since only the Laurent rule is involved. For the TM wave, however, it is crucial to distinguish $\varepsilon_l^{\text{ord}}$ and $\varepsilon_l^{\text{inv}}$ and to apply them according to the discussion just given.

Equation (2.31) can be expressed in the matrix form as an eigenvalue equation:

$$\mathbf{MU} = \xi \mathbf{U} \tag{2.32}$$

where **M** is the matrix given by $\mathbf{M} = \mathbf{K^G A^{-1} K^G} + k_x^2 \mathbf{B}$, **U** is the column vector composed of u_j (i.e., eigenvector), and ξ is the eigenvalue. Here, $\mathbf{K^G}$ is a diagonal matrix whose element is defined by $K_{i,j}^G = (G_j + K)$ if $i = j$ and 0 otherwise. For given values of *K* and k_x, the matrix **M** is uniquely determined, and thus, a set of eigenvalues and eigenvectors can be obtained by solving Eq. (2.32). The eigenvalue ξ is related to the angular frequency by $\xi = (\omega/c)^2$ and eigenvector **U** determines the Bloch wave solution given by Eq. (2.27). If *K* is set to be a real quantity, the obtained frequencies must locate inside the pass bands. Therefore, by fixing k_x value and varying *K* in the range of $0 < K < 0.5G_1$, one can determine the frequency ranges where Bloch waves are associated with real *K* values (i.e., pass band). If such calculation is repeated for different

k_x values, the pass bands can be completely identified in the $\omega - k_x$ plane. A simpler way of constructing the band structure is to identify the pass band edges only. It is found that the pass band edges correspond to solutions for $K = 0$ or $K = G_1$.

It should be noted that Eqs. (2.28) and (2.29) implicitly require that the periodic structure infinitely extend in both the positive and negative *z* directions (i.e., infinite lattice structure). In reality, however, only a truncated PC can exist. Let us consider a truncated PC coated on a Ag layer shown in Fig. 2.6(a) as an example. To properly consider the surface termination of the PC and its coupling with a Ag layer, it is necessary to construct a supercell, which is a fictitious and infinitely periodic superstructure. One period of the supercell is composed of a finite number of unit cells of the original PC bounded by Ag films on both sides, as depicted in Fig. 2.6(b). The number of complete unit cells in the supercell is not necessarily the same as that in the initial PC-on-Ag structure. In fact, there should be a sufficient number of complete unit cells in the supercell structure to prevent the coupling of surface waves at both PC-Ag interfaces. For the same reason, the thickness of the Ag layers must be much greater than its radiation penetration depth. In the supercell, the translational invariance is manifested by complete unit cells and the surface termination is properly incorporated by terminated unit cells adjacent to the Ag layer. Due to the periodicity of the supercell structure, the dielectric function and its inverse can also be expressed in a Fourier series similar to Eqs. (2.28) and (2.29). Accordingly, the solution of Maxwell's equations for the supercell must satisfy the Bloch condition. One can thus derive a matrix eigenvalue equation for the supercell structure, with the form similar to Eq. (2.32).

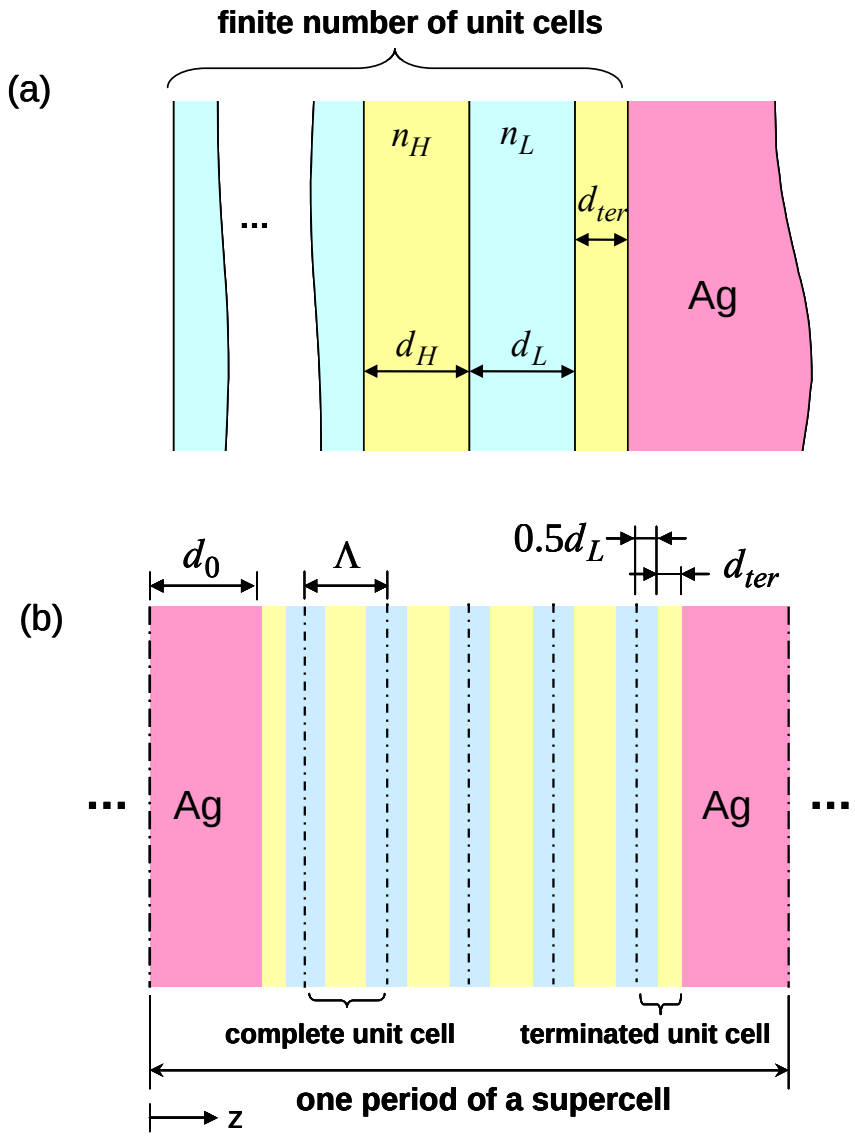

Figure 2.6 Illustration of supercell structure: (a) A 1D PC with few unit cells coated on an optically thick Ag film. The thickness of d_{ter} determines the surface termination of the PC adjacent to the Ag layer. (b) One period of the supercell is composed of a truncated PC bounded by Ag film in a symmetric manner.

The key idea of the supercell method is to convert the surface modes of the truncated PC to the eigenmodes of the supercell structure (i.e., Bloch waves in pass bands). By solving the eigenvalue equation for the supercell, the band structure can be constructed in the $\omega - k_x$ plane. If supercell's band structure is transferred to original PC's band structure, all pass bands of the original PC are matched by those of the supercell. In the supercell, however, there exist additional pass bands, which correspond to surface modes at the PC-Ag interface. Notice that the pass bands corresponding to surface modes must have an infinitely narrow width because the coupling of surface waves at both PC-Ag interfaces is prohibited. In other words, the solution is infinitely degenerated, so that it essentially forms a line. If the solutions of surface modes are transferred to the original PC's band structure, they must locate in the stop bands and represent the dispersion curves of surface waves at the PC-Ag interface.

Poynting Vector and Energy Streamline

The enhanced radiative energy transfer between closely spaced surfaces is greatly related to photon tunneling through a subwavelength layer, whose refractive index is smaller than the media that sandwich it [87]. The ray optics fails to describe the photon tunneling phenomenon because the parallel wavevector component for an evanescent wave is so large that no polar angle within the real space can be defined. On the other hand, an energy streamline (ESL) can be unambiguously defined based on the Poynting vector of coupled plane waves, such that the direction of energy flow can be characterized by the streamline that connects the local Poynting vectors [88].

Consider the geometry of three layers shown in Fig. 2.7, where media 1 and 3 are semi-infinite. Each layer is linear, homogeneous and isotropic. The electric and magnetic

responses can be characterized by the relative permittivity ε and permeability μ, which in general are complex and frequency dependent. If the incidence is a TM wave, the magnetic field in each region is given by Eq. (2.33), where subscripts are omitted for simplicity.

$$H_y(x,z) = \left[Ae^{ik_z z} + Be^{-k_z z} \right] e^{ik_x x} \tag{2.33}$$

Here, A and B are the coefficients of forward and backward waves at the interface, z is relative to the origin in media 1 and 2, while in medium 3, z is relative to d, and $k_x^2 + k_z^2 = \varepsilon\mu\omega^2 / c^2$. Boundary conditions require that k_x be real and independent of z. The components of the time-averaged Poynting vector, $\langle \mathbf{S} \rangle = \frac{1}{2}\mathrm{Re}\left(\mathbf{E} \times \mathbf{H}^* \right)$, can be obtained by applying Maxwell's equations for the electric field; hence,

$$\begin{aligned} \langle S_z \rangle = & \frac{1}{2\omega\varepsilon_0}\mathrm{Re}\left(\frac{k_z}{\varepsilon} \right)\left[|A|^2 e^{-2\,\mathrm{Im}(k_z)z} - |B|^2 e^{2\,\mathrm{Im}(k_z)z} \right] \\ & - \frac{1}{\omega\varepsilon_0}\mathrm{Im}\left(\frac{k_z}{\varepsilon} \right)\mathrm{Im}\left(AB^* e^{2i\,\mathrm{Re}(k_z)z} \right) \end{aligned} \tag{2.34}$$

$$\begin{aligned} \langle S_x \rangle = & \frac{k_x}{2\omega\varepsilon_0}\mathrm{Re}\left(\frac{1}{\varepsilon} \right)\left[|A|^2 e^{-2\,\mathrm{Im}(k_z)z} + |B|^2 e^{2\,\mathrm{Im}(k_z)z} \right] \\ & + \frac{k_x}{\omega\varepsilon_0}\mathrm{Re}\left(\frac{1}{\varepsilon} \right)\mathrm{Re}\left(AB^* e^{2i\,\mathrm{Re}(k_z)z} \right) \end{aligned} \tag{2.35}$$

The last terms in Eqs. (2.34) and (2.35) arise from the coupling between the forward and backward waves, and are in general nonzero. The direction of $\langle \mathbf{S} \rangle$ of the combined wave can always be defined by a polar angle $\theta_{\mathrm{E}} = \arctan\left(\langle S_x \rangle / \langle S_z \rangle \right)$; in contrast, it is not always possible to define the angle of incidence or refraction, $\theta = \arctan(k_x / k_z)$ in the real space. The trajectory of $\langle \mathbf{S} \rangle$ for given ω and k_x is an ESL, which defines the path of

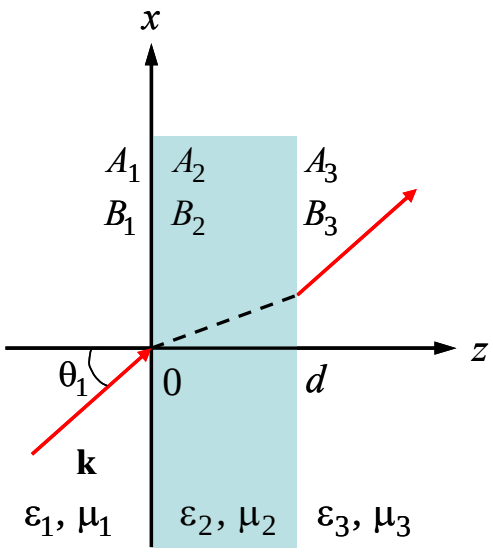

Figure 2.7 Schematic of the three layer structure, where media 1 and 3 are semi-infinite, and medium 2 has a thickness of d. the incidence angle θ_1 is determined by the wavevector. Each medium is linear, homogeneous, and isotropic.

the net energy flow. Note that the dependence of μ is implicit in Eqs. (2.34) and (2.35), since k_z is a function of μ, and furthermore, A's and B's depend on k_z's. By setting $A_1 = 1$ and $B_3 = 0$, the coefficients A and B in each layer can be obtained from boundary conditions that tangential components of the magnetic and electric fields are continuous at the interface. Assuming the symmetric configuration (i.e., $\varepsilon_1 = \varepsilon_3$), the coefficients are given

$$B_1 = \xi_1 \xi_2 (e^{-ik_{2z}d} - e^{ik_{2z}d}) / \zeta \tag{2.36}$$

$$A_2 = 2k_{1z}\xi_1 e^{-ik_{2z}d} / (\varepsilon_1 \zeta) \tag{2.37}$$

$$B_2 = -2k_{1z}\xi_2 e^{ik_{2z}d} / (\varepsilon_1 \zeta) \tag{2.38}$$

$$A_3 = 4k_{1z}k_{2z} / (\varepsilon_1 \varepsilon_2 \zeta) \tag{2.39}$$

where $\xi_1 = \left(k_{1z}/\varepsilon_1 + k_{2z}/\varepsilon_2\right)$, $\xi_2 = \left(k_{1z}/\varepsilon_1 - k_{2z}/\varepsilon_2\right)$, and $\zeta = (\xi_1^2 e^{-ik_{2z}d} - \xi_2^2 e^{ik_{2z}d})$. For TE waves, the magnetic field is replaced by the electric field in Eq. (2.33), and ε_j's are replaced by μ_j's in Eqs. (2.34), (2.35), (2.36), (2.37), (2.38), and (2.39).

At the critical angle, the magnetic field in medium 2 propagates along the interface and does not decay in the z direction because $k_z = 0$. In such case, tangential component of the electric field vector must be zero in medium 2 because electromagnetic wave is transverse to the wave propagation direction. It is obvious that there is no analytical solution of the electromagnetic fields that satisfy boundary conditions for both electric and magnetic fields if there is a transmitted wave in medium 3. The exact solution yields total reflection without tunneling. When the incidence angle is slightly perturbed from the critical angle, the solutions in the proximity limit approach the same result from either side as the incidence angle approaches the critical angle. Hence, the singularity at the critical angle can be removed numerically, so that transmittance is obtained as a continuous function of the incidence angle.

CHAPTER 3

THEORETICAL ANALYSIS OF COHERENT EMISSION FOR MULTILAYER STRUCTURE

This chapter describes a comprehensive investigation of the multilayer structure for coherent emission. The structure is made of a polar material and a semi-infinite 1D PC, as shown in Fig. 3.1. Here, the PC is terminated or modified by placing a polar material on top of it to couple surface waves with propagating waves in air. Hereafter, it will be called as the SiC-on-PC structure. The unit cell of a 1D PC is composed of the alternating dielectrics with different refractive indices n_{H} and n_{L}, respectively, and defined by the following thicknesses: d_{ter}, d_{L}, and $d_{\mathrm{H}} - d_{\mathrm{ter}}$ with a period (or lattice constant) $\Lambda = d_{\mathrm{H}} + d_{\mathrm{L}}$. In practice, only a finite number of unit cells are required and thin films can be deposited onto a suitable substrate, such as silicon. The thickness d_{ter}, which may be varied from 0 to d_{H}, plays an important role in tuning the coherent emission wavelength. The spectral-directional emissivity of the SiC-on-PC structure is calculated using the transfer matrix formulation [69,70,89], as described in Chapter 2. By examining conditions that cause a large emission in a narrow spectral range and an angular lobe in a well-defined direction, a regime map is developed to identify the emissivity enhancement due to three different mechanisms: the excitation of surface waves, cavity resonance mode, and the Brewster mode. The effects of geometric parameters and arrangement of the high- and low-index dielectrics in the PC on the emission characteristics are also investigated.

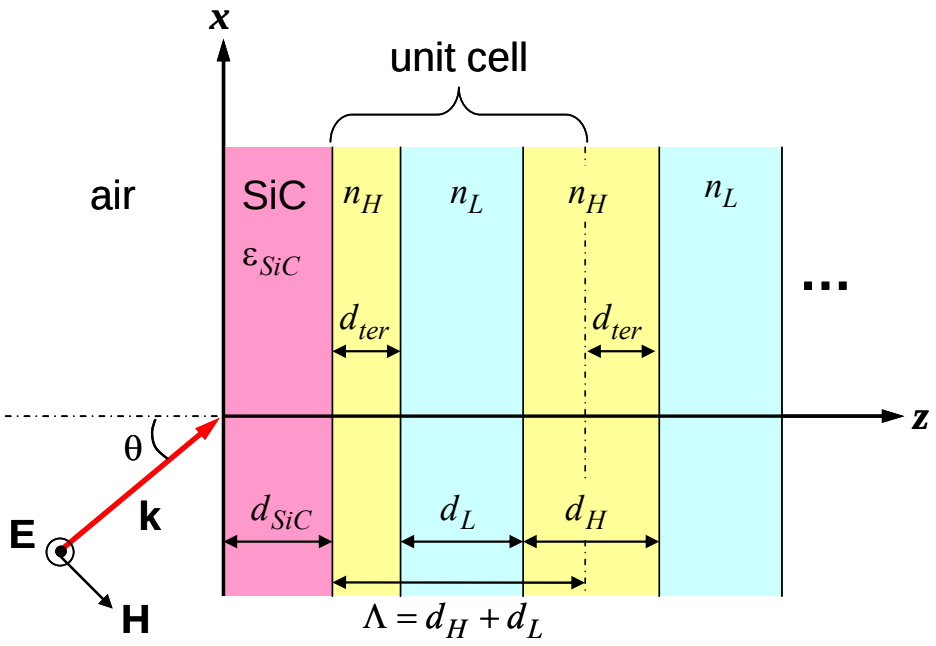

Figure 3.1 Schematic of the multilayer structure made of a SiC layer coated on a semi-infinite 1D PC for a TE wave incident from air. The unit cell of the PC consists of a high-refractive-index dielectric on both sides of a low-refractive-index dielectric with a total thickness (lattice constant) $\Lambda = d_H + d_L$. The surface termination is determined by the thickness of the dielectric (d_{ter}) next to the SiC film with a dielectric function of ε_{SiC}.

SiC is a polar material with strong lattice absorption for wavelengths (λ) between 10 μm and 13 μm. In reality, the dielectric function of SiC is a complex quantity due to loss or damping. In the infrared region, the optical constants of SiC are calculated from the functional expression of ε_{SiC} given by [90]:

$$\varepsilon_{SiC} = \left(n_{SiC} + i\kappa_{SiC}\right)^2 = \varepsilon_\infty \left(1 + \frac{\nu_{LO}^2 - \nu_{TO}^2}{\nu_{TO}^2 - \nu^2 - i\Gamma\nu}\right) \tag{3.1}$$

where $\nu = 1/\lambda$ is the wavenumber in cm^{-1}, $\varepsilon_\infty = 6.7$ is a high-frequency constant, $\nu_{LO} = 969\,\text{cm}^{-1}$ is the longitudinal optical (LO) phonon frequency, $\nu_{TO} = 793\,\text{cm}^{-1}$ is the transverse optical (TO) phonon frequency, and $\Gamma = 4.76\,\text{cm}^{-1}$ is the damping coefficient

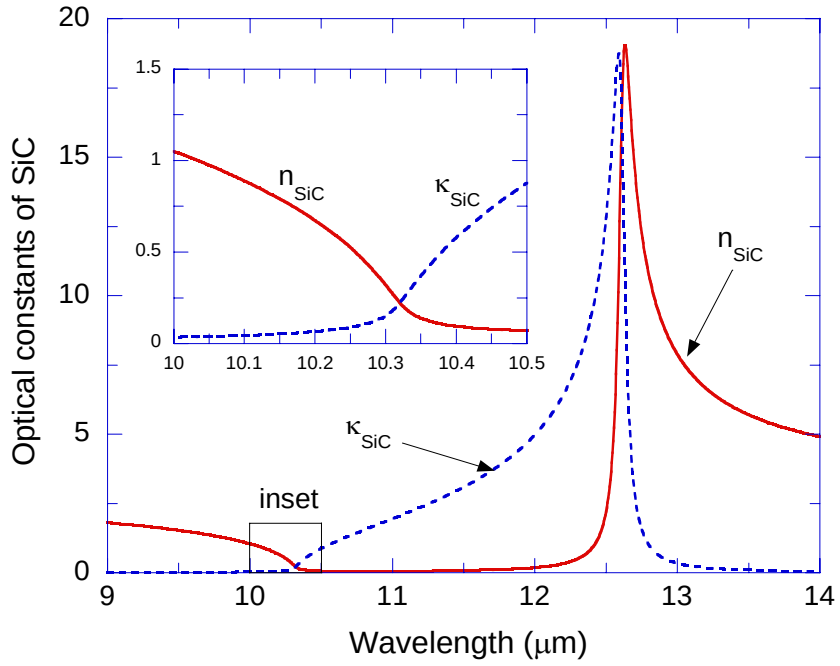

Figure 3.2 The optical constants of SiC predicted by the phonon oscillator model in Eq. (3.1) at wavelengths from 9 μm to 14 μm. The inset is for wavelengths from 10 μm to 10.5 μm.

(or scattering rate). From Eq. (3.1), it can be easily seen that the real part of $\varepsilon_{\mathrm{SiC}}$ is negative for $\nu_{\mathrm{TO}} < \nu < \nu_{\mathrm{LO}}$. In Fig. 3.2, the optical constants of SiC are plotted against the wavelength in the vicinity of the phonon absorption band, and the inset of Fig. 3.2 will be used in the later discussion. It is clear that κ_{SiC} is much larger than n_{SiC} within the phonon absorption band.

Figure 3.3(a) shows the directional-hemispherical reflectance R of the 1D PC coated with a SiC film (solid line) at normal incidence. Geometric parameters for the 1D PC are $d_{\mathrm{H}} = d_{\mathrm{L}} = 3\ \mu\mathrm{m}$, and the surface termination occurs in the high-index dielectric at $d_{\mathrm{ter}} = d_{\mathrm{H}} / 2$. The effect of thickness d_{ter} will be discussed later. For convenience, the refractive indices for the two types of dielectrics are assumed to be constant, $n_{\mathrm{H}} = 2.4$

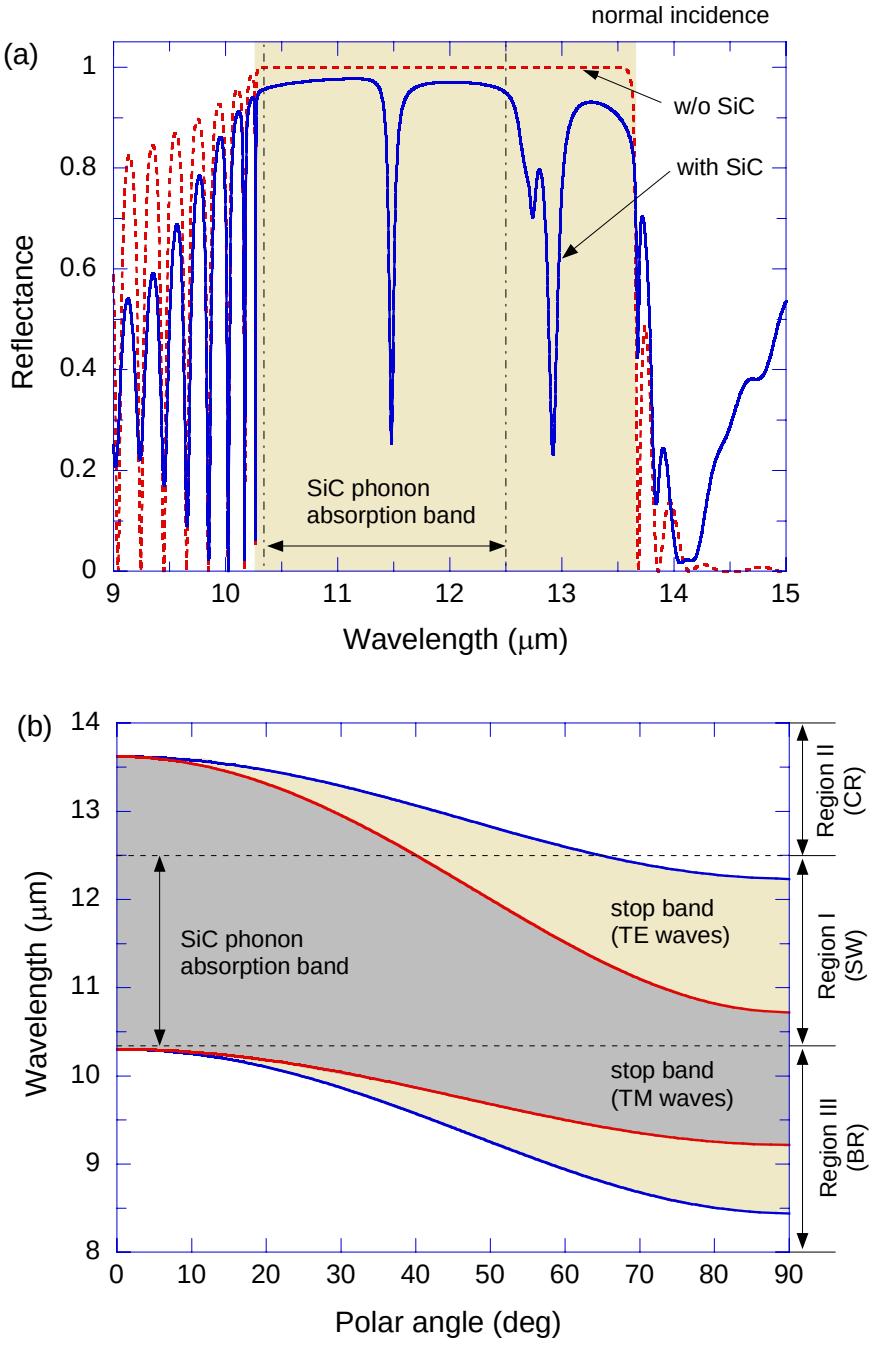

Figure 3.3 Identification of the important regimes where the radiative properties are dominated by different mechanisms. (a) The reflectance of the 1D PC with a 1.45-μm-thick SiC layer, where the dotted line is for the 1D PC without SiC. (b) The regime map in λ–θ space. CR stands for the cavity resonance mode, SW for surface wave, and BR for the Brewster mode. The shaded areas are corresponding to the first band gap of the 1D PC for TE waves (lighter) and TM waves (darker). The phonon absorption band of SiC is between the two dashed horizontal lines.

and $n_L = 1.5$, in the wavelength region of interest. Calculations show that 30 periods of unit cells are sufficient to be approximated as semi-infinite in the stop band. The thickness of SiC is set to be 1.45 μm. The reflectance of 30-period PC without SiC is plotted as dashed line for comparison. The reflectance of the PC without SiC is unity in the shaded region that corresponds to the first stop band of the 1D PC with $\Lambda = 3$ μm. Several dips appear in the reflectance spectrum with SiC within the stop band. The first dip around $\lambda = 11.5$ μm is located in the phonon absorption band of SiC and is caused by the excitation of surface waves. Two reflectance dips also appear in the stop band near $\lambda = 13$ μm, where propagating waves exist in the SiC film. These reflectance dips are caused by cavity resonance, when a standing wave exists inside the SiC layer. Note that interference effects cause some oscillations at wavelengths shorter than 10.2 μm and longer than 13.6 μm. The period of oscillation varies with the number of unit cells and the reduction in the reflectance corresponds to a large transmittance through the photonic crystal if it is not infinitely extended. Since the present study is focused on the coherent emission from the SiC layer, only features within the stop band will be further discussed.

The reflectance also depends on the angle of incidence. A regime map in the $\lambda - \theta$ plane can be constructed and is shown in Fig. 3.3(b) to identify regions where surface wave or cavity resonance mode can be excited. Region I represents the domain where the PC's stop band overlaps the SiC phonon absorption band. In this region, surface waves can be excited at the interface between SiC and 1D PC. Cavity resonance can occur in Region II, which is outside the SiC absorption band, for the SiC-on-PC structure. In Region III, another phenomenon, the Brewster mode may introduce coherent emission but only for TM waves at sufficiently large incidence angles.

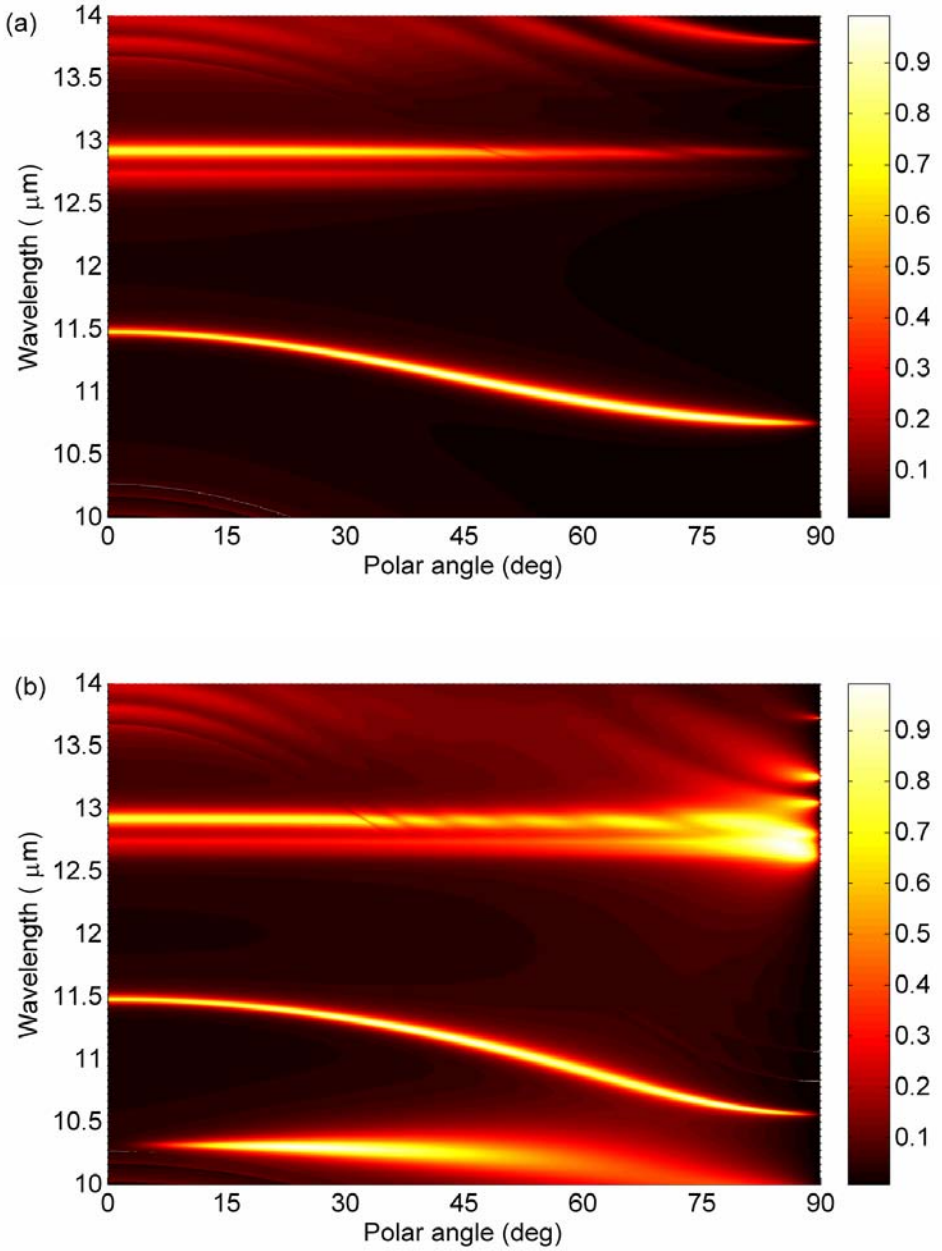

Figure 3.4 Contour plot of the spectral-directional emissivity of the SiC-on-PC structure: (a) TE waves; (b) TM waves. The thickness of SiC is set to be 1.45 μm.

The spectral-directional emissivity is illustrated by the contour plot in Fig. 3.4 for both polarizations as a function of the wavelength and emission angle. From Kirchhoff's law [1], the spectral-directional emissivity $\varepsilon_{\lambda,\theta}$ can be obtained by $\varepsilon_{\lambda,\theta} = 1 - R - T$, where T is the directional-hemispherical transmittance. The large emissivity values can be seen in a certain range of wavelengths and emission angles. As discussed previously, there exist three different mechanisms for the SiC-on-PC structure. The surface-wave excitation and cavity resonance [15,16,29] can happen for both polarizations even at normal incidence or emission, while the Brewster mode [91] can occur only for TM waves and at oblique incidence. For the bands that are relatively flat (e.g., upper branches near 13 μm for both figures), the emissivity is almost independent of the polar angle. Therefore, relatively diffuse emission can be achieved from flat bands. In Figs. 3.4(a) and 3.4(b), the top band around 13 μm is due to cavity resonance. For the lower band in Fig. 3.4(a) and middle band in Fig. 3.4(b), on the other hand, coherent emission is due to the excitation of surface waves and is confined in a narrow angular range at a given resonance wavelength. Finally, the bottom band in Fig. 3.4(b) is due to the Brewster mode. For the SiC-on-PC structure, the Brewster mode also results in relatively flat band like the cavity resonance mode. In the following, each mode contributing to coherent thermal emission from the SiC-on-PC structure is separately considered.

Excitation of Surface Waves

Figure 3.5(a) shows the spectral-directional emissivity spectra in the wavelengths between 10.5 μm and 12.5 μm at $\theta = 0°$, 30°, and 60° for both polarizations. In the calculation, the same parameters as in Fig. 3.3 are used for the 1D PC. The solid lines are for TE waves, and the dashed ones are for TM waves. Notice that since the emission peak

values depend on the thickness of SiC, d_{SiC} can be tuned to maximize the emissivity for any given emission angle and polarization states. Here, the thickness of SiC is set to be $d_{\mathrm{SiC}} = 1.45\,\mu\mathrm{m}$, which results in a near-unity emissivity at $\theta = 60°$ for TE waves and slightly lower emission peaks at other conditions. For TE waves, as an example, very large $\varepsilon_{\lambda,\theta}$ can be seen in a narrow wavelength band centered at $\lambda_{\mathrm{c}} = 11.479$, 11.293, and 10.929 μm for emission angles of $0°$, $30°$, and $60°$, respectively. The emissivity is very small outside the narrow band. The spectral emission peaks clearly show temporal coherence, which is an indication of the monochromatic behavior of the source. The sharpness of the emissivity peak at the surface-wave resonance condition can be delineated by quality factor $Q = \lambda_{\mathrm{c}} / \Delta\lambda$ [29], where $\Delta\lambda$ is the full-width-at-half-maximum (FWHM) at the narrow wavelength band. The calculated Q values are 230, 185, and 133, respectively, which are comparable to those for gratings [24] and single negative materials [17]. Compared with those for TE waves, the emissivity peaks for TM waves are the same for $\theta = 0°$ and slightly shift in wavelength for $\theta = 30°$ and $60°$.

The spatial coherence of the emission source can be seen by the angular distributions of the emissivity, shown in Fig. 3.5(b) at the three peak wavelengths for TE waves. The narrower the emissivity lobe, the more spatially coherent the thermal source. It is important to note that the emissivity is intentionally plotted as a polar plot to clearly show the narrow angular lobe in the well-defined direction. However, if one considers the actual emission source with finite dimensions, due to the axial symmetry of the planar structure, coherent emission from the SiC-on-PC structure exhibits circular patterns [80], in contrast to the antenna shape for grating surfaces [24]. The patterns are very similar for TM waves at the corresponding peak wavelengths. The emissivity at each λ_{c} is confined

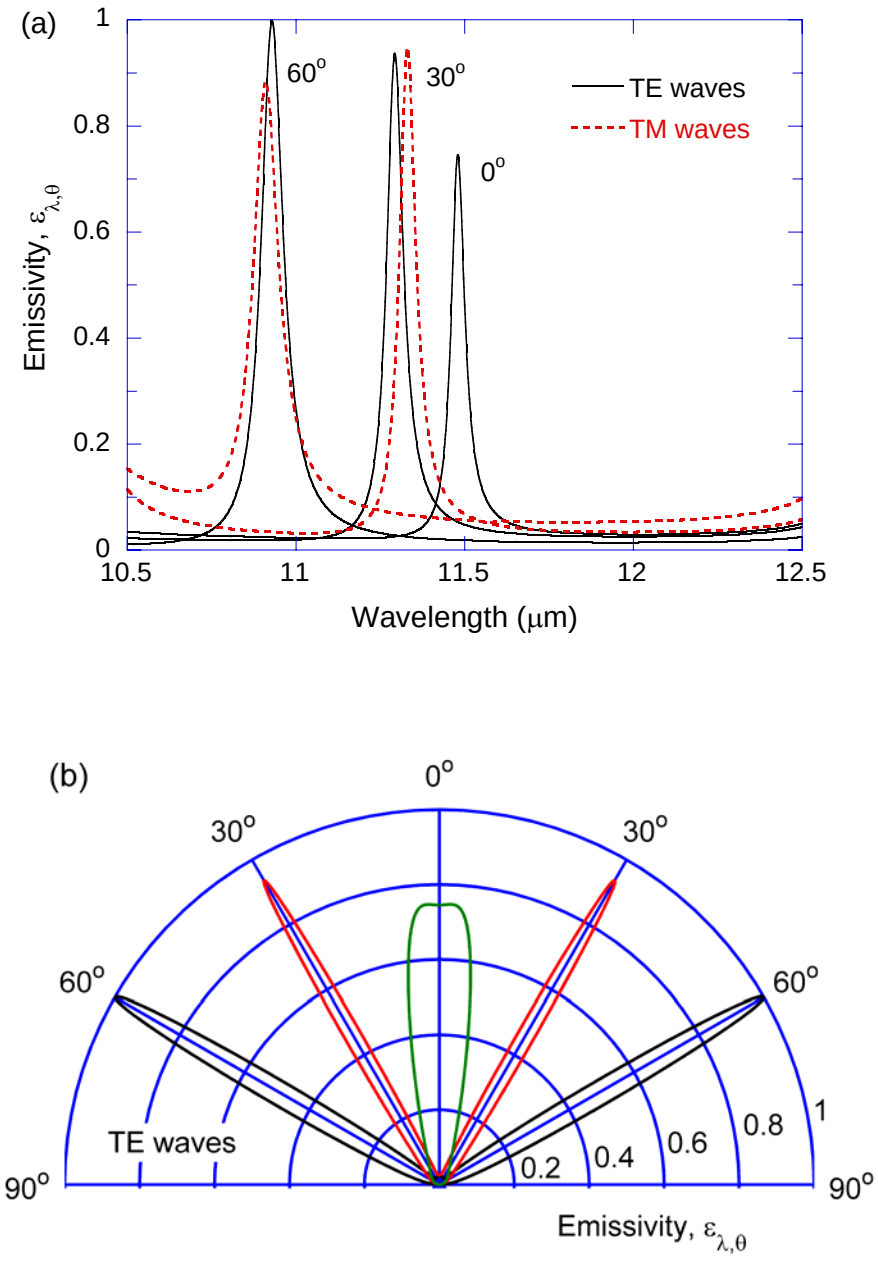

Figure 3.5 The spectral-directional emissivity of the SiC-on-PC structure when surface wave is excited. (a) Spectral dependence at θ = 0°, 30°, and 60° for TE waves (solid lines) and TM waves (dotted lines). (b) Angular distributions at λ_c = 11.479, 11.293, and 10.929 μm for TE waves.

in a very narrow angular region, although the angular spread corresponding to the peak at $\theta = 0°$ is larger than the other two peaks.

The large enhancement of the emissivity is due to excitation of the surface wave. The dispersion relation of surface wave can be obtained using the supercell method described in the previous chapter to determine the resonance wavelength (or frequency) at a given incidence angle. It should be noted that surface waves between SiC and 1D PC are somewhat different from the surface waves due to polaritons. As an example, consider the surface plasmon between air and a metal. Evanescent waves are required in both the metal and air. Therefore, ATR configuration is routinely employed to excite a surface polariton. For the surface wave in PCs, there is no actual evanescent field inside the dielectric layers as discussed in the following.

Figure 3.6 shows the square of the electric field, normalized to the incident, inside the SiC-on-PC structure at normal incidence. The real part of the complex electric field is used to show the actual field inside the structure. The solid line represents the field calculated from the transfer matrix formulation. An oscillating field exists inside the PC, and the amplitude of the oscillating field decays gradually towards larger *z*. The dots represent the electric field obtained using the equivalent layer method, which matches the matrix solutions at the boundaries of each unit cell [40]. The upper panel corresponds to the wavelength ($\lambda = \lambda_c = 11.479\ \mu$m) when a surface wave is excited, and the lower panel corresponds to $\lambda = 11.0\ \mu$m without a surface wave. The field strength at the boundary between the SiC and the PC is enhanced by more than an order of magnitude due to excitation of the surface wave. When a surface wave is excited, the incident energy is resonantly transferred to the surface wave, which causes a large absorption in the SiC. Because SiC is the only material in the structure that can absorb the incident energy, it is

also responsible for the emission of radiation from the SiC-on-PC structure. It is interesting to note that the maximum electric field is slightly off from the interface between the SiC and the PC, which has been observed previously [40]. If a smooth curve is used to connect all the dots shown in Fig. 3.6, it will be the maximum at the SiC-PC interface and decay gradually deep into the PC. Furthermore, the Poynting vector or energy flux in the *z* direction is zero inside the PC at the stop band. Therefore, the effective field inside the PC at the stop band resembles an evanescent wave in a semi-infinite medium. The fact that the field near the SiC-PC interface is greatly enhanced

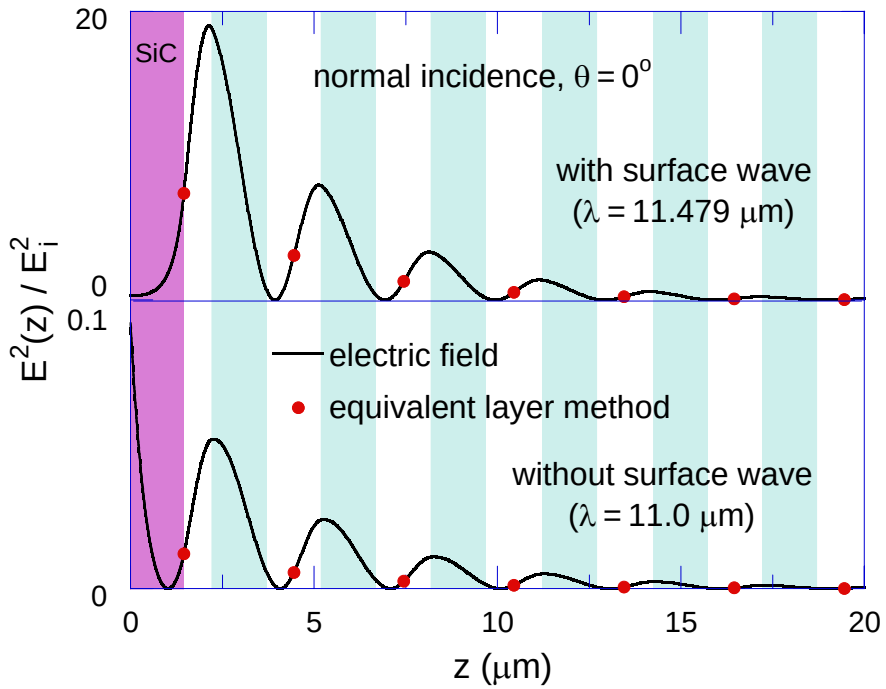

Figure 3.6 The square of the electric field (solid lines), normalized by the incident, inside the SiC-on-PC structure at normal incidence. The dots indicate the field at the boundaries of the unit cell. The upper panel represents the case where a surface wave is excited, whereas the lower panel illustrates a case without a surface wave.

confirms the existence of a surface wave. Further, surface waves at the interface between the SiC and the PC can be excited at any angle of incidence and for both polarizations.

It has been shown that the position where the surface of the 1D PC is terminated largely affects the conditions for the surface wave excitation [38,82]. In Fig. 3.7, the emissivity spectra of the SiC-on-PC structure are plotted for three cases when d_{ter} is equal to $0.6d_{\text{H}}$, $0.5d_{\text{H}}$, and $0.4d_{\text{H}}$ for TE waves. When $d_{\text{ter}} = 0.5d_{\text{H}}$, the geometric parameters of the SiC-on-PC structure are identical to those in Fig. 3.5. It can be seen from Fig. 3.7 that in addition to the resonance wavelengths, the emissivity peak values vary with d_{ter} as well. For example, the emissivity peak value due to surface waves decreases as d_{ter} changes from $0.5d_{\text{H}}$ to $0.6d_{\text{H}}$. On the other hand, when $d_{\text{ter}} = 0.4d_{\text{H}}$ the emissivity values for $\theta = 0°$ and 30° increase, but emissivity for 60° slightly decreases. Similarly, the peak emissivity value changes with the thickness d_{ter} for TM waves. Consequently, the emissivity from the considered structure can be tuned by changing the value of d_{ter}. This is an advantage of the SiC-on-PC structure over the conventional ATR configuration (consisting of a prism, a metal layer, and air) in which surfaces waves can also be excited. In the ATR configuration, the only parameter that can affect the emissivity peak values at the resonance condition is the thickness of the metallic layer next to the prism. However, in the SiC-on-PC structure, the thickness of SiC layer as well as the surface termination determined by the thickness d_{ter} can affect the emissivity values from the structure, which allows more freedom to tune the emissivity.

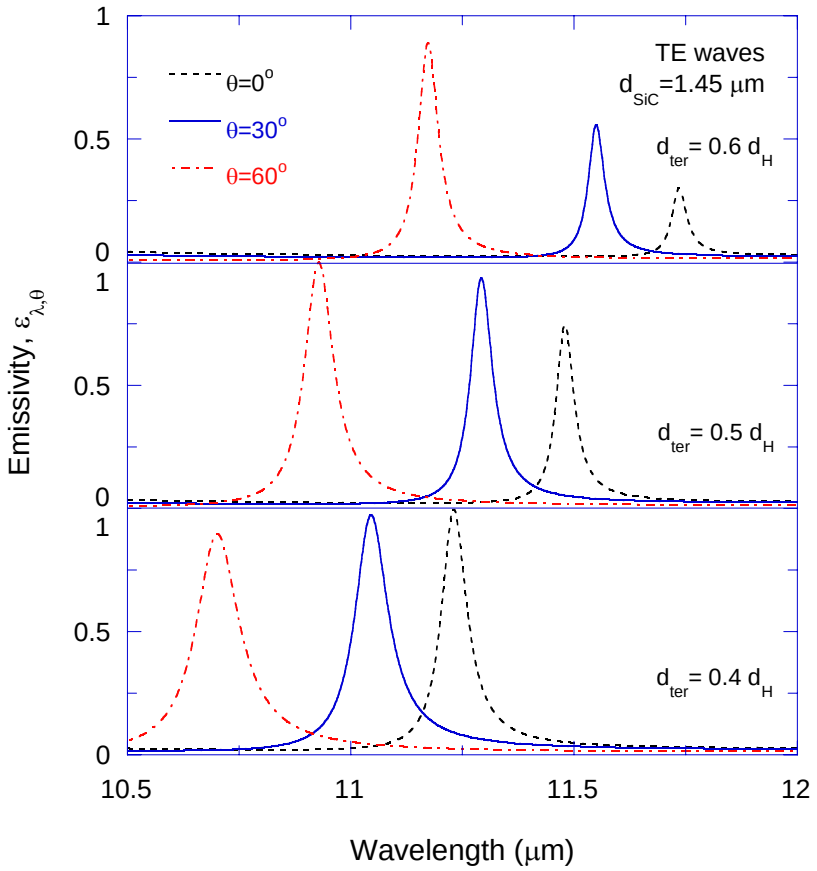

Figure 3.7 The spectral-directional emissivity of the SiC-on-PC structure with different surface termination. The upper panel is the case when surface termination occurs at $d_{ter} = 0.6d_H$. The middle and bottom panels are when $d_{ter} = 0.5d_H$ and $d_{ter} = 0.4d_H$, respectively.

The total thickness of the SiC-on-PC structure is less than 100 μm, which can be deposited using vacuum deposition techniques on a substrate such as silicon. In reality, however, the thickness of the deposited films may vary somewhat depending on deposition conditions. The effects of thickness variation on the emission characteristic can be examined by assuming a random Gaussian variation within ± 150 nm (i.e., up to 10% of the original layer thickness). Note that many thin-film deposition techniques can control the layer thickness within few tens of nanometers. It turns out that very sharp

spectral emission peak can still be achieved at slightly shifted wavelengths from the SiC-on-PC structure. Furthermore, the effects of loss in the dielectric layer are considered using a nonzero extinction coefficient κ. The peak value of emissivity reduces by less than 5% when $\kappa < 0.001$, as compared with the lossless case ($\kappa = 0$). Hence, the effects of the thickness variation and loss in the constituent dielectrics of the 1D PC can be neglected under controlled deposition and for selected dielectric materials.

Cavity Resonance

As seen from Fig. 3.4, the large emissivity due to cavity resonance can be found in the wavelength region between 12.5 μm and 13.5 μm for both polarizations. This region is outside of the SiC phonon absorption band and inside the stop band of the 1D PC. In general, the resonance like that in the Fabry-Pérot etalon can be found in the PC that has a defect layer inside it [15,29], and the resonance mode is called a defect or cavity mode [33]. For example, the 1D PC that has a single layer replaced by a different material can support a cavity mode. In this case, the photonic crystal containing a defect layer can be divided into three parts with respect to the defect layer. In other words, the structure is just like a defect layer sandwiched between two identical PCs, which act as a perfect mirror in the stop band. Consequently, the electromagnetic wave is confined inside the defect layer at the stop band due to high reflection from boundaries, resulting in a large absorption at the resonance condition if the defect layer is an absorbing medium. Recently, Celanovic et al. [16] used a PC on a dielectric cavity deposited on a metallic reflector to achieve coherent emission characteristics.

From the SiC-on-PC structure, a slightly different cavity resonance mode occurs compared to the above example because no defect layer is present inside the 1D PC. The

cavity resonance mode associated with the proposed structure is closer to the simple resonator made of a semitransparent layer [92], which also demonstrates sharp spectral peaks and narrow angular lobes in its emissivity due to wave interference effects in the semitransparent slab. At the wavelength around 12.9 μm where a large emissivity peak appears, the refractive index of SiC is 8.95 and the extinction coefficient is 0.54 (see Fig. 3.2). The reflectivity at the interface between air and SiC is 0.64 for normal incidence. In addition, total reflection occurs from the 1D PC in the stop band. Therefore, the waves are confined in the SiC layer because of high reflection at both boundaries of the SiC slab. At the resonance condition, when standing waves exist in the SiC layer, the reflectance of the SiC-on-PC structure reaches the minimum and results in a large emission because no energy can transmit through the PC in the stop band. Since phase shifts occur during the reflection from the boundaries of SiC due to the nonzero κ_{SiC} value of SiC and the total reflection from the 1D PC, $n_{\mathrm{SiC}}d_{\mathrm{SiC}}$ in the SiC layer at the resonance condition for $\theta = 0°$ is not an exact multiple of the half wavelength as in the simple Fabry-Pérot etalon [89]. In essence, wave interference effects in the SiC layer are essential to enabling the cavity resonance mode in the SiC-on-PC structure, similar to the Fabry-Pérot resonator [15,16,29,92]. Thus, the cavity resonance mode may be excited by either polarization.

For the cavity resonance mode from the SiC-on-PC structure, the emissivity values corresponding to emission angles of 0° and 30° are plotted for both polarizations in Fig. 3.8(a). The geometric parameters of the 1D PC are the same as in Fig. 3.3. In the cavity resonance mode, the wavelength position corresponding to the emissivity peaks does not change much with the emission angle. This is because the refractive index of SiC largely changes with the wavelength; hence, the effect of the polar angle change on

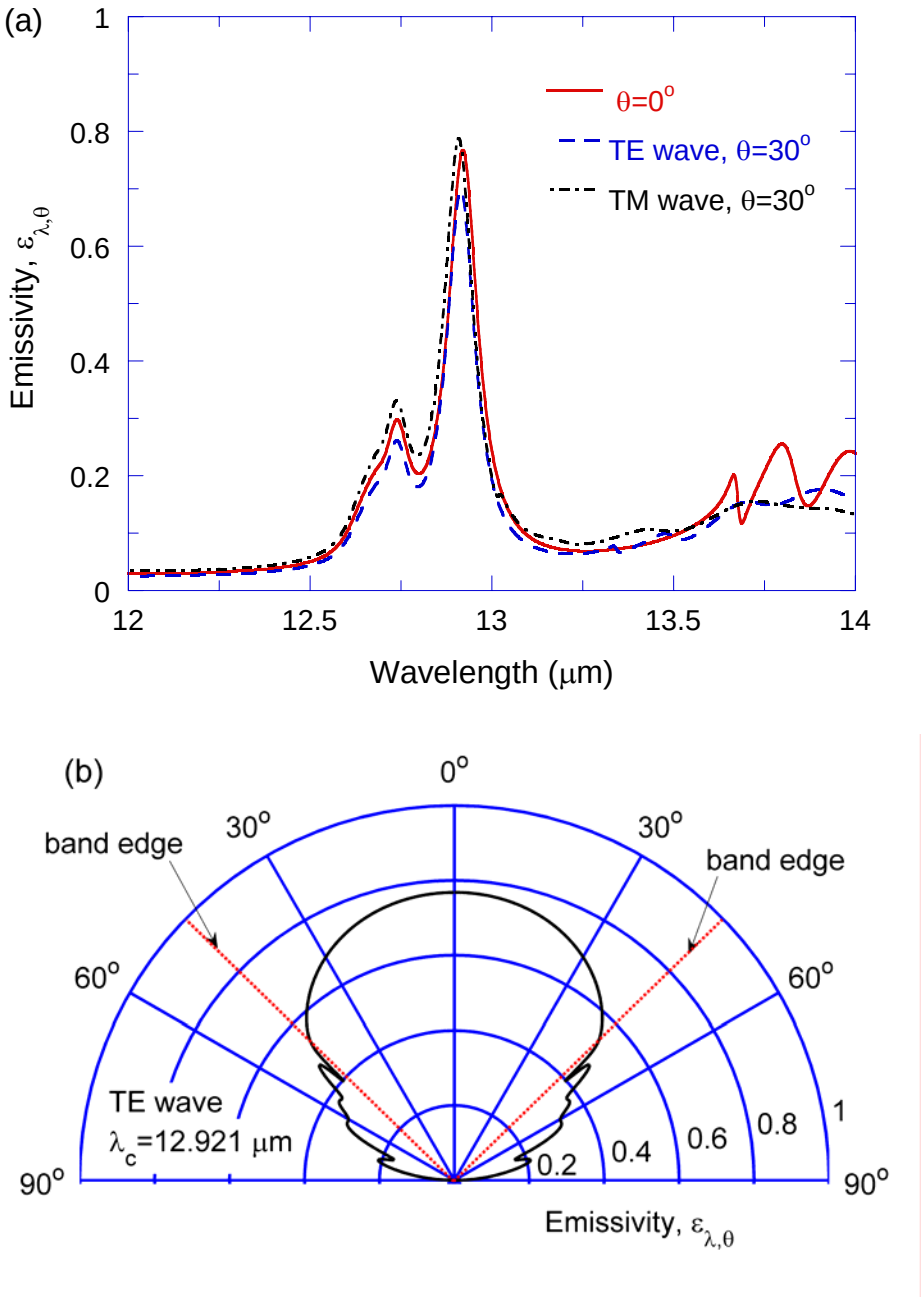

Figure 3.8 The spectral-directional emissivity of the SiC-on-PC structure for the cavity resonance mode. (a) Spectral dependence at $\theta = 0°$, (solid line) and at $\theta = 30°$ for the TE wave (dashed line) and TM wave (dash-dot line). (b) Angular distributions at $\lambda_c = 12.921\ \mu$m for the TE wave.

the phase shift in the SiC layer is compensated by the large change of the refractive index. As a result, the resonance wavelength changes little as the emission angle increases. Moreover, the calculated emissivity spectra reveal that the polarization states do not strongly affect the wavelength where the cavity resonance mode occurs. Similar to the surface wave, the emissivity peaks due to the cavity resonance mode are very sharp. The corresponding quality factors for the largest emissivity peak are 121 at $\theta = 0°$, and 127 or 121 at $\theta = 30°$ for the TE or TM wave, respectively. The angular distribution of the spectral-directional emissivity at $\lambda = 12.921\ \mu\text{m}$, where emissivity peaks are observed in Fig. 3.8(a), is plotted for the TE wave in Fig. 3.8(b). Unlike in the case of surface waves where a narrow angular lobe is found in a certain direction, the diffuse characteristic of the emissivity is obtained from the cavity resonance mode. A similar trend of angular distribution is found for the TM wave. Consequently, the SiC-on-PC structure can be used to produce a large emission either in a certain direction by the excitation of surface waves or in a wide range of the polar angles by the resonance mode, depending on the wavelength region of interest. Notice that the emissivity fluctuates outside the band gap of the PC because of interference effects in the PC.

Figure 3.9(a) shows the normal emissivity spectra for two cases when: (i) the high-refractive-index dielectric ($n_{\text{H}} = 2.4$) is next to the SiC film with $d_{\text{ter}} = d_{\text{H}} / 2$ (identical to the structure in Fig. 3.3), and (ii) the low-refractive-index dielectric ($n_{\text{L}} = 1.5$) is next to the SiC by swapping two types of dielectrics in case (i). For case (i), the surface wave is excited near $\lambda = 11.5\ \mu\text{m}$, and two cavity resonance modes appear in $12.5\ \mu\text{m} < \lambda < 13.5\ \mu\text{m}$. On the other hand, no surface wave is excited for case (ii), and three cavity resonance modes are observed in $12.5\ \mu\text{m} < \lambda < 13.5\ \mu\text{m}$. This is because the

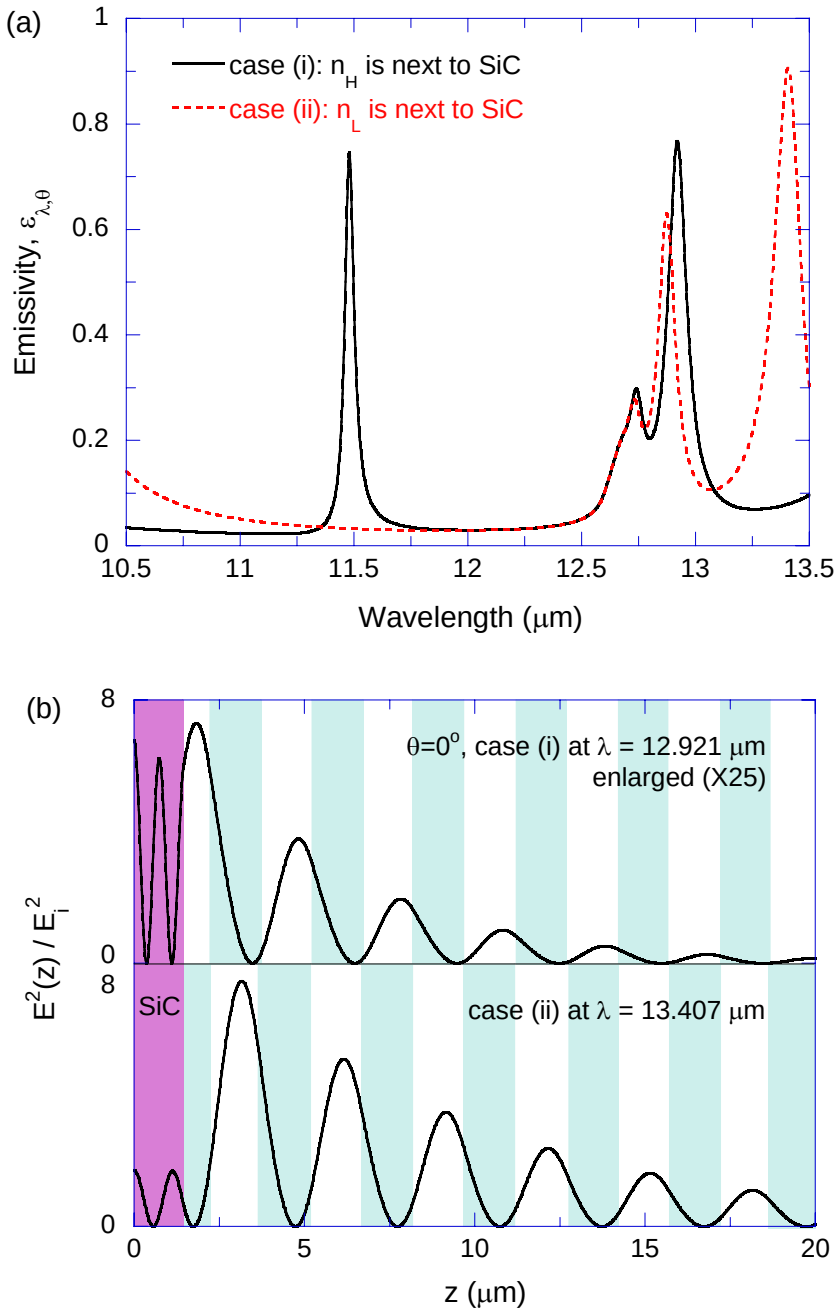

Figure 3.9 Effects of the dielectric located next to the SiC film. (a) Spectral-directional emissivity of the SiC-on-PC structure for two cases when (i) high-index dielectric (solid line) or (ii) low-index dielectric (dashed line) is next to the SiC layer. (b) The square of the electric field, normalized by the incident, inside the SiC-on-PC structure for wavelengths corresponding to two cavity resonance modes. The upper panel of (b) is enlarged by 25 times.

excitation of surface waves strongly depends on the optical constants of the dielectric located next to SiC as well as other parameters, such as angle of incidence, order of the band gap, and polarization. It has been shown that surface waves can also be excited when the lower-index dielectric is located at the surface of the PC for suitable parameters [82]. However, from the given conditions in the present study, the excitation of surface wave is not observable when the lower-index dielectric is next to SiC. Unlike the surface wave excitation, cavity resonance modes appear in both cases, because the band structure of the 1D PC is the same.

When a surface wave is excited, the field decays exponentially into both the SiC layer and 1D PC from the interface as demonstrated in Fig. 3.6. On the other hand, a standing wave exists in the SiC layer when the cavity resonance occurs, as illustrated in Fig. 3.9(b). The upper panel is for case (i) at the resonance wavelength $\lambda_c = 12.921\ \mu\text{m}$; whereas the lower panel is for case (ii) at the resonance wavelength $\lambda_c = 13.407\ \mu\text{m}$. Notice that the field in the upper panel is enlarged 25 times for clear illustration. For instance, the actual value of the square of the electric field in the upper panel is $7.3/25 = 0.292$ at the maximum. While the emissivity peak for case (i) at $\lambda_c = 12.921\ \mu\text{m}$ is slightly smaller than that for case (ii) at $\lambda_c = 13.407\ \mu\text{m}$, the field strength in the upper panel is significantly lower than that in the lower panel. Because both peaks are within the stop band of the PC, the effective evanescent behavior of the electric field inside the PC is manifested by the oscillating amplitude that decays from left to right. It can be shown that the transmittance of the PC (with a total thickness of 90 μm for 30 periods) is nearly zero, indicating that no energy is transferred through the PC.

The Brewster Modes

From Fig. 3.4(b), an emissivity enhancement is found for TM waves around $\lambda = 10.3\ \mu\text{m}$, which is distinguished from TE waves. In this case, the enhancement of emission is due to the Brewster mode. Figure 3.10(a) shows the emissivity spectra when the thickness of SiC layer is 0.5, 1.45, and 2.5 μm at $\theta = 30°$ for TM waves. The emissivity for the TE wave when $d_{\text{SiC}} = 1.45\ \mu\text{m}$ is also plotted for comparison. It is clear that the emissivity enhancement due to the Brewster mode occurs only for TM waves, and the SiC layer thickness affects the emissivity peak values and their positions.

The conditions for the Brewster mode are more complicated than those for the cases of the surface-wave excitation and cavity resonance. Most importantly, the Brewster mode occurs ideally when the Fresnel reflection coefficient at the interface between SiC and 1D PC is zero [91]. When the reflection coefficient at SiC-PC interface is zero, the reflectance of the SiC-on-PC structure is simply equal to the reflectivity at the air-SiC interface. At the same time, if the reflectivity at the air-SiC interface is small, then the reflectance of the SiC-on-PC structure becomes low. A reduction in the reflectance implies an increase in the emissivity since the transmittance is zero in the stop band. To further understand the Brewster mode, the case with $d_{\text{SiC}} = 1.45\ \mu\text{m}$ is considered in which the emissivity peak is located at $\lambda_c = 10.29\ \mu\text{m}$. At this wavelength, the refractive index of SiC is less than unity as seen from the inset of Fig. 3.2, and so that evanescent waves exist in the SiC layer for $\theta = 30°$. It is important to note that the reflection coefficient at the SiC-PC interface is not exactly equal to zero because of the nonzero κ_{SiC} value. Therefore, in the SiC layer, there exists a backward-decaying

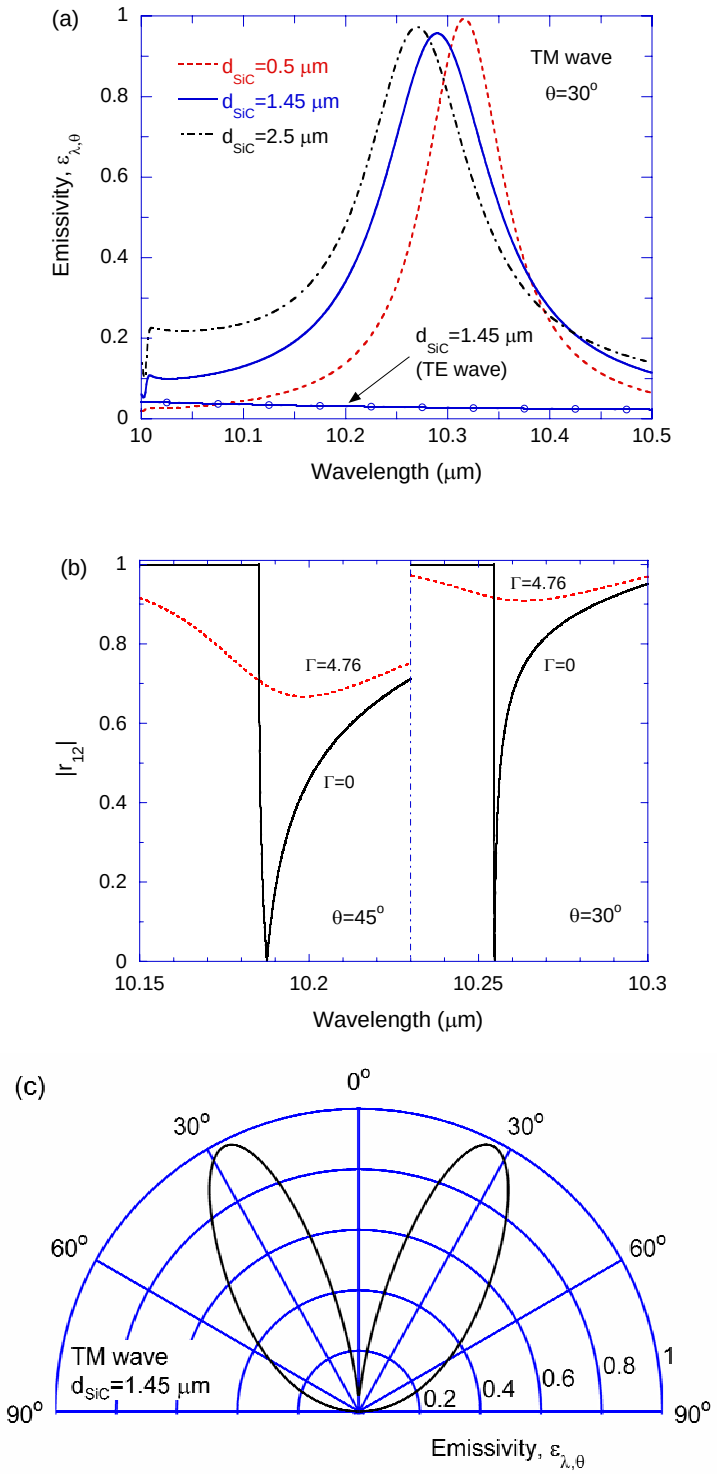

Figure 3.10 The spectral-directional emissivity of the SiC-on-PC structure for the Brewster mode. (a) Spectral dependence when d_{SiC} is 0.5, 1.45, and 2.5 μm at $\theta = 30°$ for TM waves. The solid line with circular marks is for the case when d_{SiC} = 1.45 μm for the TE wave. (b) Magnitude of the complex reflection coefficient at the SiC-PC interface for TM waves with (dashed line) or without (solid line) damping. (c) Angular distributions at λ_c = 10.29 μm when d_{SiC} = 1.45 μm for the TM wave.

evanescent wave reflected from the SiC-PC interface. Consequently, the emissivity peak values and positions are strongly affected by the coupling effects between the forward and backward evanescent waves in the SiC. This is why the emissivity peak value and position depend strongly on the SiC layer thickness, as illustrated by Fig. 3.10(a).

The magnitude of the complex reflection coefficient between SiC and 1D PC is plotted in Fig. 3.10(b) for $\theta = 30°$ and 45°. The complex reflection coefficient at the SiC-PC interface $\overline{r}_{12}$, where the subscripts 1 and 2 represent SiC and 1D PC, respectively, can be calculated by using the equivalent layer method [40,93]. For illustration, $|\overline{r}_{12}|$ at $\theta = 45°$ is plotted on the left side in 10.15 μm < λ < 10.23 μm, whereas $|\overline{r}_{12}|$ at $\theta = 30°$ is shown on the right side in 10.23 μm < λ < 10.3 μm, separated by a vertical dash-dot line. The cases with $\Gamma = 0$ (no damping) in Eq. (3.1) are plotted as solid line for comparison with the actual $|\overline{r}_{12}|$ shown as dashed line. When damping is neglected, the reflection coefficient at the SiC-PC interface goes down all the way to zero at the wavelength close to the emission peaks. On the other hand, a rather large $|\overline{r}_{12}|$ exists if damping is considered, suggesting that the amplitude of the backward evanescent wave is indeed comparable to that of the forward evanescent wave. Consequently, the emissivity peak location depends on the thickness of SiC layer due to the coupling of evanescent waves.

The angular distribution of the emissivity at $\lambda_c = 10.29$ μm is plotted in Fig. 3.10(c) when $d_{SiC} = 1.45$ μm. Emissivity values greater than 0.6 are found in the emission angles approximately from 15° to 45°. Compared to the surface wave excitation shown in Fig. 3.5(b), the angular lobe in the Brewster mode is much wider. On the other

hand, the angular distribution of the emissivity from the Brewster mode is not as diffuse as that from the cavity resonance mode, which exhibits almost constant emissivity of 0.7 in the emission angles from 0° to 45°, as plotted in Fig. 3.8(b). As a result, the angular distribution of emission from the SiC-on-PC structure largely depends on which mode is excited. Again, the Brewster mode is distinguished from the surface-wave excitation and cavity resonance, such that it is observable only for TM waves. Hence, the applicability of the emission source utilizing the Brewster mode is inevitably limited to TM waves, like binary gratings when the direction of emission is perpendicular to the grating grooves.

The spectral-hemispherical emissivity of the SiC-on-PC structure is plotted in Fig. 3.11 for both polarizations. The spectral-hemispherical emissivity is obtained by integrating the spectral-directional emissivity $\varepsilon_{\lambda,\theta}$ over the hemisphere [1]:

$$\varepsilon_{\lambda} = 2 \int_{0}^{\pi/2} \varepsilon_{\lambda,\theta}(\theta) \cos\theta \sin\theta d\theta \tag{3.2}$$

Due to the axial symmetry of the planar structure, the emission is independent of the azimuthal angle, unlike the case for 1D gratings. Notice that the electric field for the TE wave is defined to be parallel to the unit direction vector of the azimuthal angle at any point on the surface. For the TE wave, large values of the spectral-hemispherical emissivity are found in Regions I and II. The enhancement in Region I due to the excitation of surface waves is not as large as that in Region 2 at the cavity resonance mode. This is because cavity resonance enables a diffuse emitter whereas surface waves induce a large emission into a narrow angular region. For the TM wave, very similar trends are found in Regions I and II. However, a large enhancement of the hemispherical

emissivity is also seen in Region III because of the Brewster mode, since the angular lobe of the spectral-directional emissivity from the Brewster mode is much wider than that due to surface waves.

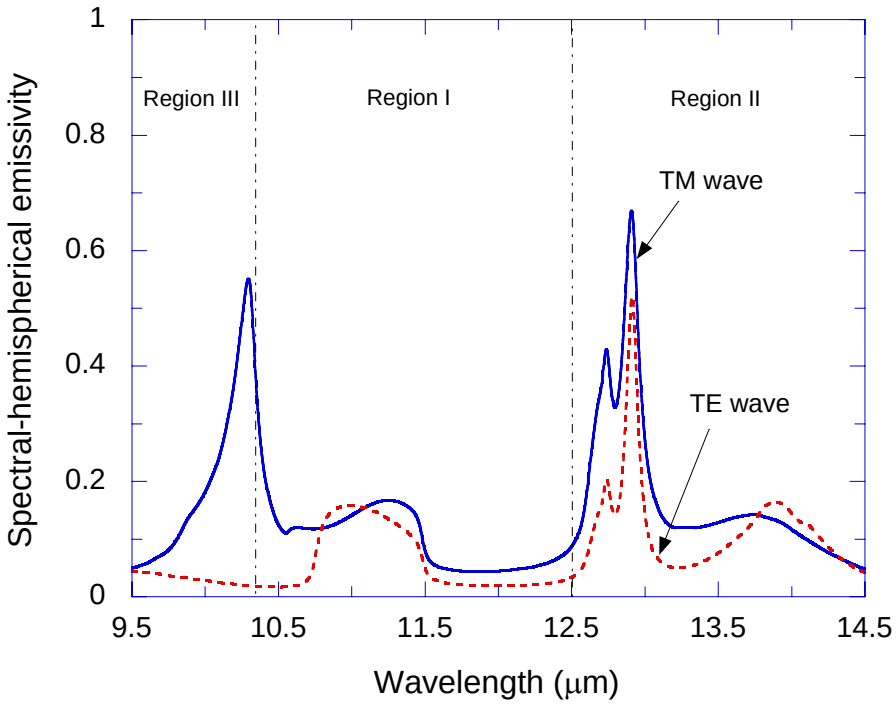

Figure 3.11 The spectral-hemispherical emissivity of the SiC-on-PC structure.

CHAPTER 4

DESIGN AND FABRICATION OF COHERENT EMISSION SOURCE IN NEAR-INFRARED

In the previous chapter, the SiC-on-PC structure was identified as a coherent emission source and its emission characteristics were extensively investigated. To fabricate such a structure, there are several issues to be considered in reality. First of all, one needs to deposit 1.5-μm-thick dielectric films to construct a semi-infinite 1D PC. Since 30 unit cells are involved in the SiC-on-PC structure, a total of 60 layers are required to be deposited. In addition, deposition methods for dielectrics such as ZnSe ($n \approx 2.4$) and KBr ($n \approx 1.52$) are rather limited as compared to SiO_2 or Si_3N_4. Therefore, we propose an alternative but much simpler structure to experimentally demonstrate the concept of coherent emission sources.

This chapter describes the design and fabrication of two planar multilayer structures as coherent thermal emission sources that exhibit both temporal and spatial coherence in the near-IR. The first structure involves the 1D PC with finite number of unit cells on a metal, such as Ag and is illustrated in Fig. 4.1(a). It will be called as the PC-on-Ag structure hereafter. The thickness d_{ter} determines the surface termination of the 1D PC adjacent to Ag. Even though the employed PC is not semi-infinite and consists of several unit cells only, evanescent waves can exist inside the truncated PC in the stop band. Hence, surface waves are supported at the interface between the 1D PC and Ag. Compared to the previous structure, where a thin SiC film is coated on the semi-infinite 1D PC [80,81], the PC-on-Ag structure requires far fewer layers and thus, is much easier

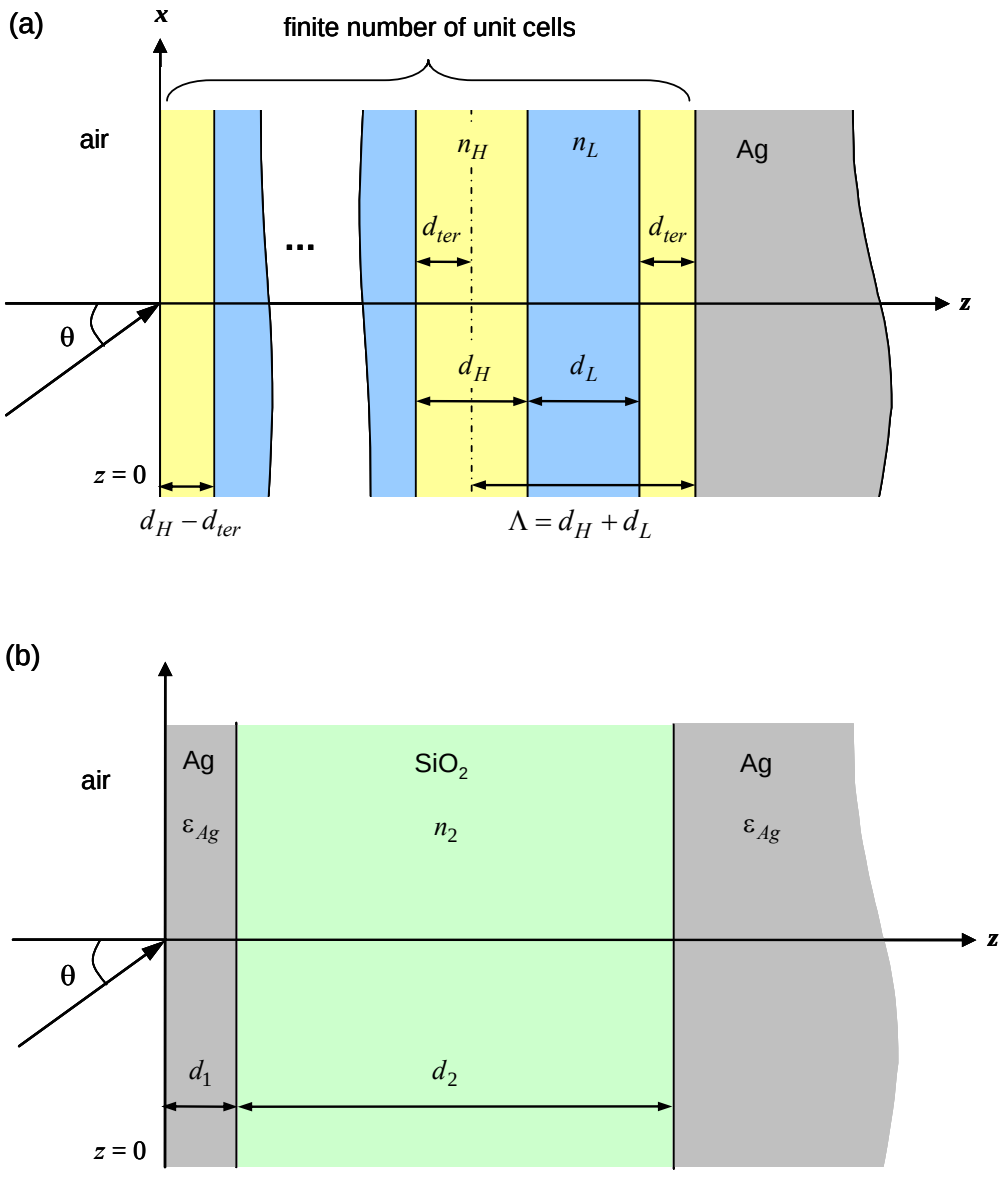

Figure 4.1 Schematics of the proposed coherent emission sources: (a) A PC-on-Ag structure made of a 1D PC with few unit cells coated on a thick Ag film. The thickness d_{ter} determines the surface termination of the PC adjacent to the Ag layer. (b) Asymmetric Fabry-Pérot resonance cavity made of a SiO_2 film with Ag coatings on both sides. The thickness of the Ag layer located on the left is d_1, and that on the right is assumed to be semi-infinite.

to manufacture. The second structure is an asymmetric Fabry-Pérot resonance cavity made of a dielectric layer with highly reflective coatings on both sides, as shown in Fig. 4.1(b). By using highly reflective materials on both sides of the dielectric layer, the present study demonstrates both temporal and spatial coherence in the near-IR spectral regions. Furthermore, conditions that influence coherent emission characteristics from both proposed structures are investigated. The band structure of the truncated PC is analyzed by comparing it with that of the semi-infinite PC. Based on the calculated results, the proposed structures were designed and fabricated using thin-film deposition techniques.

Reflectance of Truncated Photonic Crystals

Since the PC-on-Ag structure involves the truncated PC with few unit cells, it is important to understand the band structure of the truncated PC. Figure 4.2(a) shows the reflectance spectra of PCs at normal incidence in the vicinity of a stop band. The dotted line represents the reflectance of a PC with 30 unit cells ($N = 30$), and the solid line is for a PC with six unit cells ($N = 6$). The shaded region stands for the stop band of the semi-infinite PC obtained by solving the Bloch wavevector based on the transfer matrix formulation [81]. In the calculation, the constituent dielectrics of the PC are chosen as Si_3N_4 and SiO_2, whose refractive indices are approximately $n_H = 2.0$ and $n_L = 1.45$, respectively in the considered spectral region [94], and the thicknesses of dielectrics are set to be $d_H = d_L = \Lambda / 2$. The stop band of the PC is scaled by changing Λ to locate approximately 1 μm in the near-IR spectral region. Consequently, the period $\Lambda = 300$ nm is selected for the use in Fig. 4.2(a). From the reflectance spectrum, the stop band of the PC with $N = 30$ can be thought as the spectral region where the reflectance becomes

unity. Note that interference effects cause some oscillations in the reflectance spectrum at the frequency ($\nu = 1/\lambda$) regions lower than 8750 cm^{-1} and higher than 10630 cm^{-1}, i.e., in pass bands. The reduction in the reflectance is associated with an increase in the transmittance through the finite-thickness PC.

For $N = 6$, although the band edge is not well-defined in the reflectance spectrum, the stop band still exists in the region where the reflectance is close to unity. This is clear from the fact that the spectral band of large reflectance is much wider in the stop band than that normally found in the pass band due to interference effects. Interestingly, the stop band of the PC with $N = 6$ appears shifted a little towards higher frequencies, compared to that of the semi-infinite PC. This is caused by interference effects as explained below. The square of the electric field, normalized to that of the incidence, is plotted inside the PC with $N = 6$ at normal incidence, in Fig. 4.2(b). The upper panel is the field distribution at $\nu = 10000$ cm^{-1} (in the stop band), and the lower panel is the case at $\nu = 11000$ cm^{-1} (in the pass band). It can be seen from Fig. 4.2(a) that reflectance values are close to 0.9 for both cases. In terms of the field distribution in Fig. 4.2(b), the upper panel clearly shows the effective evanescent wave. In a semi-infinite PC, the effective evanescent wave does not carry energy; thus no energy can transmit through a semi-infinite PC in the stop band even though an oscillating field exists inside the PC. On the other hand, the small number of periods does not guarantee zero transmission at $\nu = 10000$ cm^{-1}. Therefore, the reflectance in the stop band of the truncated PC is generally less than unity. The lower panel of Fig. 4.2(b) shows that the amplitude of the electric field for $\nu = 11000$ cm^{-1} is rather amplifying from $z = 0$ to 1.0 μm and then

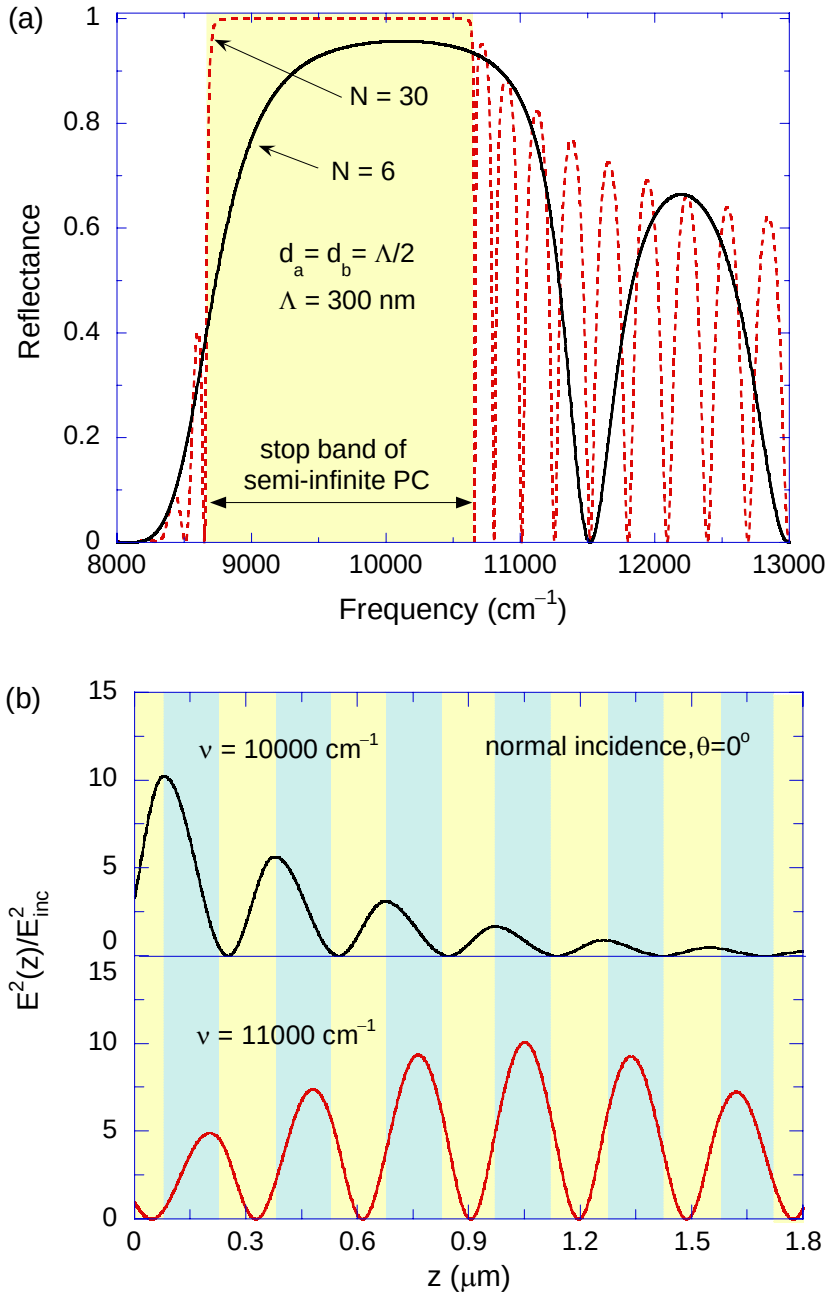

Figure 4.2 Characteristics of PCs of finite numbers of periods: (a) Reflectance spectra in the vicinity of the stop band. The solid line stands for the case when N = 6, i.e., six unit cells, and the dotted line is for the case with N = 30. The stop band of the semi-infinite 1D PC is represented by the shaded region. (b) The square of the electric field, normalized by that of the incident wave, inside the PC for N = 6 at normal incidence. The upper panel is for the case of ν = 10000 cm^{-1} (stop band), and the lower panel is for ν = 11000 cm^{-1} (pass band).

decreasing as z approaches 1.8 μm. This observation implies that the field distribution is a part of the Bloch wave, which propagates through the PC in the pass band. In other words, the high reflectance at $\nu = 11000$ cm^{-1} is due to wave interference effects in thin films.

Prediction of Coherent Emission from the PC-on-Ag Structure

In order to excite the surface wave, evanescent waves are required in both media. Notice that effective evanescent waves exist for both polarizations in the stop bands of PCs regardless of the angle of incidence or emission angle when emission rather than absorption is considered. Therefore, a 1D PC is used to directly couple propagating waves from air in the left half space (i.e., $z < 0$; refer to Fig. 4.1) to the surface wave. In terms of the frequency tuning, metals have advantage over polar materials because most of metals have plasma frequency in the ultraviolet region. Thus, there exist evanescent waves in metals in the wide near-IR region. Recall that the spectral region for the stop band of PCs can be easily modified by scaling the period. To demonstrate the feasibility, Ag is selected in the present study. The optical constants of Ag are taken from the tabulated values [94]. Notice that a Ag film can be deposited on a suitable substrate, such as a silicon wafer, and it can be treated as a semi-infinite medium when its thickness exceeds about 200 nm (i.e., much greater than the radiation penetration depth).

The major advantage of the PC-on-Ag structure over the SiC-on-PC structure is the use of PCs with fewer unit cells. In the PC-on-Ag structure, induced evanescent waves at $z = 0$ in the stop band should be able to reach the interface with Ag to excite surface waves. For this reason, care should be taken when determining the number of unit cells for the truncated 1D PC. As illustrated in Fig. 4.2(a), the finite-thickness PC

asymptotically shows the stop bands in terms of the reflectance spectrum. As the number of periods N increases, the reflectance in the stop band reaches unity, and the band edge becomes more obvious. It should be noted that if the reflectance is less than unity in the stop band, then some portion of incident energy propagates into the PC, and the wave inside the PC starts to lose evanescent characteristics. Therefore, the number of periods must be sufficiently large, so that the finite-thickness PC properly shows the stop band. On the other hand, the effective evanescent wave, which is coupled to propagating waves in air, is localized near the surface at $z = 0$ [33]. In general, an electric field inside a slab can be thought of as a summation of the forward (propagating or decaying to the positive-z direction) and backward (propagating or decaying to the negative-z direction) waves. If N is too large, forward evanescent waves decaying from $z = 0$ cannot reach the right surface of the finite-thickness PC. In this case, surface waves cannot be supported because no backward evanescent wave exists at the interface between the 1D PC and Ag. Notice that the surface wave at the PC-Ag interface is associated with the backward evanescent wave in the PC. Consequently, the number of periods must be optimized to enable surface waves at the interface between the 1D PC and Ag. For the considered PC-on-Ag structure, calculations show that the optimal N is six for coherent thermal emission.

Figure 4.3(a) shows the spectral-directional emissivity of the PC-on-Ag structure at $\theta = 0°$, $30°$, and $60°$ for both polarizations. In order to locate the stop band in the near-IR spectral region, the period of the 1D PC is scaled to $\Lambda = 300$ nm. For simplicity, the thickness of two dielectrics are assumed to be the same $d_{\mathrm{H}} = d_{\mathrm{L}}$, and the thickness d_{ter} is found to be $0.6d_{\mathrm{H}}$ that will maximize the emissivity peak values for TE waves. With the given geometric parameters, the emissivity peak values are very high, except in

the case of TM wave at $\theta = 60°$, which is close to 0.3. For TE waves, as an example, very sharp emissivity peaks are found in a narrow spectral band centered at $\nu_c = 10232$, 10718, and 11940 cm^{-1} for emission angles of $\theta = 0°$, $30°$, and $60°$, respectively. The corresponding quality factor of the emissivity peaks are 99, 124, and 208 for $\theta = 0°$, $30°$, and $60°$, respectively, and these values are comparable to those from previous studies [17,81,95]. Notice that wave interference effects cause some oscillations in the pass band, but resulting emissivity values are very small compared to those due to the surface wave excitation in the stop band.

The angular distribution of the spectral-directional emissivity from the PC-on-Ag structure is plotted in Fig. 4.3(b) at three peak frequencies for TE waves. The spatial coherence of thermal emission is apparent from the high directionality in the plot. For TE waves, the FWHM $\Delta\theta$ is estimated as 19.43°, 2.77°, and 1.35° for emission angles of $\theta = 0°$, $30°$, and $60°$, respectively. Except for the normal direction, excellent directional selectivity is found for TE waves. Although it is not shown, the angular distribution of the emissivity for TM waves is very similar at corresponding peak frequencies except for $\theta = 60°$, where the peak emissivity is only 0.3. Notice that the thickness d_{ter} affects emissivity peak values, and thus, it can be tuned to maximize the emissivity at $\theta = 60°$ for TM wave. However, for Figs. 4.3(a) and 4.3(b), the thickness d_{ter} has been set as $0.6d_H$ by optimizing the emissivity for TE waves, which results in the close-to-unity emissivity at $\theta = 30°$ and $60°$ for TE wave and lower emission peaks at other conditions.

In order to ascertain that surface waves are excited at the interface between the truncated 1D PC and Ag, the square of the normalized electric field inside the PC-on-Ag structure is plotted in Fig. 4.4 at normal incidence. The upper panel corresponds to

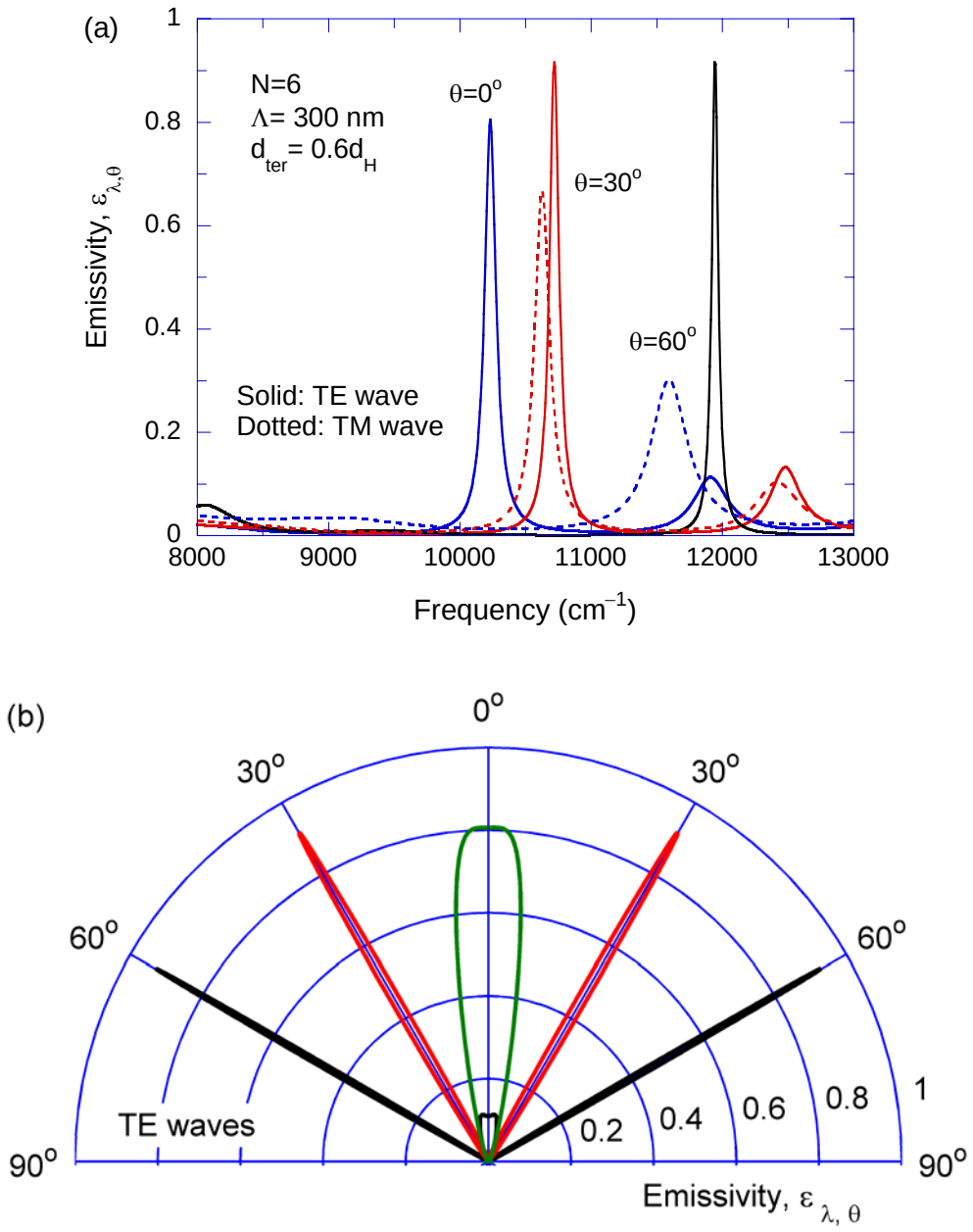

Figure 4.3 The emissivity $\varepsilon_{\lambda,\theta}$ of the PC-on-Ag structure: (a) Spectral emissivity at $\theta = 0°$, 30°, and 60° for TE waves (solid lines) and TM waves (dotted lines). Here, Λ = 300 nm, $N = 6$, $d_H = d_L = \Lambda/2$, and $d_{ter} = 0.6d_H$. (b) Angular distribution of the emissivity at three peak frequencies for TE waves. The emissivity peaks corresponding to emission angles of $\theta = 0°$, 30°, and 60° are centered at ν_c = 10232, 10718, and 11940 cm^{-1}, respectively.

$\nu = 10232$ cm^{-1} where the large emissivity peak is found, and the lower panel is for $\nu = 9000$ cm^{-1} where the corresponding emissivity is less than 0.01. Here, evanescent waves are expected inside the PC for both frequencies because they correspond to the stop band. It is clear that the lower panel mainly shows forward evanescent waves coupled to propagating waves incident from air. The square of the electric field in the lower panel is enlarged by factor of 10 for clear illustration. Since the total thickness of the PC with $N = 6$ is relatively thick, backward evanescent waves reflected from the right surface of the PC is negligible compared to forward evanescent waves. On the other hand, backward evanescent waves are dominant for the upper panel. This is because surface waves are excited at the interface between the 1D PC and Ag. When surface

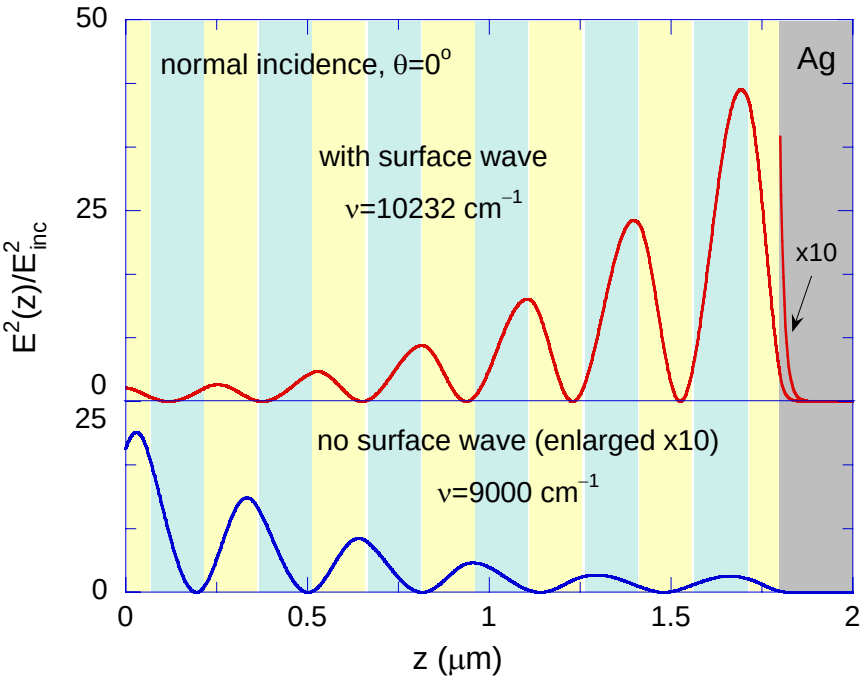

Figure 4.4 The square of the electric field, normalized by that of the incidence, inside the PC-on-Ag structure. The upper panel represents the case when a surface wave is excited, and the lower panel is for the case without a surface wave.

waves are excited, evanescent waves associated with the surface wave decay from the PC-Ag interface into both media, and the electric fields inside the media are greatly enhanced due to resonance features of the surface wave. Therefore, it is natural that backward evanescent waves associated with the surface wave are dominant in the 1D PC. Because the radiation penetration depth of Ag is very small compared to the length scale of the 1D PC, the square of the electric field in the Ag layer is multiplied by 10 to clearly illustrate the exponentially decaying field inside it. It should be noted that when surface waves are excited, the incident energy is resonantly transferred to the Ag layer, resulting in a large emissivity at the resonance frequency. The maximum of the electric field is slightly off from the interface between the 1D PC and Ag, which has been also observed previously [39,80]. This could be explained as due to the nature of the effective or oscillating evanescent wave. Based on the field distribution and considerable enhancement of the field strength, it can be concluded that the surfaces waves are certainly excited at the interface between the 1D PC and Ag at $\nu = 10232\ \text{cm}^{-1}$.

Fabrication of the PC-on-Ag Structure

To demonstrate the feasibility of the proposed structure as a coherent thermal-emission source, the samples were fabricated using vacuum deposition techniques. A Si wafer of 100 mm diameter was used as a substrate. For the PC-on-Ag structure, a Ag film was coated up to 200 nm by sputtering deposition on the substrate with a thin Ti adhesive layer. Since the thickness of this Ag layer is much greater than the radiation penetration depth, the optical properties of Ti film and Si substrate do not affect the emissivity of the PC-on-Ag structure. The 1D PC with $\Lambda = 300$ nm was formed on top of the Ag layer using plasma enhanced chemical vapor deposition (PECVD). Both SiO_2 and Si_3N_4 were

deposited at a temperature of 250°C, and deposition processes of all layers were performed during one thermal cycle without breaking a vacuum environment; however, a 5-minute nitrogen purge was applied in between the deposition of each layer to purge remaining chemical gases from the chamber.

Figure 4.5 shows the cross-sectional image of the fabricated PC-on-Ag structure obtained using a focused ion beam (FIB) workstation. Initially, we attempted to use SEM to image the cross-sections, but the images did not show sufficient contrast between the two dielectrics. In the FIB image, the layered structure shows alternating brightness and is marked with colored blocks to indicate different materials. A schematic of the PC-on-Ag structure is shown to illustrate the view angle on the right of the FIB image. Because the view angle is not normal to the surfaces, the surface of the Si_3N_4 top layer also shows up in the image. The thicknesses of the upper layers look slightly greater than the underneath layers. This could be caused by the FIB imaging process, in which gallium ion (Ga^+) was used for milling a hole to expose the cross-section as well as for taking its image. Thus, the top layers may have been milled further while the image was taken.

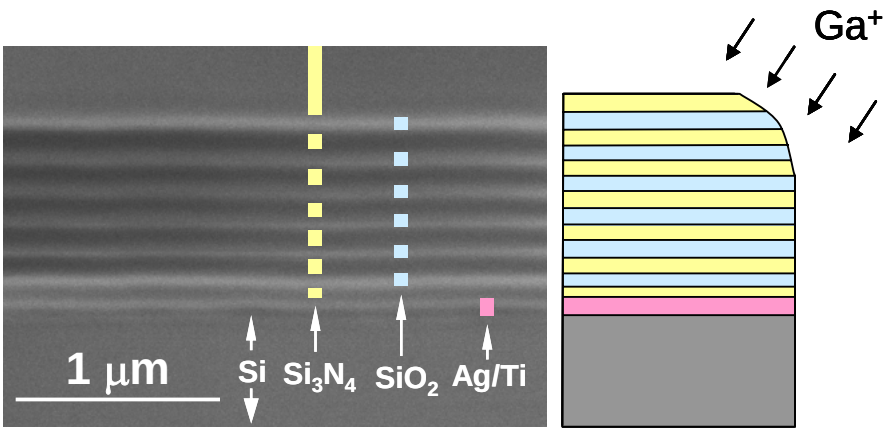

Figure 4.5 FIB image of the cross-section for the fabricated PC-on-Ag structure. A schematic is shown on the right of the image for clarity.

A Digital Instruments Multimode^{TM} atomic force microscope (AFM) was used to measure the surface roughness of the PC-on-Ag structure. The AFM scans the top surface of the fabricated sample with a sharp silicon cantilever in the contact mode. The radius of the cantilever tip is known to be around 10 nm based on manufacturer's specification (mikromash catalog 2007). The sample was cleaned with acetone and nitrogen gas before the scanning. The scan area was $10\ \mu\text{m} \times 10\ \mu\text{m}$, and the measured height data was stored in a 512×512 array. The scanning speed was 1 Hz for the acquisition of 512 data. Figure 4.6(a) shows the measured topography of the top surface of the fabricated sample. For two specimens that were diced into $0.5\ \text{mm} \times 0.5\ \text{mm}$ size from the coated wafer, the root-mean-squared roughness was estimated by four separate measurements to be 9.1 ± 0.4 nm and 11.7 ± 0.7 nm, respectively. In order to investigate the effect of surface roughness on the radiative properties, the bidirectional reflectance distribution function (BRDF) was measured in the vicinity of the specular direction by using a custom-designed laser scatterometer. The measurement was conducted with a laser diode of 635 nm wavelength at 30° incidence angle for the TM wave. The details of the scatterometer will be provided in the next chapter. Figure 4.6(b) shows the measured BRDF of the PC-on-Ag structure (solid line with triangles). For the comparison purpose, the BRDF of a double-side-polished Si wafer, whose root-mean-squared roughness was measured to be less than 1 nm, is also plotted (dashed line with circles). It was found that the scattering from the PC-on-Ag structure increases by a factor of twenty as compared to that from the polished Si wafer, due to the surface roughness. However, scattered lights from the sample are still five orders of magnitude smaller than the specular reflectance. Therefore, the effect of surface roughness of the fabricated sample can be neglected.

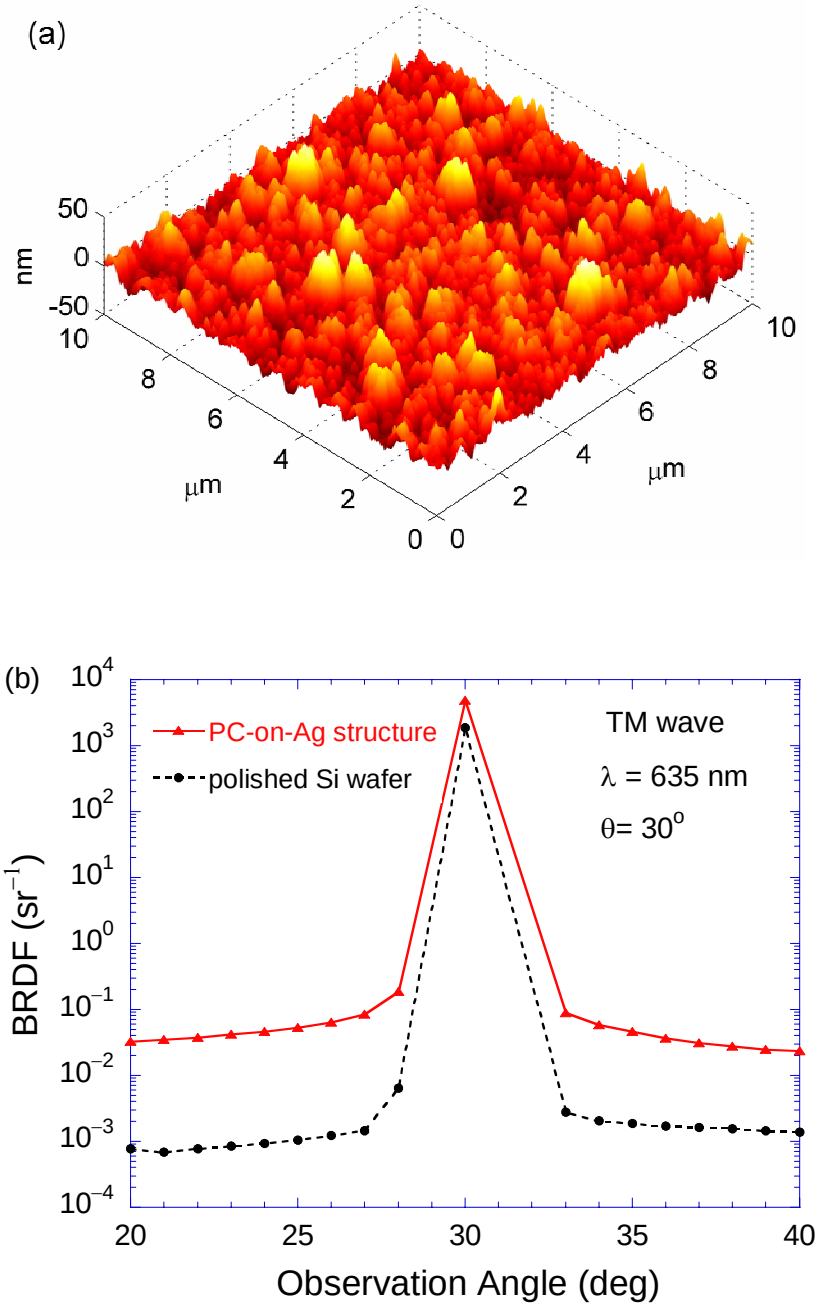

Figure 4.6 Surface roughness of the fabricated PC-on-Ag structure: (a) AFM topography of the top surface; (b) Measured BRDF of the sample at 635 nm wavelength and 30° incidence angle for the TM wave.

Reflectance of the Asymmetric Fabry-Pérot Resonance Cavity

An alternative design of the coherent-thermal emission source is an asymmetric Fabry-Pérot resonance cavity, as shown in Fig. 4.1(b). Unlike the conventional Fabry-Pérot resonator made of two parallel reflectors separated by at a finite distance, the considered structure employs a dielectric film coated with highly reflective materials of different thicknesses. Here, “asymmetric” emphasizes that the geometry of reflectors are not symmetric with respect to the cavity. In general, high reflection from the boundaries of the resonance cavity is essential for the sharp spectral peak at the resonance condition [68]. In the present study, we employed SiO_2 to form the cavity and Ag as the reflective coating. Although similar structures were considered by others [19,96], the spectral emission peaks are too broad without sharp angular lobes.

Figure 4.7(a) shows the spectral-directional emissivity of the Fabry-Pérot cavity depicted in Fig. 4.1(b) for the near-IR spectral region at normal incidence. In the calculation, the cavity thickness is set to be 2.0 μm, and the Ag film on the right side of the cavity is assumed to be semi-infinite by setting its thickness much greater than the radiation penetration depth. The thickness of the front Ag film cannot be much greater than the radiation penetration depth to enable transmission of the incident wave into the cavity. It was found that a 15 nm Ag film can maximize the emissivity peaks. In Fig. 4.7(a), the emissivity without the 15-nm-thick Ag film is also plotted for comparison. At the resonance frequency, where standing waves exist inside the dielectric cavity, very sharp emissivity peaks are found with the thin Ag film. The resonance features due to wave interference effects are clear from the fact that multiple emissivity peaks are found in the considered spectral region. Without the front Ag film, the resulting emissivity

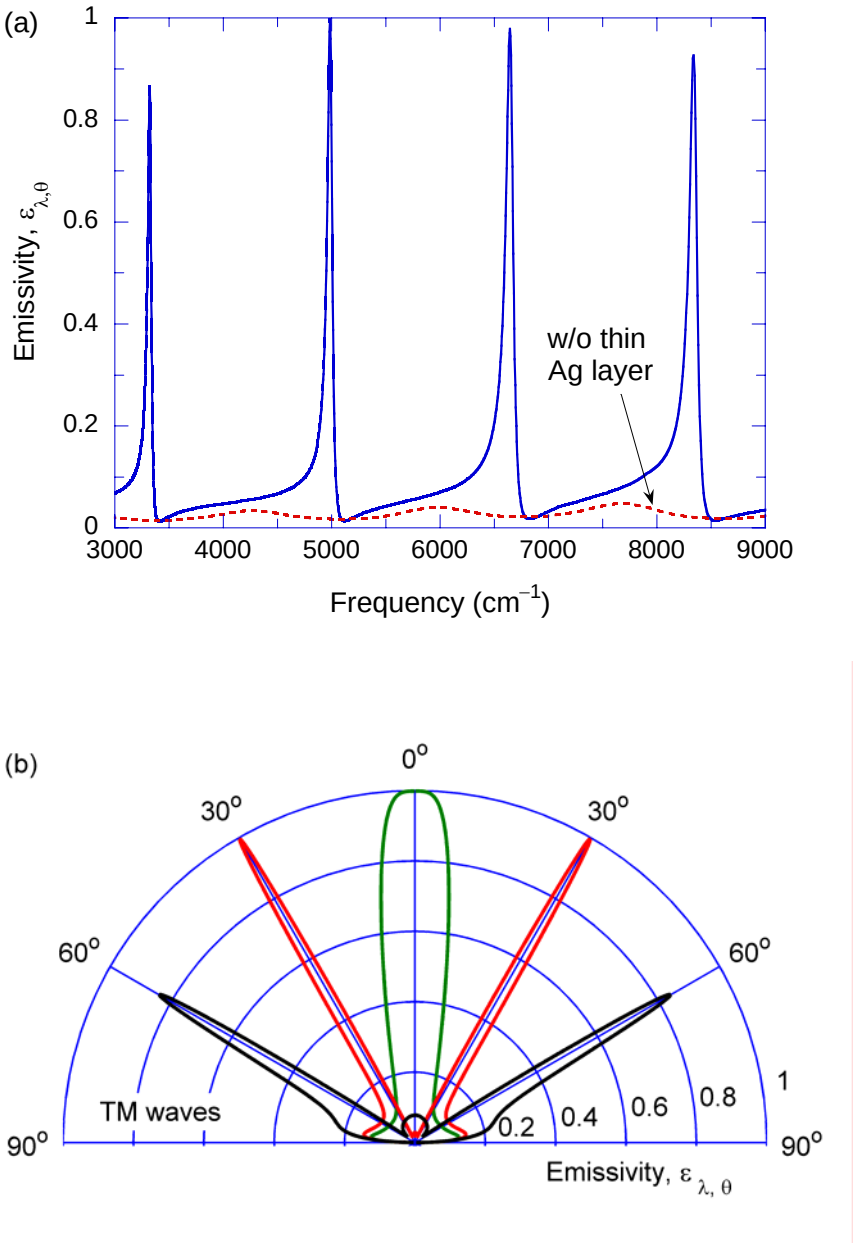

Figure 4.7 The emissivity $\varepsilon_{\lambda,\theta}$ of the Fabry-Pérot cavity: (a) Spectral emissivity at normal incidence (solid line). The thickness of the SiO_2 cavity is 2 μm, and that of thin Ag film is 15 nm. The dotted line represents the case without a front Ag film. (b) Angular distribution of the emissivity at three peak frequencies for TM waves. The emissivity peaks corresponding to emission angles of $\theta = 0°$, 30°, and 60° are centered at $\nu_c = 4984.5$, 5284.0, and 6098.0 cm^{-1}, respectively.

shows some oscillations, but the emissivity values are very low even at resonance frequencies. Therefore, high reflection from both boundaries of the cavity is the crucial factor to enable the large emissivity values. For the Fabry-Pérot resonance cavity, the quality factor is usually defined as $Q = \Delta\nu_{\mathrm{f}} / \Delta\nu$ where $\Delta\nu_{\mathrm{f}}$ is a free spectral range, which is the frequency difference between subsequent peaks, and is also called the *finesse* [68]. The definition of the quality factor is consistent with that of the PC-on-Ag structure by regarding that $\Delta\nu_{\mathrm{f}} = \nu_{\mathrm{c}} - 0$, when only one peak is available like the case of the surface wave excitation. The quality factor of the Fabry-Pérot cavity near 5000 cm^{-1} is estimated as 28.6 at normal incidence. The low value of the quality factor is due to closely spaced emissivity peaks.

In order to demonstrate the spatial coherence of the Fabry-Pérot resonance cavity, the angular distribution of the spectral-directional emissivity is plotted in Fig. 4.7(b) at three peak frequencies around 5000 cm^{-1} for TM waves. The corresponding peak frequencies for emission angles of $\theta = 0°$, $30°$, and $60°$ are $\nu_{\mathrm{c}} = 4984.5$, 5284.0, and 6098.0 cm^{-1}, respectively. Unlike the PC-on-Ag structure, the normal emissivity is very close to unity, and the emissivity value decreases as the emission angle increases. The FWHM $\Delta\theta$ of the angular lobes are estimated as 20.64°, 3.87°, and 6.09° for emission angles of $0°$, $30°$, and $60°$, respectively. These values are slightly smaller than those achieved from the PC-on-Ag structure. Since wave interference effects are independent of the polarization, the narrow angular lobes in the emissivity can also be found for TE waves at corresponding peak frequencies. However, for TE waves the peak frequencies at emission angles of $0°$, $30°$, and $60°$ are different from those for TM waves because the phase shifts ϕ_{21} and ϕ_{23} in Eq. (2.16) are based on reflection coefficients that depend on

the polarization. The angular lobes of TE waves are found at $\nu_c = 5390.0$ and 6211.5 cm^{-1} for $\theta = 30°$ and $60°$, respectively.

It would be interesting to investigate where the absorption occurs in the Fabry-Pérot cavity because the Ag films on both side of the dielectric can absorb the incident energy. It should be noted that the transmittance T in Eq. (2.13) represents the energy penetrating into the Ag reflector on the right in Fig. 4.1(b), and, thus, it will be eventually absorbed. In other words, the transmittance T indicates the absorption by the thick Ag reflector. The fraction of the absorption due to the right Ag reflector is estimated to be one fourth, and thus, 75% of the absorbed energy is confined in the 15-nm-thick Ag film. From Kirchhoff's law, it can be thought that the 15-nm-thick Ag film contributes mostly to the thermal emission from the cavity. The emissivity of a free-standing 15-nm Ag film is less than 0.1 near the frequency of 5000 cm^{-1}. Consequently, the dielectric cavity coated with highly reflective Ag films can significantly enhance thermal emission at the resonance frequencies and the emission is temporally and spatially coherent.

The asymmetric Fabry-Pérot cavity was made in a similar manner as the PC-on-Ag structure. After depositing the 200-nm-thick Ag film on the Si substrate, SiO_2 was deposited using PECVD at 250°C with the thickness of about 2 μm. Afterwards, approximately 15-nm-thick Ag film was sputtered atop the SiO_2. Once all fabrication processes were completed, the coated wafers were diced into 25.4 mm × 25.4 mm specimens for the reflectance measurement.

The measured reflectance of the Fabry-Pérot cavity is plotted in Fig. 4.8 together with the calculated. A commercial Fourier-transform infrared (FTIR) spectrometer measures the reflectance of the specimens at an incidence angle of 10° without

polarization, using a specular reflectance accessory. The details of the spectral reflectance measurements will be discussed in the next chapter. Here, only near-normal reflectance of the Fabry-Pérot resonator is discussed to demonstrate its coherent emission characteristic. It can be clearly seen from Fig. 4.8 that several sharp reflectance dips exist with reflectance value close to 0.1. The free spectral range $\Delta\nu_f$ of the reflectance spectrum mainly depends on the refractive index and the thickness of the resonance cavity. By fitting $\Delta\nu_f$ and resonance frequencies, the thickness of the cavity is determined to be 1.968 μm, and the thickness of front Ag film is found to be 22 nm. Reasonably good agreements are obtained between the measured and calculated reflectance. However, considerable deviations of the reflectance are found in the higher

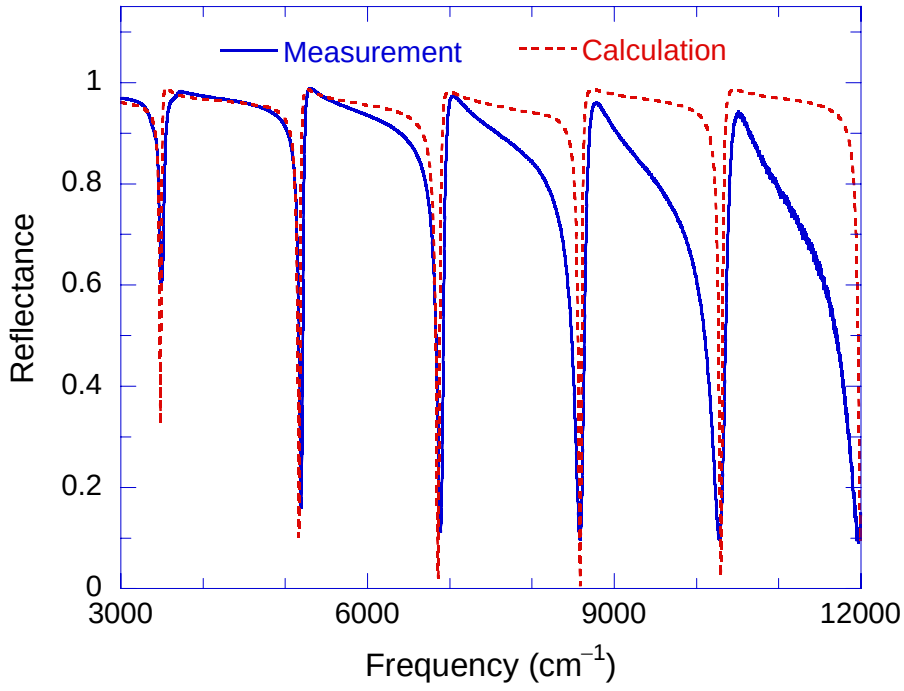

Figure 4.8 Spectral reflectance of the fabricated Fabry-Pérot resonance cavity in the near-IR spectral region at room temperature. The solid and dashed lines represent the measured and predicted reflectance, respectively.

frequency range. Although not plotted in Fig. 4.8, the calculated reflectance by increasing the value of the tabulated refractive index for Ag has much better agreement with the measured spectrum. Hence, one possible explanation of the difference between the measured and predicted reflectance spectra may be additional losses in the deposited Ag film, especially in the higher frequency region. Notice that the optical constants in the deposited Ag film may not be exactly the same as those given in the handbook [94].

CHAPTER 5

EXPERIMENTAL DEMONSTRATION OF COHERENT EMISSION CHARACTERISTICS

This chapter describes a detailed experimental investigation of coherent emission characteristics for the fabricated PC-on-Ag structure. A FTIR spectrometer, together with a specular reflectance accessory and a linear polarizer, is used to measure the reflectance of the fabricated sample at incidence angles of 10°, 30°, and 45°. A laser scatterometer [97] is used to measure the angle-resolved reflectance at the wavelength of 891 nm for different polarizations. The surface-wave excitation can be manifested by a sharp dip in the measured reflectance due to strong absorption at the resonance condition. Since the PC-on-Ag structure is essentially opaque, the spectral-directional emissivity can be obtained from Kirchhoff's law [1]. The temporal and spatial coherence of the emission from the fabricated sample is carefully examined. Furthermore, the surface-wave dispersion relation is calculated based on the Supercell method with modified matrix equations as described in Chapter 2. The resonance conditions obtained from experiments are compared with the surface-wave dispersion relation in the following discussion.

Spectral Reflectance Measurements

An ABB Bomen FTLA2000 series FTIR spectrometer was used to measure the reflectance of the fabricated PC-on-Ag structure. The near-IR source is a quartz-halogen lamp with a tungsten filament, and the detector is a pyroelectric detector, which has an excellent linearity and can respond up to frequencies of 12000 cm^{-1}. The stability of the

near-IR source was examined over three hours, and the output signal was found to be stable within 1% of fluctuation. A sample holder with an aperture of 9 mm diameter limited the beam size on the sample. Since scattering from the multilayer structure is negligible, the reflection is specular. One of the three reflectance accessories was attached to the spectrometer to fix the incidence angles of 10°, 30°, or 45°. At $\theta = 10°$, the reflectance is almost the same for the two polarizations and the frequencies at the reflectance minimum would be different by only 10 cm^{-1} between the two polarizations. Hence, no polarizer was used for 10° incidence, and a wire-grid polarizer was employed for the reflectance measurements at $\theta = 30°$ and 45°. The reflectance spectra were taken with a resolution of 2 cm^{-1}. An Au mirror was used as the reference, and its reflectance was calculated using the optical constants given in Ref. [94]. The spectral reflectance measurement was repeated ten times by interchanging the reference and the specimen, and each measurement was averaged over 64 scans. The background signal was measured without placing a sample, and the signal without sample (open aperture) was less than 0.5% of that with the Au mirror. Considering the repeatability, alignment error, and uncertainty in the reflectance of the Au mirror, the overall uncertainty of the measured reflectance was estimated to be 0.03 with a 95% confidence level.

Figure 5.1 shows the measured and predicted reflectance spectra of the PC-on-Ag structure at $\theta = 10°$, 30°, and 45°. Since the reflectance spectrum is measured with the FTIR spectrometer, the reflectance rather than the emissivity is presented here. Since the difference in reflectance between TM and TE wave is negligibly small at the incidence angle of 10°, the results can be considered as for either polarization. The solid line represents the measured reflectance spectrum, and the dashed line indicates the calculated

spectrum based on the fitted geometric parameters. Since the thicknesses of the dielectrics in the fabricated sample may slightly deviate from the target values after actual deposition processes, a least-squared fitting was performed to match the reflectance dip frequencies for all measurements by taking Λ and d_{ter} as fitting parameters. The thicknesses of Si_3N_4 and SiO_2 were assumed to be the same and the frequency-dependent optical constants based on a linear interpolation of the tabulated data [94] were used in the fitting process as well as in the reflectance calculation hereafter. From the fitting, the geometric parameters were determined to be $d_{\text{H}} = d_{\text{L}} = 153$ nm and $d_{\text{ter}} = 100$ nm.

A sharp reflectance dip can be seen at 9885 cm^{-1} from the measured spectrum at near-normal incidence; see Fig. 5.1(a). When surface waves are excited at the PC-Ag interface, the incident photon energy is coupled to surface waves and eventually absorbed by the Ag layer. The small reflectance dips found in the pass band of the PC are caused by wave interference effects in the multilayer structure and does not contribute much to the absorption. The calculated reflectance captures the essential features of the measured spectrum. Compared with the prediction, the measured reflectance valley is not as deep and sharp. This may be caused by the effect of partial coherence, resulting from the non-uniformity and surface roughness of the fabricated thin films in the multilayer structure [98,99]. The half cone angle of the incidence beam in the FTIR spectrometer is about 6°, and beam divergence may further reduce the coherence. Imperfection in microstructure of the dielectric and Ag films can also contribute to the dip broadening in the measured spectrum. The relatively large difference between measured and predicted reflectance in the higher frequency region is attributed to the additional losses in the deposited Ag film.

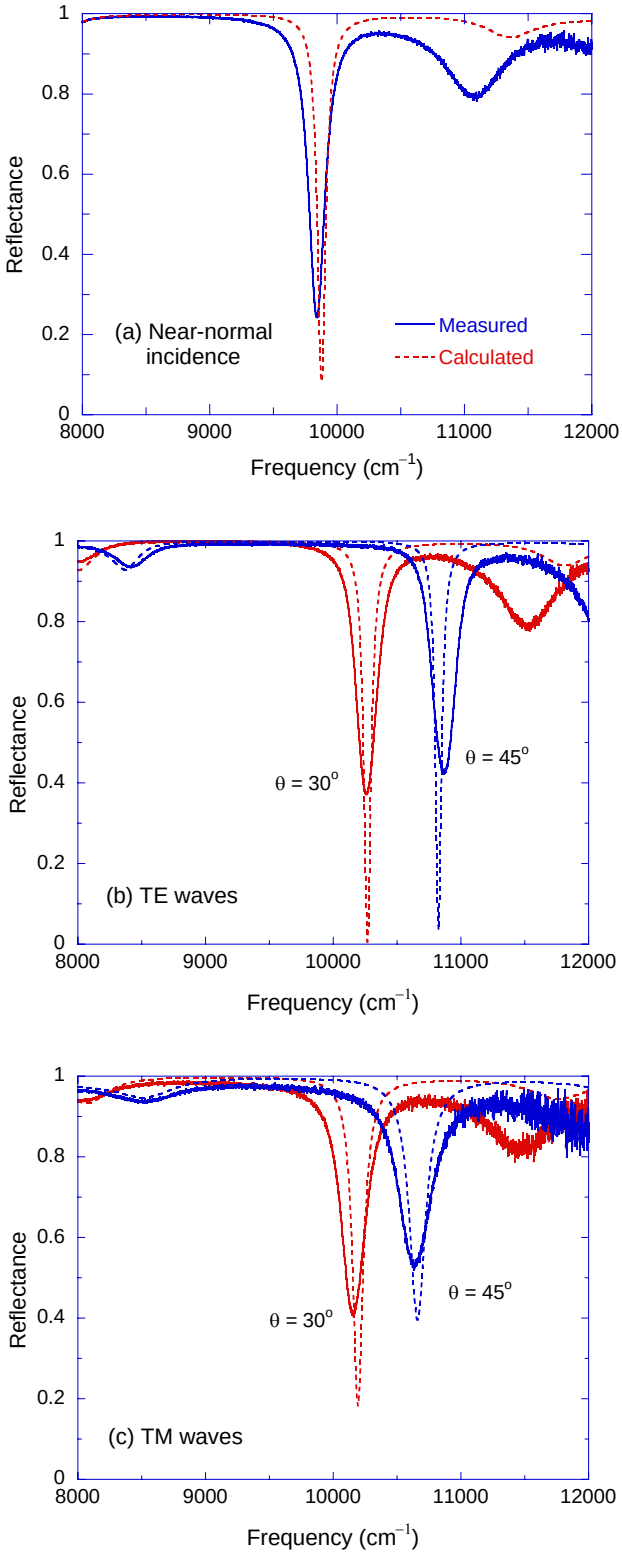

Figure 5.1 Spectral reflectance of the fabricated PC-on-Ag structure in the near-IR: (a) Near-normal incidence; (b) TE waves; (c) TM waves. The calculated reflectance spectra based on the fitted parameters are denoted by dashed lines.

The reflectance spectra for TE waves at incidence angles of 30° and 45° are shown in Fig. 5.1(b). The reflectance dip is found to shift towards higher frequencies as the incidence angle increases. The measured reflectance minimum is 0.37 for $\theta = 30°$ and 0.42 for $\theta = 45°$. The calculation shows sharper and deeper valleys due to beam divergence in the measurement setup. Beam divergence is the dominant reason at large θ values, because both the reflectance and the resonance condition are very sensitive to the incidence angle. The reflectance spectra for TM waves in Fig. 5.1(c) show similar trend as those for TE waves, except that the valleys are slightly shallower and wider. Considering the uncertainty in the spectral reflectance measurement and possible variations in the film thicknesses, the agreement between the calculation and measurement is satisfactory. An attempt was made to take d_{H} and d_{L} as separate fitting parameters but did not yield noticeable improvement.

Since the Ag layer is opaque, the emissivity of the PC-on-Ag structure is simply one minus the reflectance according to Kirchhoff's law. A sharp dip in the reflectance spectrum can be regarded as a peak in the emissivity and, therefore, the concept of coherent thermal emission [24,42,80,81,100] can be realized. Furthermore, the frequency of the emission peak can be tuned towards longer wavelengths (e.g., mid-infrared region) by increasing the period of the PC. In the application as a coherent emission source, the PC-on-Ag structure needs to be heated to elevated temperatures in order to utilize the emission peak in the near infrared. The temperature-dependent optical constants are necessary to fully describe the emission characteristics. Celanovic et al. [16] showed that the temperature-dependent optical constants have little effects on the frequency and value of emissivity peak up to 900 K, although its bandwidth slightly increases. In addition,

thermal expansion and thermal stress of thin films are practical issues that need to be evaluated for high-temperature applications. For demonstration of the concept of coherent emission for both polarizations by exciting surface waves at the truncated PC and metallic interface, the effects of temperature and thermal stress are not considered in the present work. The quality factor $Q = \nu_c / \Delta\nu$ is usually employed as a measure of temporal coherence. Here, ν_c is the center frequency of the emissivity peak (or reflectance dip) and $\Delta\nu$ is the full-width-at-half-maximum (or minimum). From Fig. 5.1, the $\Delta\nu$ is estimated to be 158 cm^{-1} and the calculated Q value is 62.6 for $\theta = 10°$. Furthermore, $\Delta\nu$ for TE waves are 196 cm^{-1} at $\theta = 30°$ and 215 cm^{-1} at $\theta = 45°$, and the corresponding Q values are 52.3 and 50.6, respectively. For TM waves, the $\Delta\nu$ and Q are 232 cm^{-1} and 43.8 at $\theta = 30°$ and 307 cm^{-1} and 34.6 at $\theta = 45°$, respectively. Clearly, the quality factor decreases as the incidence angle increases for both polarizations and are slightly less than half of the calculated values [100]. Based on the quality factor, better temporal coherence is achieved for TE waves because the fabricated sample was designed for an optimum performance of TE waves. By changing the number of unit cells as well as the surface termination d_{ter}, the PC-on-Ag structure can also be optimized for TM waves.

Angle-Resolved Reflectance Measurements

The bidirectional reflectance of the fabricated sample was measured with a custom-designed three-axis automated scatterometer [97]. The laser scatterometer is equipped with a goniometric table, a light source, detectors, and a data acquisition system. Very high angular resolution, accuracy and repeatability can be achieved by the

goniometric table with computer-controlled rotary motors. The light source is a fiber-coupled laser diode, whose wavelength was determined to be 891 (± 1) nm using a mini spectroscope (OCLI MicroPac CS600). A twelve hour drift test shows that the root-mean-square fluctuation of the laser output power is 0.22%. The effect of power fluctuation is further reduced by monitoring the laser power with another detector using a beamsplitter. A lock-in amplifier is connected to the diode laser controller to electronically modulate the output power without a chopper. The lock-in amplifier receives the signal from the silicon detector after a preamplifier. A linear polarizer is placed before the laser beam reaches the sample. Since the scattered light from the sample is negligibly small, the measurements were conducted in the specular direction only, with an angular resolution of 0.2°. The effect of azimuthal angle was tested by rotating the sample, and the resulting reflectance change was negligible. Hence, the sample can be considered as isotropic in the azimuthal direction. The uncertainty of the angle-resolved reflectance measurement was estimated to be less than 1% with a confidence level of 95% by comparison with measurements of plain Si wafers.

Figure 5.2 plots the measured reflectance (solid line) as a function of the incidence angle, along with the calculated reflectance (dashed line) for both polarizations. In the calculation, the geometric parameters of the PC-on-Ag structure were taken from the same fitted values as mentioned earlier. For the TE wave, the reflectance dip is at $\theta = 54°$ with the reflectance value less than 0.05, as shown in Fig. 5.2(a). The measurement and calculation agree very well. Since the laser beam is highly collimated, the measured reflectance exhibits a very sharp dip with a minimum even lower than that predicted, although the calculated width of the valley is somewhat narrower. The

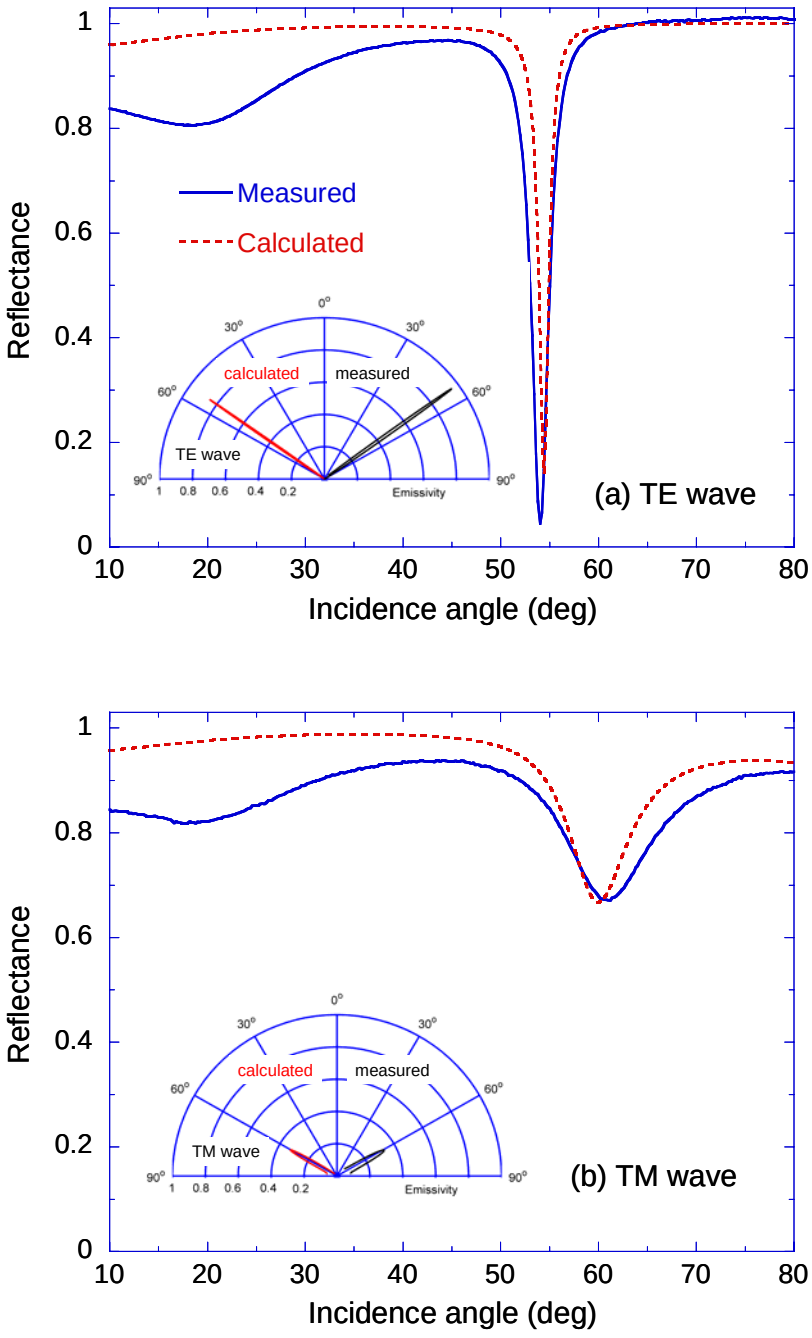

Figure 5.2 Reflectance as a function of the incidence angles at 891 nm for (a) TE waves and (b) TM waves. Solid lines represent measured results, and dashed lines indicate calculated values. The inset shows the directional emissivity calculated from Kirchhoff's law in the vicinity of the emission peak. In the insets, the right half represents the measurement, and the left half represents the prediction.

absorption of Ag film depends on the deposition conditions. The loss in the fabricated film may be larger than those used to obtain the dielectric function of Ag in Ref. [94]. The additional loss may result in a line broadening of the reflectance dip as well as a reduction of the reflectance at small incidence angles. For the same reason, the measured reflectance in Fig. 5.1 is somewhat lower than the predicted at shorter wavelengths. For TM waves, Fig. 5.2(b) shows that a shallow valley exists at $\theta = 61.2°$ with a minimum reflectance value of 0.77. There is approximately 1° difference in the resonance condition between the measured and the calculated reflectance. If the wavelength of the laser is changed by 2 nm, which is equivalent to 25 cm^{-1} difference in the frequency, then the reflectance dip position will match each other. Notice that the 25 cm^{-1} difference in the frequency is less than the uncertainty between reflectance dip frequencies of the measured and fitted spectra in Fig. 5.1.

The directional emissivity, obtained from the measured reflectance using Kirchhoff's law, is plotted in the vicinity of the peak as insets in Fig. 5.2. The right half represents the measurement and the left half represents the prediction. The angular-dependent emissivity exhibits strong directional selectivity for both polarizations. The coherence length given by $L_{coh} = \lambda/(\pi\Delta\theta\cos\theta)$ [23], where $\Delta\theta$ is the full-width-at-half-maximum of the emissivity peak, is a measure of the spatial coherence. Alternatively, the spatial coherence length of thermal source can be estimated by plotting the cross-spectral density of the *z*-component of the electric field [95]. The estimated $\Delta\theta$ from the measurements is 2.2° and 12.3° for the TE and TM waves, respectively, and the corresponding coherence lengths are 14.1λ and 3.1λ. The coherence length for TE waves is much longer than that for TM waves, suggesting that the fabricated structure can result

in better temporal coherence for TE waves than TM waves. The experimentally obtained coherence length for TE waves in the present study is slightly smaller than those from binary gratings [23,24].

Comparison of Measurements with Surface-Wave Dispersion Curves

Figures 5.3(a) and 5.3(b) show the dispersion relation of surface waves at the PC-Ag interface for the TE and TM waves, respectively. The calculation is conducted based on the modified supercell method. The dashed curves are the predicted dispersion relations that lie in the stop band of the PC, whereas the diamonds and triangles represent the reflectance dip locations from the reflectance measurements. In the supercell calculation, twenty complete unit cells were used to construct the supercell, and the thickness of Ag layers was set to be 15Λ, such that the coupling of surface waves could be neglected. The thicknesses of each dielectric were obtained from the fitted parameters of the reflectance measurements. The dielectric functions of Si_3N_4 and SiO_2 layers were assumed as $\varepsilon_{\mathrm{H}} = 2.0^2$ and $\varepsilon_{\mathrm{L}} = 1.45^2$, respectively. These values were obtained from tabulated data in Ref. [94] near 1 μm wavelength. For Ag, only the real part of the dielectric function was considered, as commonly done for calculating the dispersion relation of surface polaritons [101]. Its value was taken as constant of $\varepsilon_{\mathrm{Ag}} = -41.3$. The variation of dielectric functions was neglected for simplicity in calculations. If frequency-dependent dielectric functions were employed, the resonance frequency of surface waves would shift by less than 0.5% in the near-infrared. A total of 801 Fourier coefficients were used to construct the Bloch wave given in Eq. (2.27) to achieve a convergence within 0.1%. Due to the presence of a metallic layer in the supercell calculation, more

Fourier terms are necessary as compared to the case of surface waves at the PC-dielectric interface. It should be noted that the failure of applying the inverse rule in Eq. (2.31) may not cause a serious problem in the case of surface waves at the PC-dielectric interface. If a metallic layer is involved in the supercell structure, however, the modified equations must be used to obtain the surface-wave dispersion relations for the TM wave. The band structure of the 1D PC obtained using Supercell method agrees very well with the solution obtained from the transfer matrix formulation [81].

In Fig. 5.3, the shaded regions correspond to the pass band, and the unshaded regions represent the stop band. The light line in air is denoted by a dash-dot line. Obviously, the dispersion curves (dashed lines) of the surface wave are located in the stop band of the PC, where an effective evanescent wave exists. For the TE wave shown in Fig. 5.3(a), one branch exists in the dispersion relation of the PC-on-Ag structure, which involves an effective evanescent wave in the PC and a propagating wave in air. For TM waves, however, there exist two dispersion curves as shown in Fig. 5.3(b). The lower branch is the case when actual evanescent waves exist in all dielectric layers as well as in the Ag layer. Therefore, it is located in the right side of the light line in the higher index material (i.e., Si_3N_4). The lower branch corresponds to the surface plasmon polaritons that can be observed in the conventional ATR configuration for TM waves only. On the other hand, for the upper branch the surface wave can be excited by propagating waves in air, similar to the TE wave.

The resonance conditions obtained from the measured reflectance are now compared with the surface-wave dispersion relation calculated using the modified supercell method. For the purpose of comparison, the frequencies and incidence angles

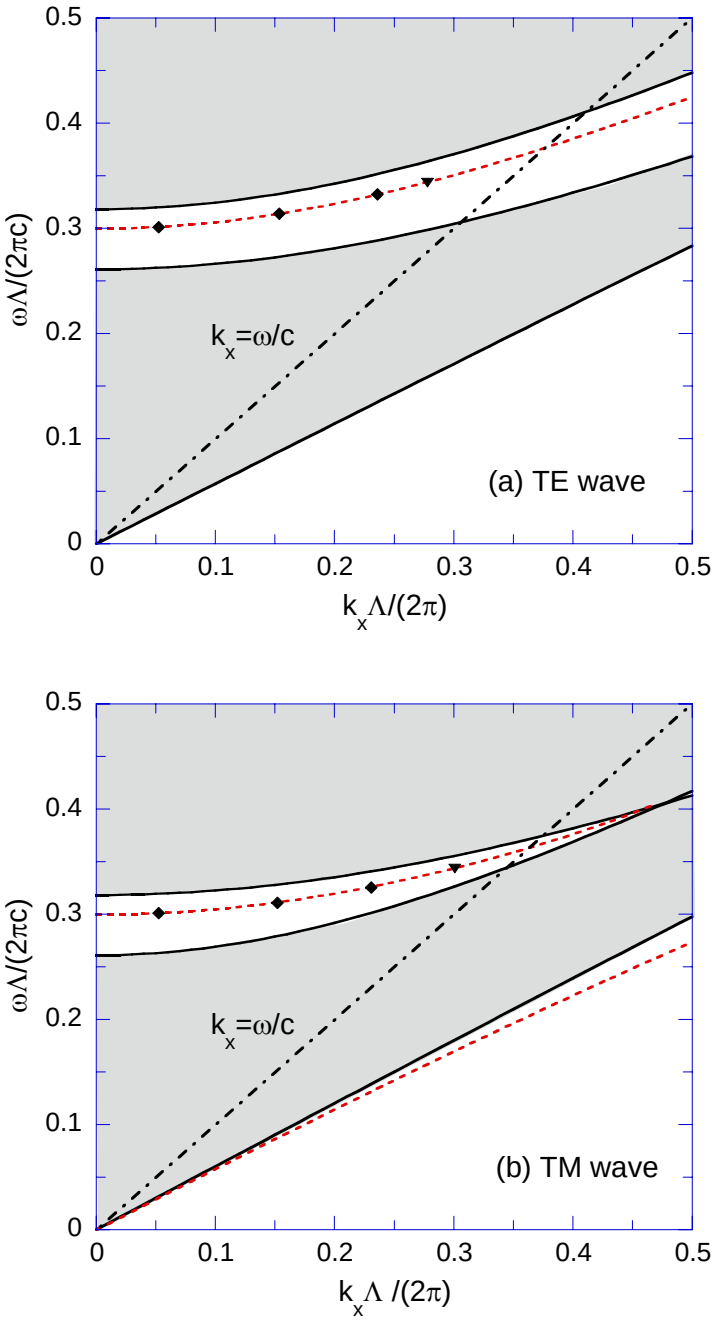

Figure 5.3 Surface-wave dispersion curves shown as dashed lines for (a) TE waves and (b) TM waves. The geometric parameters of the PC-on-Ag structure are taken from the fitted values based on the measured reflectance. The shaded regions represent pass bands and the unshaded regions correspond to stop bands of the PC that is infinitely extended. The resonance conditions obtained from the spectrometer measurements and from the scatterometer measurements are denoted by the diamond and triangular symbols, respectively.

corresponding to the measured reflectance dips are converted into the $\omega - k_x$ plane as shown in Figs. 5.3(a) and 5.3(b). The diamonds represent the conditions where reflectance dips are found in the spectrometer measurements, and the triangles indicate the resonance conditions in the scatterometer measurements. It can be seen that the experimentally obtained resonance conditions are located close to the calculated surface-wave dispersion curves. The comparison confirms that surface waves are excited at the PC-Ag interface by a propagating wave in air. In general, the resonance condition is sensitive to the surface termination of the PC. For the considered PC-on-Ag structure, the dispersion curve shifts to a lower frequency region for both polarizations if d_{ter} increases (not shown here).

To further investigate the enhancement of the field magnitude accompanied with the surface wave excitation, the magnitude of the evanescent wave at the PC-Ag interface is plotted in Fig. 5.4. The tangential component of the electric field E_y is plotted in Fig. 5.4(a) for TE waves, and that of the magnetic field H_y is plotted in Fig. 5.4(b) for TM waves. The calculation was done for propagating waves in air (i.e., inside the light cone). Hence, the region in the right side of the light line is blackened in Fig. 5.4. The geometric parameters of the PC-on-Ag structure are the same as in Figs. 5.1 and 5.2. Furthermore, the frequency-dependent dielectric functions have been taken into consideration. The band edges of the PC are shown as the white dashed lines, within which lies the stop band, as predicted by the band structure calculation. The field magnitude oscillates in the pass bands of the PC due to wave interference effects in the multilayer structure. In the stop band, however, the field magnitude is greatly enhanced in

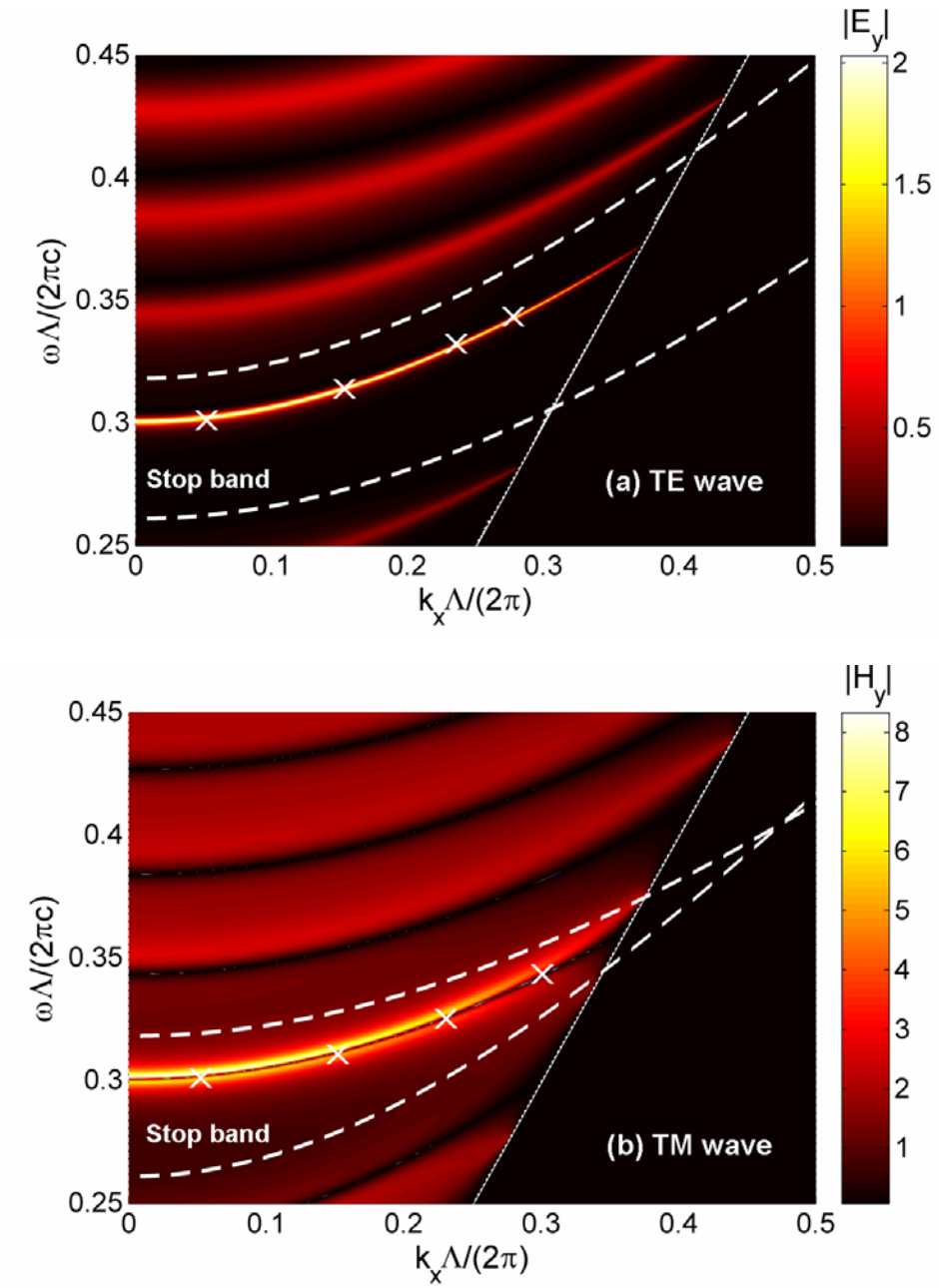

Figure 5.4 Magnitude of the tangential field component at the interface between 1D PC and Ag film: (a) $|E_y|$ for TE waves; (b) $|H_y|$ for TM waves. The calculation is only conducted inside the light cone of air (solid line). The stop band of the 1D PC is located between the band edges, which are represented by dashed lines. Locations of the measured reflectance minima are marked by the × symbol.

a narrow band in the $\omega - k_x$ plane, which is notable by the bright color. These lines correspond well with the surface wave dispersion curves in Fig. 5.3. In Fig. 5.4, × marks denote the resonance conditions from the reflectance measurements. Like the dispersion curves, the resonance conditions agree well with the conditions when the magnitude of evanescent waves is greatly enhanced at the PC-Ag interface, confirming the existence of surface waves. The measured reflectance provides the first experimental demonstration of coherence spectral characteristics in the PC-on-Ag structure, due to the surface-wave excitation without using a prism. It is interesting to note that for TE waves, the magnitude of evanescent waves is enhanced for approximately twenty times when surface waves are excited, as compared to the case without surface waves. For TM waves, the field is enhanced for about five times with surface wave excitations. Hence, the resulting peak emissivity values are higher for TE waves from the fabricated PC-on-Ag structure.

CHAPTER 6

ENERGY PROPAGATION DIRECTION IN PHOTON TUNNELING AND NEAR-FIELD THERMAL RADIATION

In this chapter, we employ the energy streamline (ESL) method based on the Poynting vector of coupled plane waves to study the lateral beam shift associated with photon tunneling. The direction of the net energy flux of electromagnetic waves can be well characterized by the ESL, which is tangential to the time-averaged Poynting vectors. In the second part of this chapter, we extend the ESL method to investigate the energy pathway in near-field thermal radiation between two semi-infinite surfaces separated by a vacuum gap. With the use of fluctuation-dissipation theorem [102] and dyadic Green's function [103], the thermally emitted electromagnetic waves in the vacuum gap are completely determined. Then, we show that the Poynting vector is decoupled for each parallel wavevector component due to the random nature of thermal emission. By employing the ESL method, the energy pathways in the near field are separately obtained for different parallel wavevector components. Furthermore, the effect of surface polaritons on the lateral shift of energy path is investigated. While fluctuational electrodynamics has been used to calculate the energy flux in nanoscale thermal radiation, it has not been employed to describe the energy propagation direction.

Photon Tunneling

To further understand the photon tunneling phenomenon, let us consider the configuration of the double negative (DNG) material sandwiched by prism for TM waves, as shown in Figs. 6.1(a) and 6.1(b), at different incidence angles. The energy transports

from the left to the right, as denoted by arrows for $\theta = 20°$ as an example. The trajectory of the Poynting vector in the three regions forms a zigzag path, especially when $d << \lambda$. The *z* and *x* axes are normalized to the slab thickness *d*, which is $\lambda/20$ in Fig. 6.1(a) and $\lambda/5$ in Fig. 6.1(b). All energy streamlines are for positive k_x values and pass through the origin. With the dielectric prism ($\varepsilon = 2.25$), the critical angle is $\theta_{\text{cr}} = 41.81°$. Causality requires that $\langle S_z \rangle$ be positive; furthermore, when loss is neglected, $\langle S_z \rangle$ is independent of *z*. Note that $\langle S_x \rangle = \frac{k_x}{2\omega\varepsilon_0} \text{Re}(1/\varepsilon) |H_y|^2$ is opposite to k_x when $\text{Re}(\varepsilon) < 0$, as in the DNG layer, i.e., medium 2. It is surprising to note that at $\theta_1 = \theta_{\text{cr}}$ (i.e., when the phase refraction angle $\theta_2 = 90°$), the energy propagation angle θ_{E} in medium 2, is much less than 90°. Furthermore, the dash-dotted line in the slab separates the propagating-wave streamlines (inside the cone) from the evanescent-wave streamlines (outside the cone). The observation that the energy paths of propagating waves and evanescent waves are separated by a cone provides a new explanation of the photon tunneling phenomenon based on wave optics. When $d = \lambda/5$, the streamlines become wavy as seen in Fig. 6.1(b). The energy transmittance through the DNG slab, calculated by $T = |A_3/A_1|^2$, is labeled for each streamline except $\theta_1 = \theta_{\text{cr}}$, where Airy's formulae are used to obtain *T* by taking the limit $k_z \to 0$.

By changing μ_2 from −1 to 1 and plotting the energy streamline in Figs. 6.1(c) and 6.1(d), one can investigate photon tunneling through a single negative (SNG) material slab. In this case, only evanescent waves exist in the slab because k_z is purely imaginary even at normal incidence. Energy is carried through medium 2 by coupled

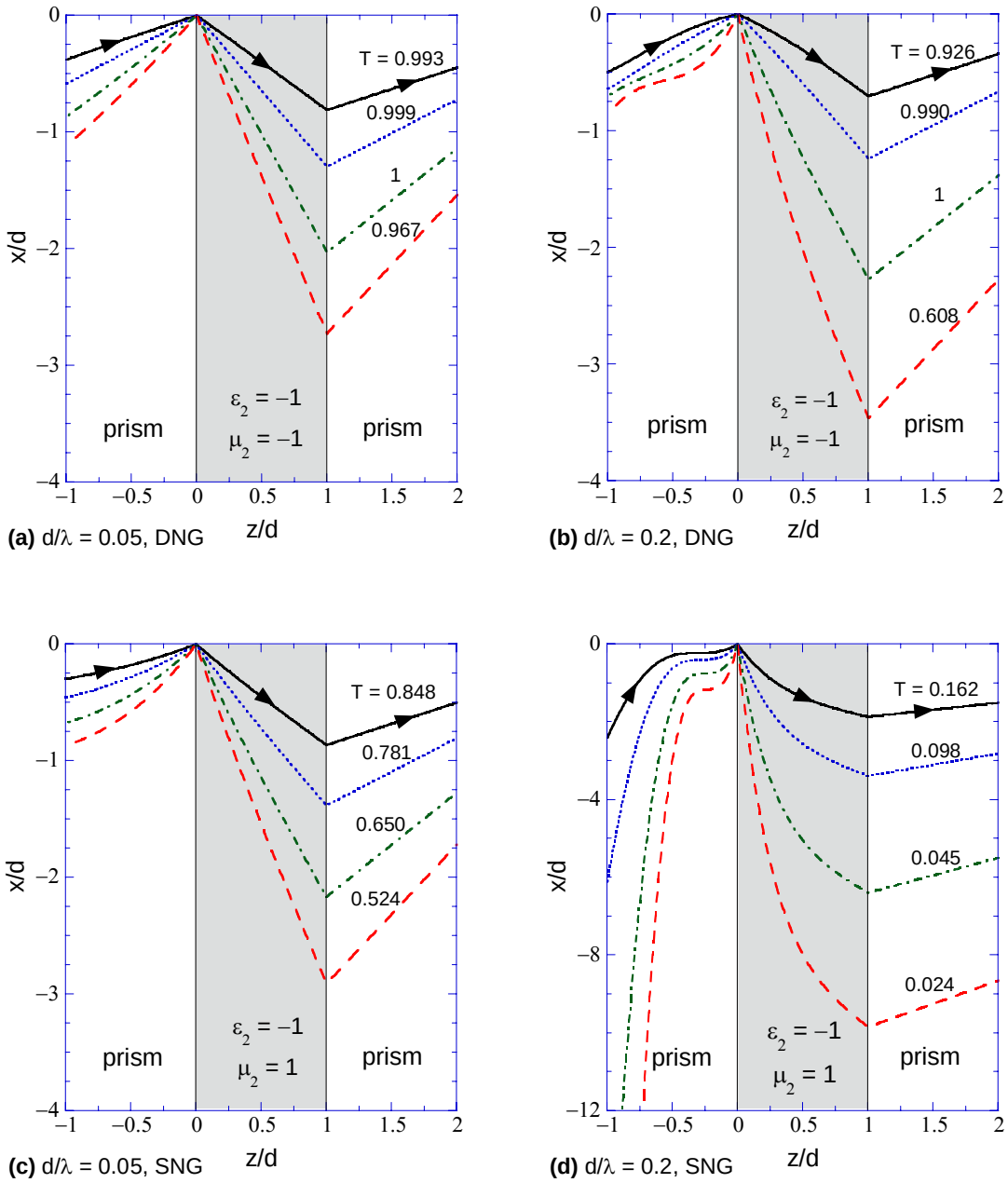

Figure 6.1 Energy streamlines for prism-DNG-prism and prism-SNG-prism configurations at various incidence angles: $\theta_1 = 20°$ (solid), 30° (dotted), 41.81° (dash-dot), and 50° (dashed) for TM waves. The prism has $\varepsilon = 2.25$ and $\mu = 1$, so $\theta_1 = 41.81°$ corresponds to the critical angle for DNG in (a) and (b). Only evanescent waves exist in medium 2 for SNG in (c) and (d). The energy transmittance (T) from medium 1 to 3 is shown for each incidence angle. A different scale is used for the x axis in (d).

evanescent waves, whose path can be completely described by a streamline. The transmittance with a SNG slab is much smaller than that with a DNG slab for the same ε, and the lateral beam shift in the x direction becomes very large in Fig. 6.1(d). Yet, Figs. 6.1(a) and 6.1(c) look alike. Alu and Engheta [65] pointed out that, when $d << \lambda$, propagating waves and evanescent waves are similar because both the sinusoidal function and the hyperbolic function are the same under the small-argument approximation. After some tedious derivations, we arrive at the following approximation for energy propagation angle θ_{E}'s when $d/\lambda \to 0$:

$$\theta_{\mathrm{E}1} = \theta_1 \quad \text{and} \quad \tan\theta_{\mathrm{E}2} = (\varepsilon_1/\varepsilon_2)\tan\theta_{\mathrm{E}1} \tag{6.1}$$

assuming that only propagating waves exist in medium 1 and both ε_1 and ε_2 are real. Note that μ_2 does not affect the TM wave results in the electrostatic limit, as noted by Pendry [104]. However, the effect of μ_2 becomes significant when $d/\lambda > 0.1$, as demonstrated in Figs. 6.1(b) and 6.1(d). Although Poynting vector traces have been used in inhomogeneous media and around small spheres [88,105], the application to planar layered structures here reveals some quite striking features of the energy transfer by coupled evanescent waves.

Both positive and negative phase-time shifts were noticed by Li [106] for an optically dense dielectric slab in air without evanescent waves. It is worthwhile to take a look at the energy streamlines for the vacuum-dielectric-vacuum configuration. For propagating waves, because the second term in Eq. (2.35) depends on x, the streamline (solid curve) exhibits wavelike features for $d = \lambda$, as can be seen from Fig. 6.2(a), where the solid curve is the streamline and the dashed lines are the traces of the wavevector.

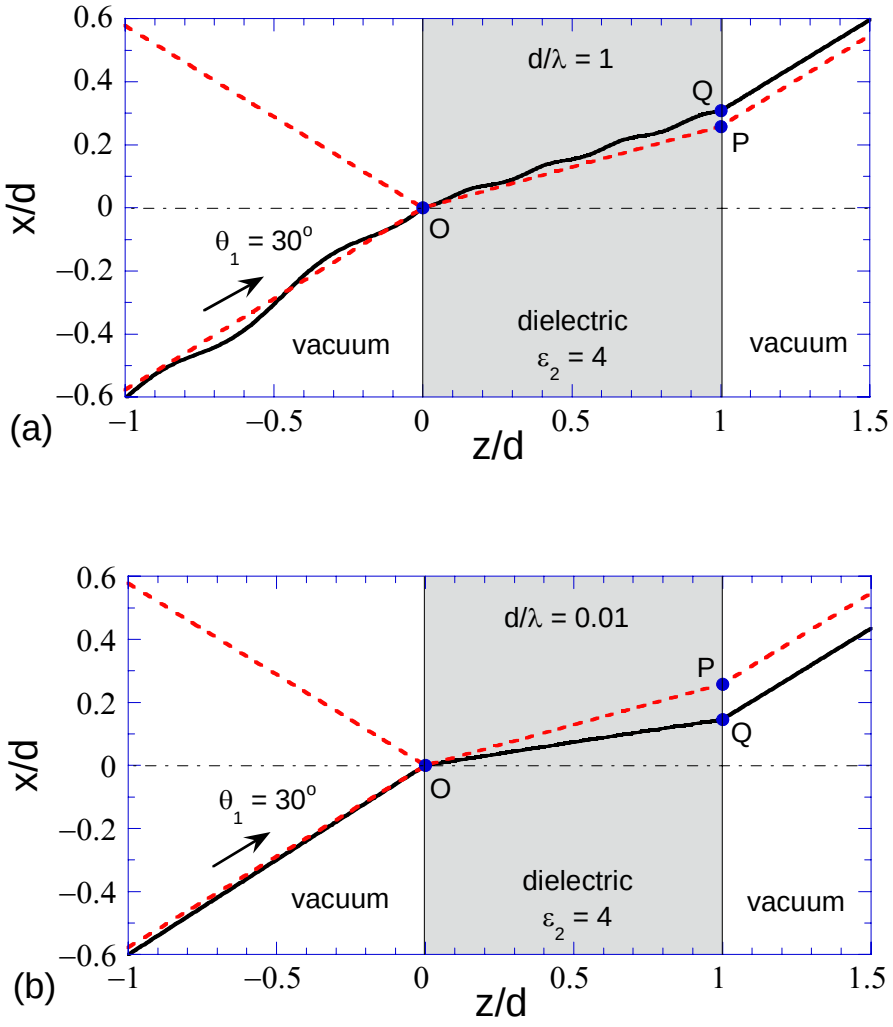

Figure 6.2 The energy streamline for vacuum-dielectric-vacuum configuration at $\theta_1 = 30°$ when (a) $d / \lambda = 1$ and (b) $d / \lambda = 0.01$.

The lateral shift of the energy line is determined by point Q rather than P. When d/λ is reduced to 0.01 as shown in Fig. 6.2(b), the streamline is almost a straight line in each medium. However, Q becomes closer to the z axis than P, in contrary to Fig. 6.2(a). When $d << \lambda$, Snell's law determines the refraction angle θ_2 but Eq. (6.1) determines the energy propagation angle θ_{E2}. The shift of Q with respect to P depends on the incidence angle, which can be positive or negative. Although lateral shifts for photon tunneling or transmission through a dielectric film have been extensively studied using beams of finite width, such as a Gaussian beam, or the derivative of the phase shift [60-64,106], the present study uses plane waves of infinite extension to reveal a beam shift due to interference of propagating waves or coupled evanescent waves.

Energy Pathways in Nanoscale Thermal Radiation

The ESL method discussed above assumes that a plane wave is incident at a fixed parallel wavevector component. This assumption needs to be validated for near-field radiative transfer in which the emission of electromagnetic waves can be understood by the thermally excited random movement of charged particles inside the medium [11]. In other words, a full consideration of plane waves for all possible parallel wavevector components may be necessary to determine the Poynting vector in the near field, as previously done for a binary grating [107] and a superlens [108].

Let us consider nanoscale thermal radiation between two semi-infinite media separated by a vacuum gap, as depicted in Fig. 6.3. The emitter and absorber are set to be SiC that can support surface phonon polaritons in its phonon absorption band approximately between 10.3 μm and 12.6 μm wavelengths, where the real part of the dielectric function becomes negative. The wavelength-dependent dielectric function of

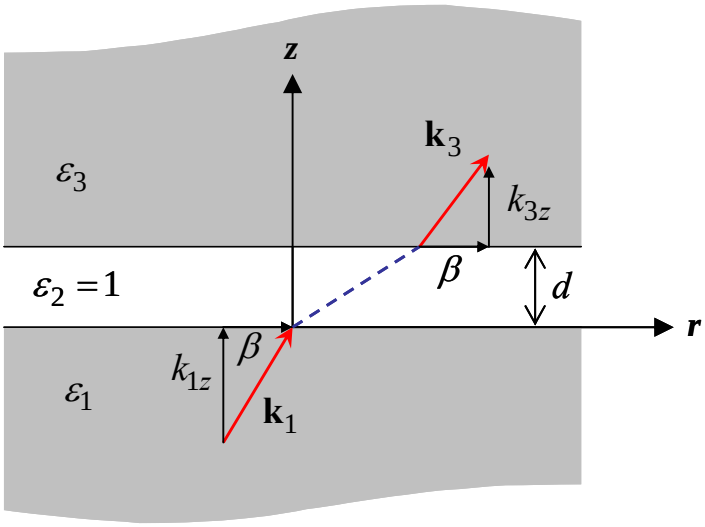

Figure 6.3 Schematic of near-field thermal radiation between two SiC slabs whose dielectric functions are the same: $\varepsilon_1 = \varepsilon_3$. A vacuum gap ($\varepsilon_2 = 1$) of distance d separates the two semi-infinite media. Here, $\mathbf{k}_1$ and $\mathbf{k}_3$ are the wavevectors in media 1 and 3, respectively, and k_{1z} and k_{3z} are the corresponding normal component of the wavevector. The parallel wavevector component β is the same in all three media, and δ denotes the lateral shift for given λ (wavelength in vacuum) and β.

SiC is calculated from the functional expression given in Ref. [90]. Due to the axial symmetry of planar surfaces, cylindrical coordinate can be used, so that the space variable is expressed as $\mathbf{x} = \mathbf{r} + \mathbf{z} = r\hat{\mathbf{r}} + z\hat{\mathbf{z}}$, where $\hat{\mathbf{r}}$ and $\hat{\mathbf{z}}$ are unit direction vectors. The random movement of charge particles causes fluctuating electric currents that will generate electromagnetic waves outside the emitting medium. With the assistance of the electric dyadic Green's function $\overline{\overline{\mathbf{G}}}_{\mathrm{e}}$, the induced electric field $\mathbf{E}$ in the vacuum gap due to the fluctuating current density $\mathbf{j}$ is given by [103]

$$\mathbf{E}(\mathbf{x},\omega) = i\omega\mu_0 \int_{V'} d^3\mathbf{x}' \overline{\overline{\mathbf{G}}}_{\mathrm{e}}(\mathbf{x},\mathbf{x}',\omega)\mathbf{j}(\mathbf{x}',\omega) \tag{6.2}$$

where μ_0 the vacuum permittivity and V' is the volume of emitter (i.e., medium 1), and

$$\overline{\overline{\mathbf{G}}}_{\mathrm{e}} = \frac{i}{8\pi^2}\int_0^{\infty} \frac{\beta d\beta}{k_{1z}} \overline{\overline{\mathbf{e}}}(z,\beta,\omega) e^{-ik_{1z}z'} e^{i\beta\hat{\mathbf{r}}\cdot(\mathbf{r}-\mathbf{r}')} \tag{6.3}$$

Here, $\overline{\overline{\mathbf{e}}} = (\hat{\mathbf{s}} t_{\mathrm{s}}^{+} \hat{\mathbf{s}} + \hat{\mathbf{p}}_2^{+} t_{\mathrm{p}}^{+} \hat{\mathbf{p}}_1^{+}) e^{ik_{2z}z} + (\hat{\mathbf{s}} t_{\mathrm{s}}^{-} \hat{\mathbf{s}} + \hat{\mathbf{p}}_2^{-} t_{\mathrm{p}}^{-} \hat{\mathbf{p}}_1^{+}) e^{-ik_{2z}z}$ where β is the wavevector component in the radial direction (i.e., $\beta^2 = k_x^2 + k_y^2$). The unit vectors for polarization states are defined by $\hat{\mathbf{s}} = \hat{\mathbf{r}} \times \hat{\mathbf{z}}$ and $\hat{\mathbf{p}}_j^{\pm} = (\beta \hat{\mathbf{z}} \mp k_{jz} \hat{\mathbf{r}}) / k_j$ with $k_j = (\omega / c) \varepsilon_j$. Notice that superscripts + and – represent the forward and backward waves, respectively, in the vacuum gap. For each polarization, t_{s}^{+} (or t_{p}^{+}) represents the amplitude of forward waves in the vacuum gap, normalized to the amplitude of the induced electric field at the vacuum-emitter interface, and t_{s}^{-} (or t_{p}^{-}) indicates that of backward waves. By considering multiple reflections in the gap, one can easily obtain

$$t_{\mathrm{s}}^{+} \text{ (or } t_{\mathrm{p}}^{+}) = \frac{\overline{t}_{12}}{1 - \overline{r}_{23} \overline{r}_{21} e^{i2k_{2z}d}} \tag{6.4}$$

$$t_{\mathrm{s}}^{-} \text{ (or } t_{\mathrm{p}}^{-}) = \frac{\overline{t}_{12} \overline{r}_{23} e^{i2k_{2z}d}}{1 - \overline{r}_{23} \overline{r}_{21} e^{i2k_{2z}d}} \tag{6.5}$$

where Fresnel coefficients $\overline{t}_{12}$, $\overline{r}_{21}$, and $\overline{r}_{23}$ are calculated for the corresponding polarization. From Maxwell's equation, the magnetic field can be expressed in a similar way using the magnetic dyadic Green's function $\overline{\overline{\mathbf{G}}}_{\mathrm{m}}$:

$$\mathbf{H}(\mathbf{x}, \omega) = \frac{1}{i\omega\mu_0} \nabla \times \mathbf{E}(\mathbf{x}, \omega) = \int_{V'} d^3\mathbf{x}' \overline{\overline{\mathbf{G}}}_{\mathrm{m}}(\mathbf{x}, \mathbf{x}', \omega) \mathbf{j}(\mathbf{x}', \omega) \tag{6.6}$$

where

$$\overline{\overline{\mathbf{G}}}_{\mathrm{m}} = -\frac{1}{8\pi^2} \int_0^{\infty} \frac{\beta d\beta}{k_{1z}} \overline{\overline{\mathbf{h}}}(z, \beta, \omega) e^{-ik_{1z}z'} e^{i\beta \hat{\mathbf{r}} \bullet (\mathbf{r} - \mathbf{r}')} \tag{6.7}$$

with $\overline{\overline{\mathbf{h}}} = \left((-\beta \hat{\mathbf{z}} + k_{2z} \hat{\mathbf{r}}) t_{\mathrm{s}}^{+} \hat{\mathbf{s}} + k_2 \hat{\mathbf{s}} t_{\mathrm{p}}^{+} \hat{\mathbf{p}}_1^{+} \right) e^{ik_{2z}z} + \left((-\beta \hat{\mathbf{z}} - k_{2z} \hat{\mathbf{r}}) t_{\mathrm{s}}^{-} \hat{\mathbf{s}} + k_2 \hat{\mathbf{s}} t_{\mathrm{p}}^{-} \hat{\mathbf{p}}_1^{+} \right) e^{-ik_{2z}z}$.

Once the electric and magnetic fields are determined, the spectral energy flux can be expressed by the time-averaged Poynting vector $\left\langle \mathbf{S}(\mathbf{x},\omega)\right\rangle = \frac{1}{2}\left\langle \mathrm{Re}[\mathbf{E}(\mathbf{x},\omega)\times\mathbf{H}^{*}(\mathbf{x},\omega)]\right\rangle$, where <> denotes ensemble average. In order to obtain the Poynting vector, one needs to calculate a product of electric- and magnetic-field components, such as $\left\langle E_i(\mathbf{x},\omega)H_j^{*}(\mathbf{x},\omega)\right\rangle$. Using Eqs. (6.2) and (6.6), it can be shown that

$$\left\langle E_i(\mathbf{x},\omega)H_j^{*}(\mathbf{x},\omega)\right\rangle = i\omega\mu_0 \int_{V'} d^3\mathbf{x}' \int_{V''} d^3\mathbf{x}'' \left(\bar{\bar{\mathbf{G}}}_{\mathrm{e}}\right)_{ik} \left(\bar{\bar{\mathbf{G}}}_{\mathrm{m}}^{*}\right)_{jn} \left\langle j_k(x',\omega) j_n^{*}(x'',\omega)\right\rangle \quad (6.8)$$

From the fluctuation-dissipation theorem, the spatial correlation function of current density is [102]

$$\left\langle j_k(\mathbf{x}',\omega) j_n^{*}(\mathbf{x}'',\omega)\right\rangle = \frac{4}{\pi}\omega\varepsilon_0 \,\mathrm{Im}(\varepsilon_1)\,\Theta(\omega,T_1)\,\delta_{kn}\,\delta(\mathbf{x}'-\mathbf{x}'') \quad (6.9)$$

where δ_{kn} is the Kronecker delta function and $\delta(\mathbf{x}'-\mathbf{x}'')$ is the 3D Dirac delta function. Here, $\Theta(\omega,T_1) = \hbar\omega/[\exp(\hbar\omega/k_{\mathrm{B}}T_1)-1]$ is the mean energy of a Planck oscillator at temperature T_1, where $\hbar$ is the Planck constant divided by 2π and k_{B} is the Boltzmann constant. In Eq. (6.9), the factor four is included for consistency with the conventional definition of the Poynting vector, because only positive frequencies are considered [109]. After substituting the correlation function of current density into Eq. (6.8), one can obtain that $\left\langle E_i(\mathbf{x},\omega)H_j^{*}(\mathbf{x},\omega)\right\rangle = (4i/\pi)\omega^2\varepsilon_0\mu_0\Theta(\omega,T_1)I_{ij}$, where [11]

$$I_{ij} = \frac{1}{64\pi^4}\int_{-\infty}^{0} dz' \int_{0}^{\infty} d^2\mathbf{r}' \int_{0}^{\infty} \beta d\beta \int_{0}^{\infty} \beta' d\beta' \left[\bar{\bar{\mathbf{e}}}_{ik}\bar{\bar{\mathbf{h}}}_{jk}^{*} e^{i(\beta\hat{\mathbf{r}}-\beta'\hat{\mathbf{r}})\cdot\mathbf{r}} e^{2\,\mathrm{Im}(k_{1z})z'} e^{-i(\beta\hat{\mathbf{r}}-\beta'\hat{\mathbf{r}})\cdot\mathbf{r}'}\right] \quad (6.10)$$

However, $\int_0^{\infty} d^2\mathbf{r}' e^{-i(\beta\hat{\mathbf{r}}-\beta'\hat{\mathbf{r}})\cdot\mathbf{r}'} = 4\pi^2\delta(\beta\hat{\mathbf{r}}-\beta'\hat{\mathbf{r}})$ according to the property of the 2D Dirac delta function [110]. Consequently, the double integration with respect to β and β'

in Eq. (6.10) reduces to a single integration in terms of β. The physical significance is that there is no coupling between electric and magnetic fields with different β values that will contribute to $\langle \mathbf{S}(\mathbf{x},\omega) \rangle$. Therefore, the separate treatment of the plane wave at a fixed β as done in the previous work [111] can indeed be applied to describe the energy propagation direction in nanoscale thermal radiation.

From Eq. (6.10) together with expressions of $\overline{\overline{\mathbf{e}}}$ and $\overline{\overline{\mathbf{h}}}$ given above, the spectral energy flux can be expressed:

$$\langle S_z \rangle = \frac{\Theta(\omega,T)}{\pi^2} \int_0^\infty s(\beta,\omega) d\beta \tag{6.11}$$

where

$$\begin{aligned} s(\beta,\omega) = {} & \frac{\beta \,\mathrm{Re}(k_{1z})}{4 k_{1z} k_{1z}^*} \mathrm{Re}\left[k_{2z}^* (t_\mathrm{s}^+ e^{ik_{2z}z} + t_\mathrm{s}^- e^{-ik_{2z}z})(t_\mathrm{s}^+ e^{ik_{2z}z} - t_\mathrm{s}^- e^{ik_{2z}z})^* \right] \\ & + \frac{\beta \,\mathrm{Re}(k_{1z})}{4 k_{1z} k_{1z}^*} \mathrm{Re}\left[k_{2z} (t_\mathrm{p}^+ e^{ik_{2z}z} - t_\mathrm{p}^- e^{ik_{2z}z})(t_\mathrm{p}^+ e^{ik_{2z}z} + t_\mathrm{p}^- e^{-ik_{2z}z})^* \right] \frac{(k_{1z} k_{1z}^* + \beta^2)}{k_1 k_1^*} \end{aligned} \tag{6.12}$$

The first term in the right side of the above equation indicates the contribution of *s*-polarized waves, and the second term is that of *p*-polarized waves. For non-magnetic materials, the *p*-polarized waves dominate the spectral energy flux during photon tunneling. The appearance of both t_s^+ and t_s^- (or t_p^+ and t_p^-) in Eq. (6.12) clearly represents the photon tunneling mechanism of the interaction between forward and backward evanescent waves for each polarization. However, the Poynting vector is decoupled for each parallel wavevector component. Notice that the *z*-dependent term must be canceled out because no absorption occurs in the vacuum gap, that is $\langle S_z \rangle$ is independent of *z* in the gap.

Figure 6.4 shows the near-field spectral energy flux calculated between two SiC surfaces when the vacuum gap thickness d is 100 nm. The temperature of medium 1 is assumed to be either 500 K (solid line) or 700 K (dashed line), and the temperature of medium 3 is set to be 0 K for simplicity. Hence, the energy flux from medium 3 to medium 1 is zero. In the far field, the spectral energy flux is contributed only by propagating waves in the vacuum gap (i.e., $\beta < \omega / c$). In the near field, however, evanescent waves can significantly contribute to energy transfer via photon tunneling, suggesting that Poynting vectors with $\beta > \omega / c$ become important. For considered SiC slabs, the spectral energy flux due to the propagating waves is on the order of

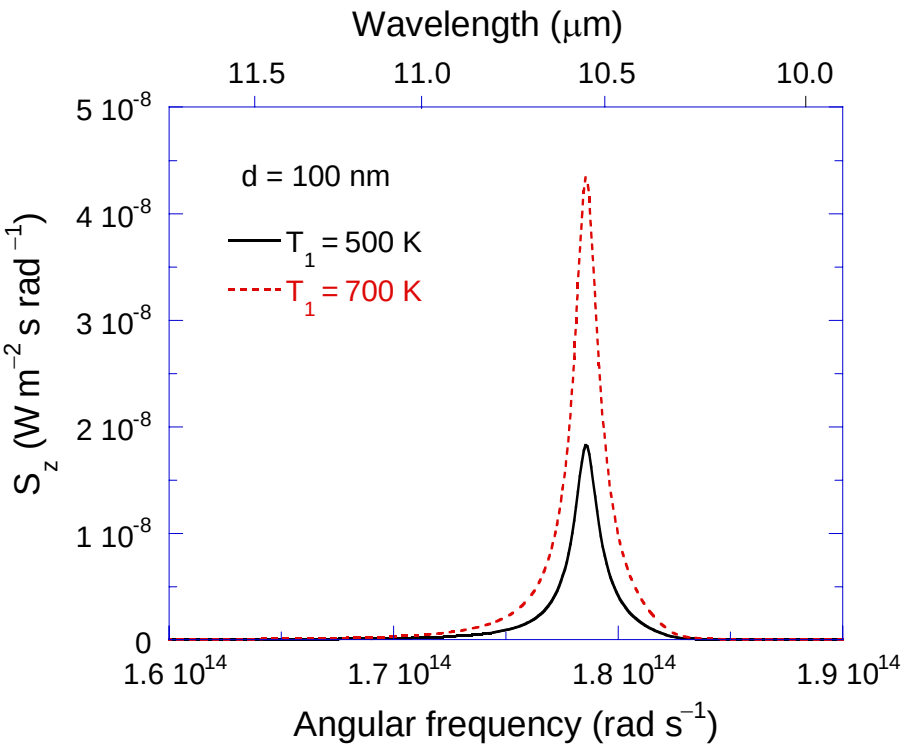

Figure 6.4 Spectral energy flux between SiC slabs when the vacuum gap thickness is 100 nm. The solid line represents the Poynting vector at emitter temperature of 500 K, and the dashed line indicates the Poynting vector at emitter temperature of 700 K. In both cases, the temperature of absorber is set to be 0 K.

10^{-11} W m^{-2}s rad^{-1} in the considered spectral region (not shown here). Therefore, the spectral energy flux in Fig. 6.4 mainly results from tunneling contributions by evanescent waves. It can be seen that for both emitter temperatures there exist sharp peaks in the spectral energy flux centered at $\lambda = 10.55$ μm. Such a nearly monochromatic enhancement on the heat transfer is a signature of surface phonon polaritons, which can be supported from SiC in the mid-infrared region. Since the evanescent waves are strongly amplified when surface polaritons are excited [25], the resulting photon tunneling can also be enhanced and thus, dominate the energy flux. For instance, the spectral energy flux at $\lambda = 10.55$ μm is approximately two orders of magnitude greater than that at other wavelengths for both emitter temperatures. Notice that surface polaritons are excited at both boundaries of the vacuum gap and strongly coupled with each other because the gap thickness is much smaller than the resonance wavelength.

To illustrate the energy propagation direction in the near field, ESLs obtained using fluctuational electrodynamics are plotted in Fig. 6.5 for selected β values at $\lambda = 10.55$ μm when surface polaritons are excited. The lateral and normal axes are normalized by the vacuum gap *d*, which is set to be 100 nm, i.e., in the proximity limit ($d << \lambda$). For propagating waves in vacuum ($\beta < \omega / c$), each ESL forms a straight line and all ESLs are located inside the conical surface bounded by the ESL at the critical angle when $\beta = \omega / c$. The lateral shift δ increases as β increases and reaches approximately 7*d* when $\beta = \omega / c$. The energy propagation direction is different from the wavevector direction due to interference between forward and backward waves. For propagating waves in the proximity limit, the energy propagation angle θ_E remains the same in the vacuum gap since ESLs are straight.

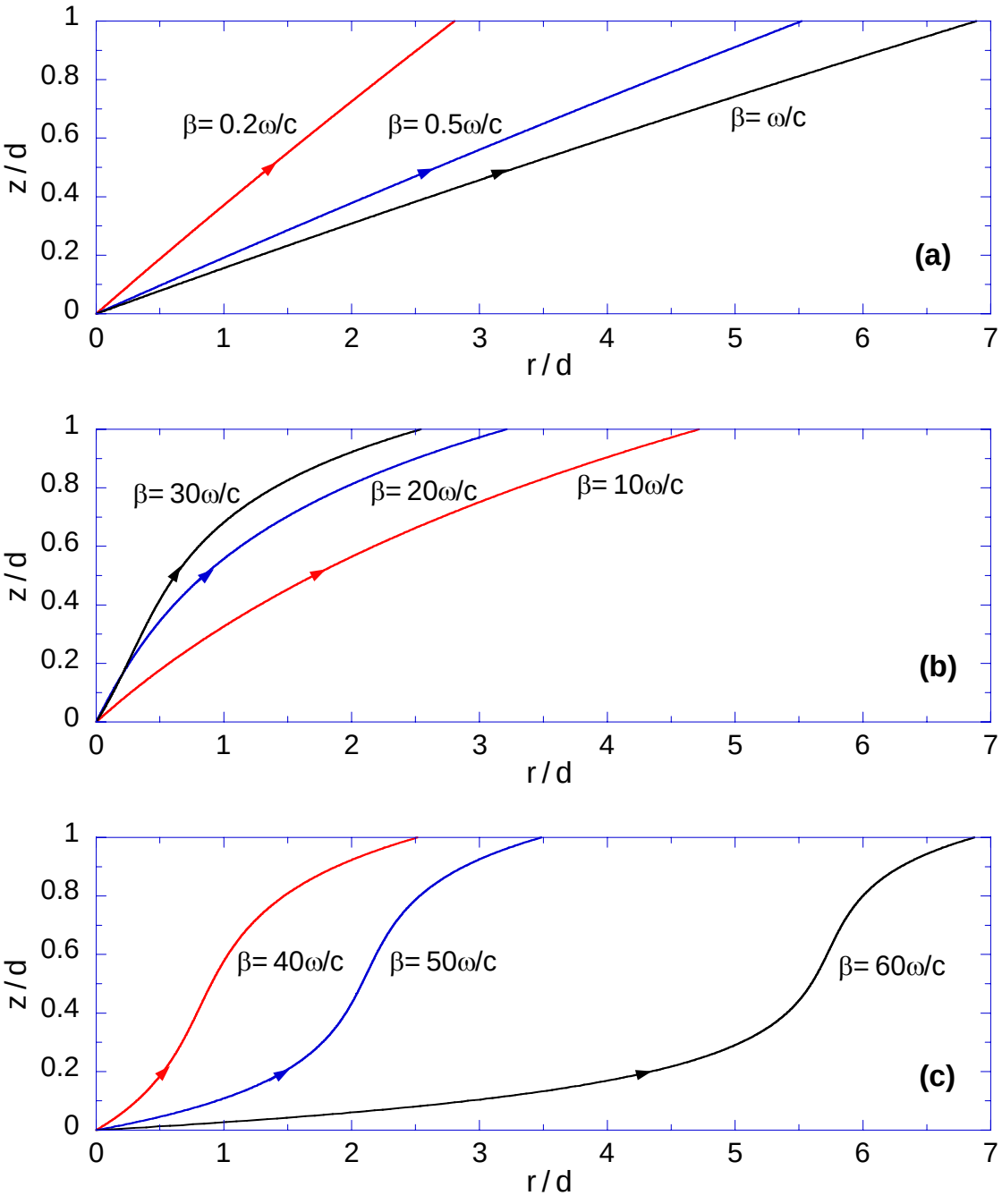

Figure 6.5 The calculated energy streamlines in the vacuum gap when d = 100 nm and the surface polaritons are excited at λ = 10.55 μm for thermal emission from the bottom surface. (a) Propagating waves; (b) $10\omega/c \le \beta \le 30\omega/c$; (c) $40\omega/c \le \beta \le 60\omega/c$.

In Fig. 6.5(b), ESLs are illustrated for $\beta = 10\omega/c$, $20\omega/c$, and $30\omega/c$ when the energy is transferred via photon tunneling (i.e., coupling of evanescent waves). In contrast to those shown in Fig. 6.5(a), the ELS for a large β value deviate from a straight line. In other words, the energy propagation angle θ_E becomes a function of z in the vacuum gap. Taking $\beta = 10\omega/c$ for instance, we obtain $\theta_E = 71°$ at $z = 0.1d$ and $\theta_E = 77°$ at $z = 0.5d$. Surprisingly, the lateral shift decreases as β increases in Fig. 6.5(b), indicating that a larger β does not necessarily cause a larger δ. Furthermore, the ESLs for large β values can be located either inside or outside the conical surface bounded by the streamlines corresponding to $\beta = \omega/c$. The curved ESL is not symmetric with respect to the mid-plane ($z = 0.5d$) although both media 1 and 3 are SiC. This may be due to the nature of coupling between forward and backward evanescent waves.

If β increases further, the ESLs become much curvier as depicted in Fig. 6.5(c) for $40\omega/c \le \beta \le 60\omega/c$. The energy propagation angle θ_E is greater than 65° at $z = 0.1d$ and decreases as z increases to the center of the vacuum gap. When z approaches medium 3, θ_E increases again. The lateral shifts of energy path in Fig. 6.5(c) are comparable to those of propagating waves. However, the lateral shift can be as large as $100d$ if $\beta = 87\omega/c$ although not shown in the figures. Since the lateral shift does not monotonically increase with β and the ESL is not a straight line in the case of photon tunneling, it is not easy to apply the concept of intensity, commonly used in radiative transfer [1], to the near field. It is worth noting that Ben-Abdallah [112] has derived a curved radiative transfer equation in weakly participating media with a generalized intensity based on the group velocity.

Figure 6.6 shows the ESL projected to the *x*-*z* plane at $\lambda = 10.55\ \mu$m and $d = 100$ nm for $\beta = 40\omega/c$ in all three media. Since the *p*-polarized waves dominate the spectral energy flux during photon tunneling for non-magnetic materials [11], the magnitude of transverse magnetic field is denoted by the colored contours (i.e., the brighter color indicates the greater value). To calculate the magnetic field, thin-film optics is employed with an assumption that a *p*-polarized plane wave is incident from medium 1. The emission originated deeper from the surface than the radiation penetration depth could not reach the SiC-vacuum interface. Hence, the field distribution is plotted in the vicinity of the vacuum gap. It can be seen from Fig. 6.6 that negative refraction of energy path occurs at the interfaces between SiC and vacuum due to the opposite sign of their dielectric functions. This observation is consistent with a previous study that proposes a SiC slab as a superlens for mid-infrared sources [113]. The energy streamlines are curved except for medium 3 where no backward waves exist. The magnetic field oscillates in the lateral direction as a result of the excitation of surface phonon polaritons.

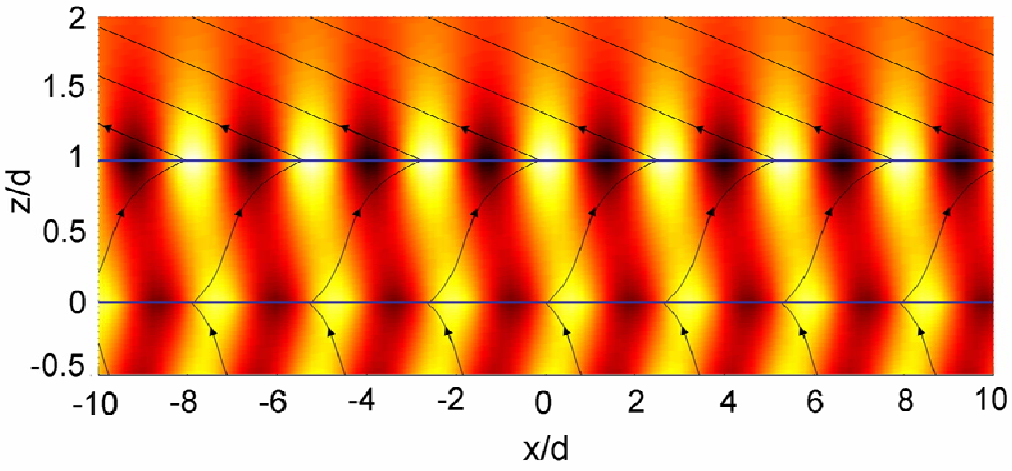

Figure 6.6 Energy streamlines in all three media for $\beta = 40\omega/c$ when $\lambda = 10.55\ \mu$m and $d = 100$ nm. The magnitude of transverse-magnetic field is denoted by colored contours.

The ESLs can be three-dimensionally illustrated and are shown in Fig. 6.7 for the same β values as in Fig. 6.5. Due to the axial symmetry, the energy streamlines form a curved conical surface, which depends on the value of β at a given wavelength. Furthermore, the net energy flux to the lateral direction must always be zero because the magnitude of Poynting vector is independent of the azimuthal angle ϕ. Since the temperature-dependent terms are cancelled out when calculating the energy propagation angle based on the Poynting vector, the ESLs shown in Figs. 6.5, 6.6, and 6.7 are independent of the emitter temperature T_1. It should be noted that, for a monochromatic plane wave incident on a subwavelength object or a periodic slit arrays, all diffracted waves are coupled coherently. The Poynting vector can be calculated by considering all the diffracted fields together, as commonly done in the literature [107,114]. Similarly, the Poynting vector analysis of superlens imaging is conducted based on the superposition of plane waves through a Fourier expansion [108]. For near-field thermal radiation, as proved in this study, the electric and magnetic fields with different parallel wavevector components are decoupled. This is a unique characteristic of thermally emitted electromagnetic waves, which arise from random fluctuating currents. Due to the coupling of forward and backward evanescent waves for given ω and β, photon tunneling may occur and can greatly enhance radiative heat transfer at the nanoscale. The spectral radiative energy is transferred in infinite directions, determined by the energy streamline that connects the Poynting vectors for each given β.

Figure 6.8 plots $s(\beta, \omega)$ defined in Eq. (6.12) as a function of β when surface polaritons are excited at $\lambda = 10.55$ μm and $d = 100$ nm. Since the spectral energy flux is proportional to the integration of $s(\beta, \omega)$ over β, one can identify the important β ranges

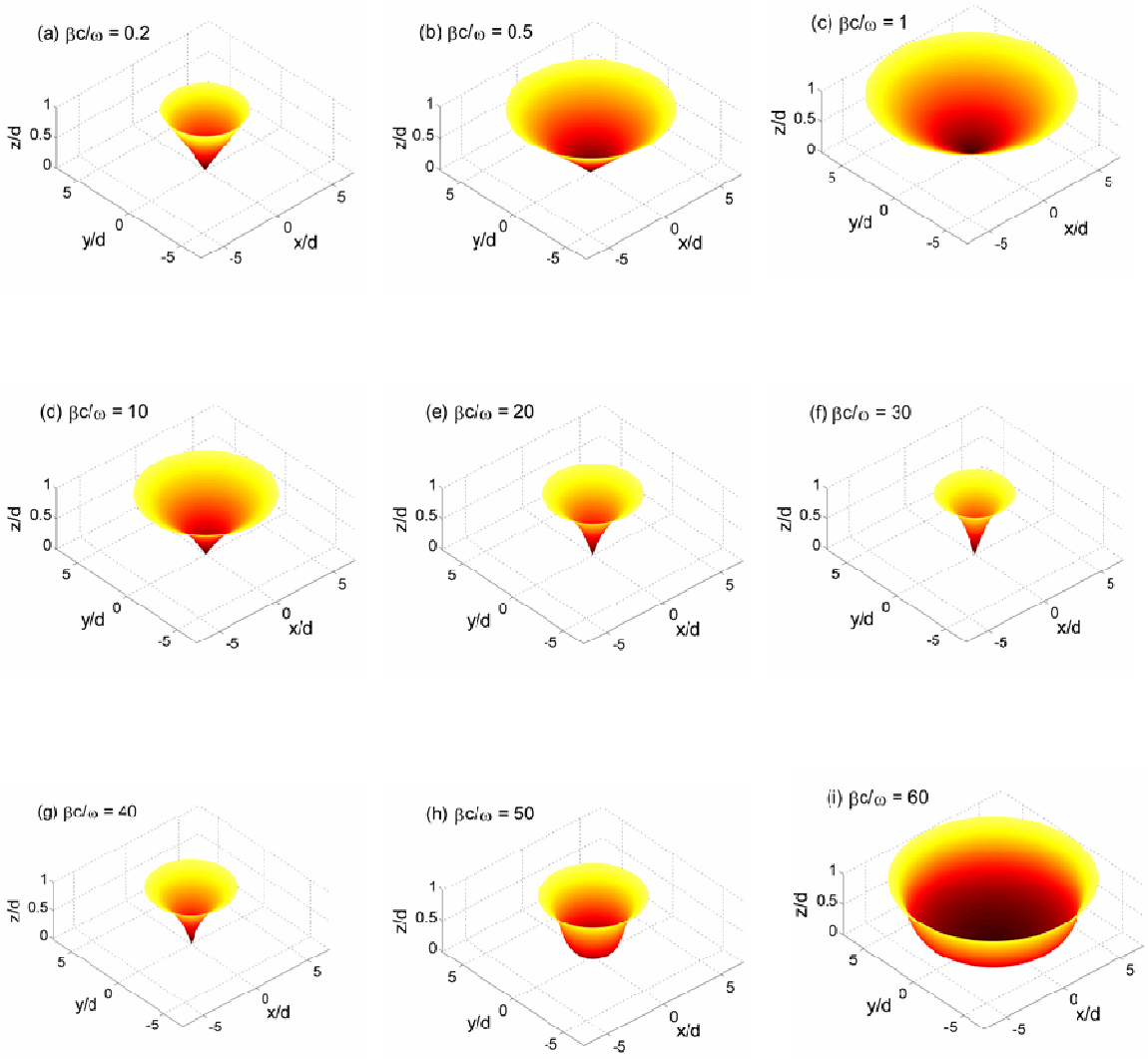

Figure 6.7 Three-dimensional illustration of energy streamline in the vacuum gap for the same conditions as Fig. 6.5. The radiative heat flux is transferred from the bottom to the top surfaces.

for the energy transfer from Fig. 6.8. It can be seen that $s(\beta, \omega)$ has a wide peak around $\beta = 49.0\omega/c$. The FWHM of the peak is estimated to be $35.3\omega/c < \beta < 64.2\omega/c$, as denoted by the shaded region in the figure. The calculation reveals that approximately 70% of the spectral energy flux is due to evanescent waves with β values located in the FWHM. In general, evanescent waves with $\beta >> \omega/c$ quickly decay in vacuum, so that they may not largely contribute to photon tunneling (i.e., energy transfer) through the gap. However, surface-polariton excitation enables those evanescent waves to contribute the energy transfer. Note that the surface-polariton excitation is a resonance phenomenon, whose excitation condition is usually confined in a narrow ω band at a given β or alternatively, in a narrow β region at a given ω. On the other hand, there exists a particular ω where surface polaritons can be excited in a wide range of β. In other words, the dispersion curve of surface polaritons becomes almost flat in the $\omega - \beta$ plane [115]. At this frequency, evanescent waves in a broad band of β, whose value is much greater than ω/c, can be significantly enhanced by coupling with surface polaritons and therefore, largely contribute to photon tunneling.

Figure 6.8(b) shows the lateral shift of energy streamlines as a function of β. The shaded region corresponds to the FWHM of $s(\beta, \omega)$ determined in Fig. 6.8(a). As noted earlier, the lateral shift does not monotonically increase with β in the near field. When $\beta < 1.4\omega/c$, for instance, the lateral shift increases with β until $\delta = 7d$. As β increases further, δ decreases to $2.4d$ around $\beta = 36\omega/c$ and then monotonically increases. Since almost 70% of the spectral energy is transferred by the evanescent waves, whose β values are inside the FWHM, the dominant energy transfer occurs with ESLs in Fig. 6.5(c) and

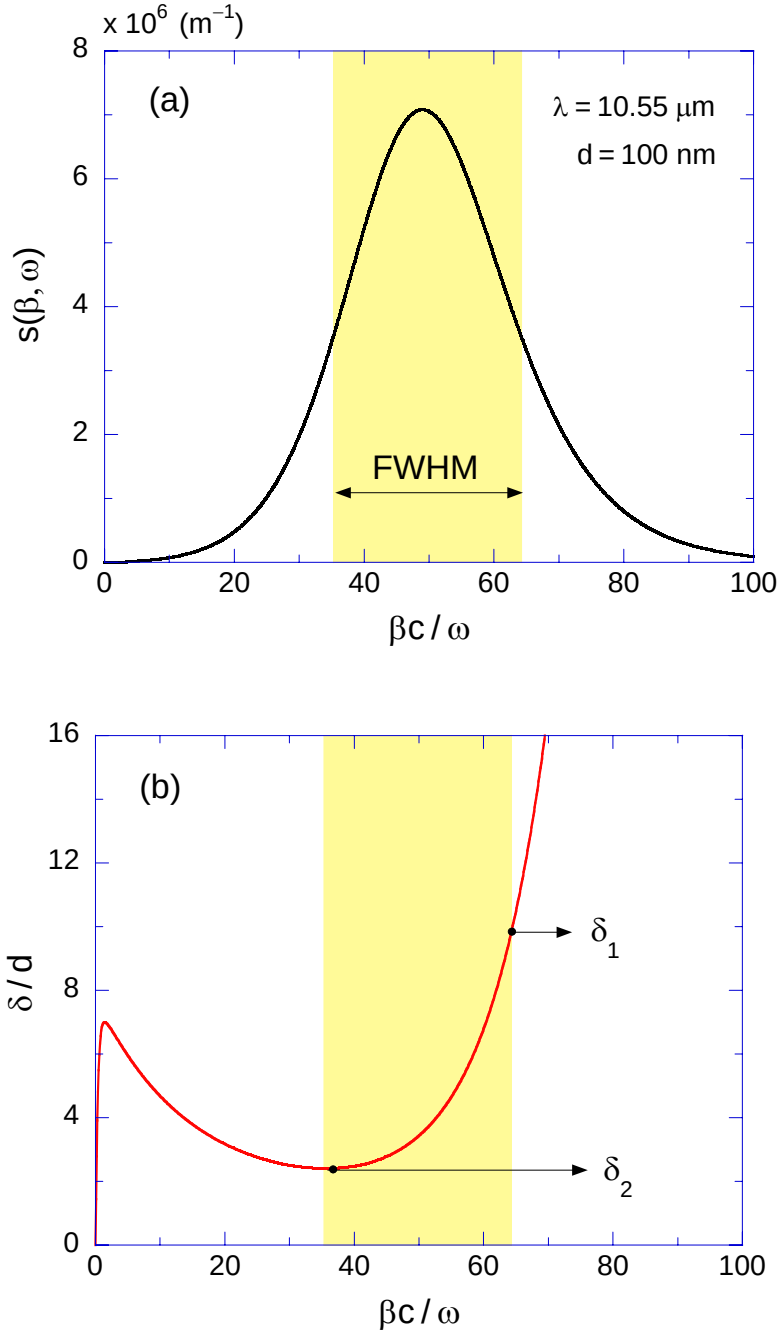

Figure 6.8 Important β range for the spectral energy flux: (a) Plot of $s(\beta,\omega)$ in terms of β; (b) The lateral shift of energy pathway as a function of β. The shaded region represents the FWHM of $s(\beta,\omega)$. Approximately 70% of the spectral energy flux is due to evanescent waves whose β values are located in the shaded region.

the lateral shift in the shaded region is important for the practical application of near-field radiation. As illustrated in Fig. 6.8(b), the lateral shift of ESLs varies from $\delta_2 = 2.4d$ to $\delta_1 = 9.8d$ if evanescent waves with β's in the FWHM are considered.

The effects of surface polaritons on the energy streamline and the lateral shift are now considered. The function $s(\beta, \omega)$ is illustrated as a contour plot with respect to the angular frequency and the parallel wavevector component in Fig. 6.9(a). The color bar in the right on the figure shows the scale of $s(\beta, \omega)$ in 10^6 m^{-1}, such that brighter color represents higher value of it. It can be clearly seen that large portion of the total energy is confined in a narrow band near the 10.55 μm. Since $\Theta(\omega, T)$ is nearly constant in the narrow spectral band, the volume under the 3D surface of $s(\beta, \omega)$ can be approximated to be proportional to the total energy flux. Due to the resonance characteristics, the energy flux is greatly enhanced with the surface-polariton excitation; thus, the function $s(\beta, \omega)$ has the maximum value at 10.55 μm.

The calculated dispersion curves for surface polaritons between two SiC surfaces are plotted in Fig. 6.9(b). In the calculation, only the real part of the dielectric function of SiC is considered [25]. Due to the coupling of surface polaritons at both vacuum-SiC interfaces, there exist two branches of dispersion curves. The lower-frequency branch corresponds to the symmetric mode, and the higher-frequency branch represents the asymmetric mode [101]. It can be seen that the region with high $s(\beta, \omega)$ values match well the polariton dispersion curves. Since the FWHM of $s(\beta, \omega)$ in the β axis becomes narrower and the peak location shifts to smaller β values less than $10\omega/c$ as the wavelength deviates from 10.55 μm, the contribution of the Poynting vector to the total

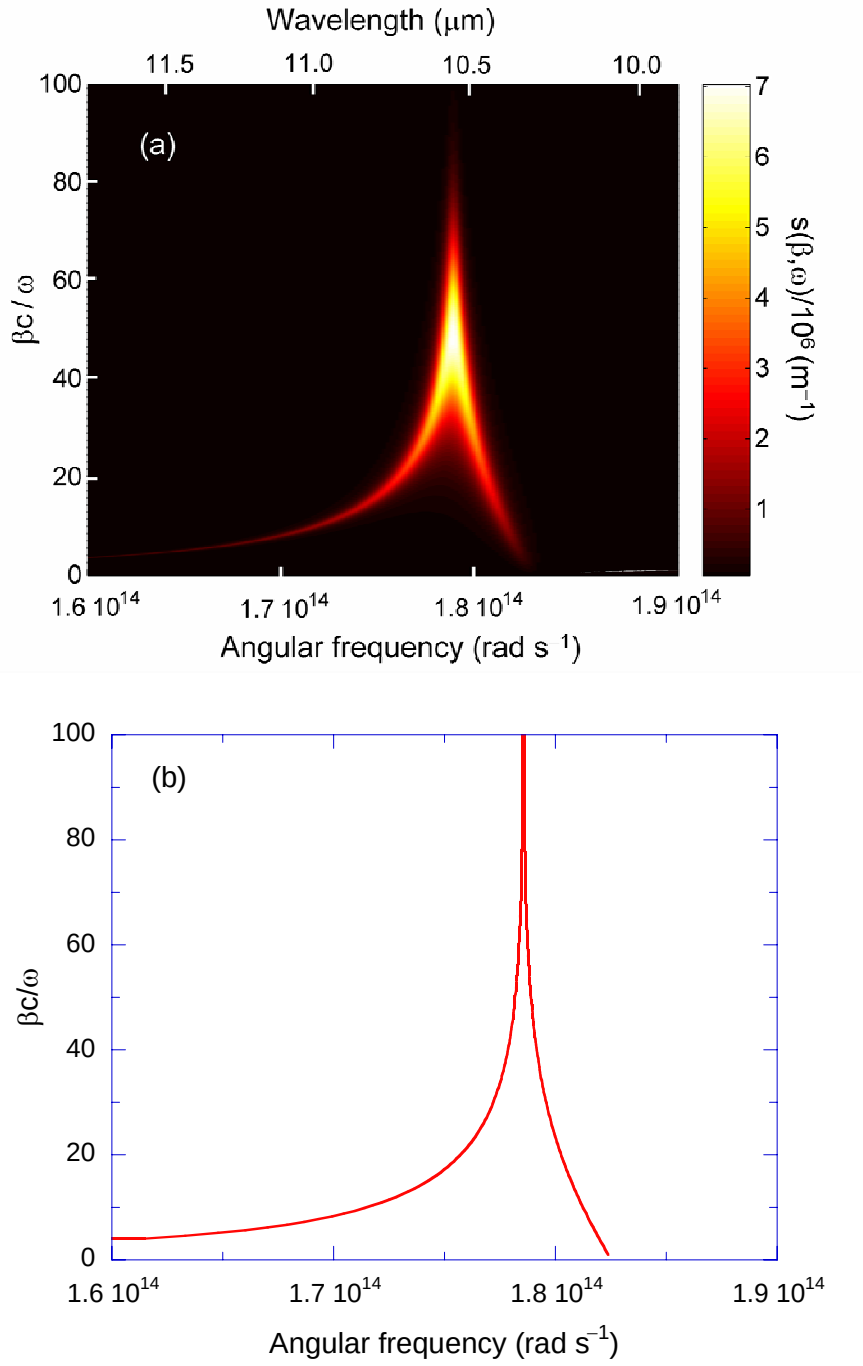

Figure 6.9 Effect of surface polaritons on the total energy flux: (a) Contour plot of $s(\beta,\omega)$ with respect to the angular frequency and the parallel wavevector component. The volume under the three-dimensional surface is proportional to the total energy flux; (b) Surface polariton dispersion curves.

energy flux significantly decreases accordingly. In other words, the flat region of the dispersion curve in the $\omega - \beta$ plane dominantly contributes to the total energy flux, even though surface polaritons are also excited at other wavelengths.

Figure 6.10 shows the lateral shifts of ESLs in the wavelength range from 10.4 μm to 10.7 μm. Here, approximately 80% of total energy flux is confined in this wavelength region at both $T_1 = 500$ K and 700 K (refer to Fig. 6.4). For different wavelengths, δ_1 and δ_2 are evaluated similarly as done in Fig. 6.8(b). Therefore, the hatched region in Fig. 6.10 includes the lateral shifts due to the evanescent waves whose β values are in the FWHM of $s(\beta, \omega)$ for wavelengths from 10.4 μm to 10.7 μm. The change of the difference between lateral shifts of δ_1 and δ_2 with respect to the

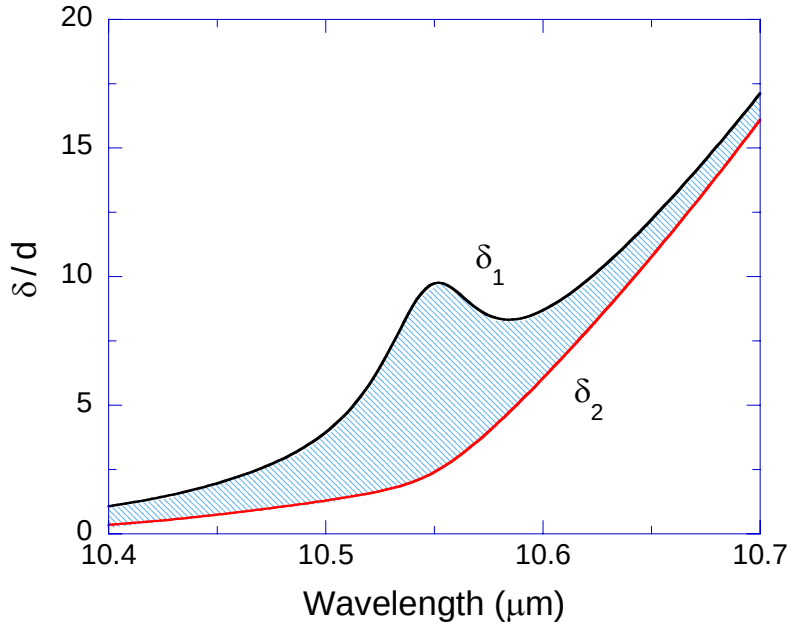

Figure 6.10 Lateral shifts of the energy pathways in the wavelength region from 10.45 μm to 10.65 μm. Approximately 80% of the total energy is confined in the above wavelength range. The hatched region represents the lateral shifts due to evanescent waves with β values in the FWHM of $s(\beta, \omega)$.

wavelength is consistent with the observation that the FWMH becomes wider near the resonance wavelength of 10.55 μm. Surprisingly, the lateral shift does not significantly increase when surface polaritons occurs in contrast to the spectral energy flux.

For two wavelengths of 10.5 μm and 10.6 μm (i.e., 0.1 μm away from the polariton-resonance wavelength), the FWHM of $s(\beta, \omega)$ are estimated to be $25\omega/c < \beta < 42\omega/c$ and $29\omega/c < \beta < 43\omega/c$, respectively from Fig. 6.9. Although the FWHM are comparable for both wavelengths, the corresponding lateral shift is $1.3d < \delta < 4.0d$ and $6.1d < \delta < 8.7d$, respectively, as shown in Fig. 6.10. Therefore, the resulting lateral shifts can be different for different wavelengths even though the considered β regions are similar. An important question is how large an area is needed for the surfaces to be considered as semi-infinite when energy is transferred from one to another medium via photon tunneling. To eliminate the edge effect, let us choose the lateral dimension of the surface to be five times the lateral shift. This implies that the lateral dimension of the SiC slab needs to be about $100d$ for 80% of the total energy flux to tunnel through the vacuum gap with negligible edge effects. It should be noted that the estimated lateral dimension of the SiC slab is still applicable although the vacuum gap thickness d changes because of the similarity in the lateral shift as demonstrated in Ref. [111]. Furthermore, if the temperature of medium 3 is set to be greater than 0 K, one can separately construct the ESLs from medium 3 to medium 1 by letting the temperature of medium 1 as zero, similar to the calculation of the spectral energy flux from medium 3 to medium 1. This is because the thermally emitted electromagnetic waves from medium 3 are not coupled to those from medium 1. Therefore, analysis presented in this study can be easily extended to more complicated configurations.

CHAPTER 7

CONCLUSIONS AND RECOMMENDATIONS

This dissertation provides a theoretical and experimental investigation of coherent thermal emission based on thin-film multilayer structures. In order to understand the mechanism of tailoring thermal emission, detailed theoretical study is conducted for a multilayer structure consist of a SiC film coated on a semi-infinite 1D PC. A regime map is developed to identify different mechanisms (i.e., surface-wave excitation, cavity resonance and the Brewster mode) that are responsible for large emissivity values. By coating a SiC film on the 1D PC, surface waves can be directly coupled to propagating waves in air when the wavelengths and emission angles are within the SiC phonon absorption band as well as the PC's stop band. It is shown that the emissivity with surface-wave excitations can be tuned by changing the thickness of SiC layer as well as the thickness of the dielectric next to SiC (i.e., surface termination). On the other hand, cavity resonance can occur from the SiC-on-PC structure when the wavelengths and incidence angles are in the stop band of the PC but outside of the SiC phonon absorption band. At the resonance condition, standing waves exist in the SiC layer, resulting in diffuse emission within a narrow spectral band. Furthermore, for TM waves, a region where the Brewster mode can be excited is also identified. The angular lobe of the emissivity due to the Brewster mode exhibits a width between those of the surface wave excitation and cavity resonance mode.

In order to experimentally demonstrate coherent emission characteristics, we have modified the original design of the SiC-on-PC structure and fabricated much simpler

samples. One structure involves a truncated 1D PC with several unit cells coated on a metal (Ag). The major advantage of the PC-on-Ag structure over the SiC-on-PC structure is the use of PCs with fewer unit cells. Furthermore, the metallic film enables coherent thermal emission in the near-IR region, with much thinner constituent dielectrics than those of the SiC-on-PC structure. The other structure is the asymmetric Fabry-Pérot resonator made of the SiO_2 cavity coated with different-thickness Ag films on both sides. When standing waves exist inside the cavity, sharp spectral peaks and narrow angular lobes can be achieved in the spectral-directional emissivity. The thicker Ag layer mainly serves as a reflector, and the thinner Ag film in front of the dielectric layer contributes mostly to the emission of the structure.

We have verified theoretical predictions of coherent thermal emission by measuring the reflectance of the fabricated PC-on-Ag structure at room temperature. A FTIR spectrometer was used to measure the spectral reflectance at incidence angles of 10°, 30°, and 40°. A laser scatterometer was also used to measure the angle-resolved reflectance at the wavelength of 891 nm. The measured reflectance shows sharp dips caused by the excitation of surface waves near 1 μm in the stop band of the PC. Based on Kirchhoff's law, the emissivity is calculated from the measured reflectance, and excellent temporal and spatial coherence is achieved for the fabricated PC-on-Ag structure. Furthermore, the dispersion relations of surface waves are calculated based on the supercell method with modified matrix equations to guarantee the convergence of solutions for TM waves, especially when a metallic layer is involved. It is found that frequencies and incidence angles where the measured reflectance exhibits sharp dips agree very well with the surface-wave dispersion curves for both polarizations. Along

with the dispersion curves, calculated field magnitude at the PC-Ag interface also confirms the existence of surface waves where the field is highly localized. Results obtained from this dissertation will facilitate applications of coherent thermal-emission sources in energy conversion such as thermophotovoltaic devices, and in thermal management by modifying radiative energy transfer.

This dissertation also investigates the energy propagation direction in photon tunneling and near-field thermal radiation. For either propagating waves or evanescent waves, the Poynting vector in the near field is not parallel to the wavevector due to the coupling between forward and backward waves. Moreover, it is not a straight line even in vacuum. For photon tunneling between dielectrics, propagating waves are squeezed towards the axis due to interference and form a cone around the centerline, giving an external conical space for the coupled evanescent waves to carry energy through the barrier. When the gap thickness is much smaller than the characteristic wavelength, the energy streamline is almost a straight line and the energy propagation angle allows the determination of lateral shift of the energy path through photon tunneling.

By employing the fluctuational electrodynamics, this research shows that when nanoscale radiation between two parallel plates is considered, the Poynting vector is decoupled for each parallel wavevector component β due to the random nature of thermal emission. The streamlines calculated by tracing the Poynting vector vividly demonstrate that the spectral radiative energy travels in infinite directions along curved lines. At the wavelength of 10.55 μm where the surface-wave dispersion curve becomes almost flat in the $\omega - \beta$ plane, approximately 70% of the spectral energy flux is contributed by photon tunneling with $35\omega / c < \beta < 64\omega / c$. On the other hand, a large portion of the spectral

energy is carried by evanescent waves with $\beta < 10\omega/c$ if the wavelength deviates from 10.55 μm. Depending on the β value, the energy pathway exhibits considerable lateral shift, which could be a crucial factor in the design of devices based on nanoscale radiation heat transfer. It is shown that the lateral dimension of the SiC slab needs to be $100d$ for approximately 80% of the total energy flux to tunnel through the vacuum gap with negligible edge effects. The prediction of lateral shift is critical to the design of near-field thermophotovoltaic systems, thermal radiation scanning tunneling microscopy, and scanning photon-tunneling microscopy.

In this dissertation, the feasibility of controlling thermal emission by employing photonic crystals has been demonstrated at room temperature. From the reflectance measurements, we have observed considerable differences between the measured and predicted reflectance spectra especially in the higher frequency region. One possible explanation for these discrepancies was additional losses in the deposited Ag film as compared to the tabulated values. In the future, it is necessary to systemically investigate the optical constants of the sputtered and evaporated Ag films. In addition, fabricating a new sample optimized for the mid-IR spectral region will also be important. In this case, a Ag film can be replaced by a SiC or SiO_2 layer depending on the spectral region, and the constituent dielectrics should be replaced accordingly with increased thicknesses.

The next step is to examine coherent thermal emission at elevated temperatures. To achieve this end, the structural stability must be carefully examined. Seeking alternative materials with desired optical and thermal properties may be necessary to improve the stability and performance of the structure at elevated temperatures. The deposition method of thin films alters mechanical properties of the fabricated structure

and thus, may also affect their stability. In addition, direct measurement of the emission from a heated sample needs to be performed, which requires developing an emissometer with high accuracy and reliability. From the theoretical point of view, more complicated structure such as 2D or 3D PCs can be investigated to construct coherent emission sources. Thermal emission can be directly modeled by using the rigorous coupled-wave analysis or finite-difference time-domain method, coupled with the fluctuation-dissipation theorem. The supercell method can also be extended to predict the surface-wave dispersion relation at the interface between PC and another medium.

For the near-field thermal radiation, it is critical to experimentally demonstrate the large enhancement of the energy flux between two parallel plate separated by a nanometer-scale vacuum gap. In fact, there is lack of the quantitative measurements of near-field thermal radiation when the gap thickness is less than 100 nm. Polar materials such as SiC and SiO_2 that support surface-phonon polaritons can be used to study the mechanisms of near-field radiation heat transfer. In the experiment, the most challenging part is to maintain the nanometer distance between two parallel plates. One can use well-designed nanoparticles or nanospacers for the gap distance below 100 nm. By reducing the portion of the contact area by particles or spacers, the heat conduction through them can be neglected.

REFERENCES

[1] Siegel, R., and Howell, J. R., 2002, *Thermal Radiation Heat Transfer*, 4th ed., Taylor & Francis, NY.

[2] Hesketh, P. J., Zemel, J. N., and Gebhart, B., 1986, "Organ Pipe Radiant Modes of Periodic Micromachined Silicon Surfaces," Nature, **324**, 549-551.

[3] Hesketh, P. J., Gebhart, B., and Zemel, J. N., 1988, "Measurements of the Spectral and Directional Emission from Microgrooved Silicon Surfaces," J. Heat Transfer, **110**, 680-686.

[4] Sai, H., Yugami, H., Kanamori, Y., and Hane, K., 2003, "Spectrally Selective Thermal Radiators and Absorbers with Periodic Microstructured Surface for High-Temperature Applications," Microscale Thermophys. Eng., **7**, 101-115.

[5] Perlmutter, M., and Howell, J. R., 1963, "A Strongly Directional Emitting and Absorbing Surface," J. Heat Transfer, **85**, 282-283.

[6] Dimenna, R. A., and Buckius, R. O., 1994, "Electromagnetic Theory Predictions of the Directional Scattering from Triangular Surfaces," J. Heat Transfer, **116**, 639-645.

[7] Chen, Y.-B., Zhu, Q. Z., Wright, T. L., King, W. P., and Zhang, Z. M., 2004, "Bidirectional Reflection Measurements of Periodically Microstructured Silicon Surfaces," Int. J. Thermophy., **25**, 1235-1252.

[8] Coutts, T. J., 1999, "A Review of Progress in Thermophotovoltaic Generation of Electricity," Renewable Sustainable Energy Rev., **3**, 77-184.

[9] Heinzel, A., Boerner, V., Gombert, A., Blasi, B., Wittwer, V., and Luther, J., 2000, "Radiation Filters and Emitters for the NIR Based on Periodically Structured Metal Surfaces," J. Mod. Opt., **47**, 2399-2419.

[10] Zhang, Z. M., 2007, *Nano/Microscale Heat Transfer*, McGraw-Hill, New York.

[11] Joulain, K., Mulet, J.-P., Marquier, F., Carminati, R., and Greffet, J.-J., 2005, "Surface Electromagnetic Waves Thermally Excited: Radiative Heat Transfer, Coherence Properties and Casimir Forces Revisited in the near Field," Surf. Sci. Rep., **57**, 59-112.

[12] Fleming, J. G., Lin, S. Y., El-Kady, I., Biswas, R., and Ho, K. M., 2002, "All-Metallic Three-Dimensional Photonic Crystals with a Large Infrared Bandgap," Nature, **417**, 52-55.

[13] Narayanaswamy, A., and Chen, G., 2004, "Thermal Emission Control with One-Dimensional Metallodielectric Photonic Crystals," Phys. Rev. B, **70**, 125101.

[14] Enoch, S., Simon, J.-J., Escoubas, L., Elalmy, Z., Lemarquis, F., Torchio, P., and Albrand, G., 2005, "Simple Layer-by-Layer Photonic Crystal for the Control of Thermal Emission," Appl. Phys. Lett., **86**, 261101.

[15] Ben-Abdallah, P., and Ni, B., 2005, "Single-Defect Bragg Stacks for High-Power Narrow-Band Thermal Emission," J. Appl. Phys., **97**, 104910.

[16] Celanovic, I., Perreault, D., and Kassakian, J., 2005, "Resonant-Cavity Enhanced Thermal Emission," Phys. Rev. B, **72**, 075127.

[17] Fu, C. J., Zhang, Z. M., and Tanner, D. B., 2005, "Planar Heterogeneous Structures for Coherent Emission of Radiation," Opt. Lett., **30**, 1873-1875.

[18] Battula, A., and Chen, S. C., 2006, "Monochromatic Polarized Coherent Emitter Enhanced by Surface Plasmons and a Cavity Resonance," Phys. Rev. B, **74**, 245407.

[19] Laroche, M., Marquier, F., Carminati, R., and Greffet, J.-J., 2005, "Tailoring Silicon Radiative Properties," Opt. Commun., **250**, 316-320.

[20] Biswas, R., Ding, C., Puscasu, I., Pralle, M., McNeal, M., Daly, J., Greenwald, A., and Johnson, E., 2006, "Theory of Subwavelength Hole Arrays Coupled with Photonic Crystals for Extraordinary Thermal Emission," Phys. Rev. B, **74**, 045107.

[21] Chan, D. L. C., Soljacic, M., and Joannopoulos, J. D., 2006, "Thermal Emission and Design in 2D-Periodic Metallic Photonic Crystal Slabs," Opt. Express, **14**, 8785-8796.

[22] Kreiter, M., Oster, J., Sambles, R., Herminghaus, S., Mittler-Neher, S., and Knoll, W., 1999, "Thermally Induced Emission of Light from a Metallic Diffraction Grating, Mediated by Surface Plasmons," Opt. Commun., **168**, 117-122.

[23] Laroche, M., Arnold, C., Marquier, E., Carminati, R., Greffet, J.-J., Collin, S., Bardou, N., and Pelouard, J. L., 2005, "Highly Directional Radiation Generated by a Tungsten Thermal Source," Opt. Lett., **30**, 2623-2625.

[24] Greffet, J.-J., Carminati, R., Joulain, K., Mulet, J.-P., Mainguy, S., and Chen, Y., 2002, "Coherent Emission of Light by Thermal Sources," Nature, **416**, 61-64.

[25] Raether, H., 1988, *Surface Plasmons on Smooth and Rough Surfaces and on Gratings*, Springer-Verlag, Berlin.

[26] Marquier, F., Laroche, M., Carminati, R., and Greffet, J.-J., 2007, "Anisotropic Polarized Emission of a Doped Silicon Lamellar Grating," J. Heat Transfer, **129**, 11-16.

[27] Enoch, S., Tayeb, G., Sabouroux, P., Guerin, N., and Vincent, P., 2002, "A Metamaterial for Directive Emission," Phys. Rev. Lett., **89**, 213902.

[28] Maruyama, S., Kashiwa, T., Yugami, H., and Esashi, M., 2001, "Thermal Radiation from Two-Dimensionally Confined Modes in Microcavities," Appl. Phys. Lett., **79**, 1393-1395.

[29] Schubert, E. F., Hunt, N. E. J., Vredenberg, A. M., Harris, T. D., Poate, J. M., Jacobson, D. C., Wong, Y. H., and Zydzik, G. J., 1993, "Enhanced Photoluminescence by Resonant Absorption in Er-Doped SiO_2/Si Microcavities," Appl. Phys. Lett., **63**, 2603-2605.

[30] Pralle, M. U., Moelders, N., McNeal, M. P., Puscasu, I., Greenwald, A. C., Daly, J. T., Johnson, E. A., George, T., Choi, D. S., El-Kady, I., and Biswas, R., 2002, "Photonic Crystal Enhanced Narrow-Band Infrared Emitters," Appl. Phys. Lett., **81**, 4685-4687.

[31] Lin, S. Y., Moreno, J., and Fleming, J. G., 2003, "Three-Dimensional Photonic-Crystal Emitter for Thermal Photovoltaic Power Generation," Appl. Phys. Lett., **83**, 380-382.

[32] Ashcroft, N. W., and Mermin, N. D., 1976, *Solid State Physics*, Harcourt College Publishers, Fort Worth, TX.

[33] Joannopoulos, J. D., Meade, R. D., and Winn, J. N., 1995, *Photonic Crystals*, Princeton University Press, Princeton, NJ.

[34] Villa, F., and Gaspar-Armenta, J. A., 2004, "Photonic Crystal to Photonic Crystal Surface Modes: Narrow-Bandpass Filters," Opt. Express, **12**, 2338-2355.

[35] Morrison, S. K., and Kivshar, Y. S., 2005, "Engineering of Directional Emission from Photonic-Crystal Waveguides," Appl. Phys. Lett., **86**, 081110.

[36] Yeh, P., Yariv, A., and Hong, C. S., 1977, "Electromagnetic Propagation in Periodic Stratified Media. 1. General Theory," J. Opt. Soc. Am. A, **67**, 423-438.

[37] Yeh, P., Yariv, A., and Cho, A., 1978, "Optical Surface-Waves in Periodic Layered Media," Appl. Phys. Lett., **32**, 104-105.

[38] Robertson, W. M., 1999, "Experimental Measurement of the Effect of Termination on Surface Electromagnetic Waves in One-Dimensional Photonic Bandgap Arrays," J. Lightwave Technol., **17**, 2013-2017.

[39] Robertson, W. M., and May, M. S., 1999, "Surface Electromagnetic Wave Excitation on One-Dimensional Photonic Band-Gap Arrays," Appl. Phys. Lett., **74**, 1800-1802.

[40] Gaspar-Armenta, J. A., and Villa, F., 2003, "Photonic Surface-Wave Excitation: Photonic Crystal-Metal Interface," J. Opt. Soc. Am. B, **20**, 2349-2354.

[41] Sai, H., Kanamori, Y., and Yugami, H., 2003, "High-Temperature Resistive Surface Grating for Spectral Control of Thermal Radiation," Appl. Phys. Lett., **82**, 1685-1687.

[42] Laroche, M., Carminati, R., and Greffet, J.-J., 2006, "Coherent Thermal Antenna Using a Photonic Crystal Slab," Phys. Rev. Lett., **96**, 123903.

[43] Seager, C. H., Sinclair, M. B., and Fleming, J. G., 2005, "Accurate Measurements of Thermal Radiation from a Tungsten Photonic Lattice," Appl. Phys. Lett., **86**, 244105.

[44] Cravalho, E. G., Tien, C. L., and Caren, R. P., 1967, "Effect of Small Spacings on Radiative Transfer between 2 Dielectrics," J. Heat Transfer, **89**, 351-358.

[45] Polder, D., and Vanhove, M., 1971, "Theory of Radiative Heat Transfer between Closely Spaced Bodies," Phys. Rev. B, **4**, 3303-3314.

[46] Loomis, J. J., and Maris, H. J., 1994, "Theory of Heat-Transfer by Evanescent Electromagnetic-Waves," Phys. Rev. B, **50**, 18517-18524.

[47] Shchegrov, A. V., Joulain, K., Carminati, R., and Greffet, J.-J., 2000, "Near-Field Spectral Effects Due to Electromagnetic Surface Excitations," Phys. Rev. Lett., **85**, 1548-1551.

[48] Volokitin, A. I., and Persson, B. N. J., 2004, "Resonant Photon Tunneling Enhancement of the Radiative Heat Transfer," Phys. Rev. B, **69**, 045417.

[49] Hall, E. E., 1902, "The Penetration of Totally Reflected Light into the Rarer Medium," Phys. Rev., **15**, 73-106.

[50] Zhang, Z. M., and Fu, C. J., 2002, "Unusual Photon Tunneling in the Presence of a Layer with a Negative Refractive Index," Appl. Phys. Lett., **80**, 1097-1099.

[51] Fang, N., Lee, H., Sun, C., and Zhang, X., 2005, "Sub-Diffraction-Limited Optical Imaging with a Silver Superlens," Science, **308**, 534-537.

[52] Martin-Moreno, L., Garcia-Vidal, F. J., Lezec, H. J., Degiron, A., and Ebbesen, T. W., 2003, "Theory of Highly Directional Emission from a Single Subwavelength Aperture Surrounded by Surface Corrugations," Phys. Rev. Lett., **90**, 167401.

[53] Srituravanich, W., Fang, N., Sun, C., Luo, Q., and Zhang, X., 2004, "Plasmonic Nanolithography," Nano Letters, **4**, 1085-1088.

[54] Muller-Hirsch, W., Kraft, A., Hirsch, M. T., Parisi, J., and Kittel, A., 1999, "Heat Transfer in Ultrahigh Vacuum Scanning Thermal Microscopy," J. Vac. Sci. Technol. A, **17**, 1205-1210.

[55] Kittel, A., Muller-Hirsch, W., Parisi, J., Biehs, S. A., Reddig, D., and Holthaus, M., 2005, "Near-Field Heat Transfer in a Scanning Thermal Microscope," Phys. Rev. Lett., **95**, 224301.

[56] De Wilde, Y., Formanek, F., Carminati, R., Gralak, B., Lemoine, P. A., Joulain, K., Mulet, J.-P., Chen, Y., and Greffet, J.-J., 2006, "Thermal Radiation Scanning Tunnelling Microscopy," Nature, **444**, 740-743.

[57] Narayanaswamy, A., and Chen, G., 2003, "Surface Modes for Near Field Thermophotovoltaics," Appl. Phys. Lett., **82**, 3544-3546.

[58] Laroche, M., Carminati, R., and Greffet, J.-J., 2006, "Near-Field Thermophotovoltaic Energy Conversion," J. Appl. Phys., **100**, 063704.

[59] Planck, M., 1959, *The Theory of Heat Radiation*, Dover, New York.

[60] Steinberg, A. M., and Chiao, R. Y., 1994, "Tunneling Delay Times in One and Two Dimensions," Phy. Rev. A, **49**, 3283-3295.

[61] Broe, J., and Keller, O., 2002, "Quantum-Well Enhancement of the Goos-Hänchen Shift for P-Polarized Beams in a Two-Prism Configuration," J. Opt. Soc. Am. A, **19**, 1212-1222.

[62] Kim, K.-Y., 2004, "Photon Tunneling in Composite Layers of Negative- and Positive-Index Media," Phys. Rev. E, **70**, 047603.

[63] Chen, Y.-Y., Huang, Z. M., Wang, Q., Li, C.-F., and Shi, J. L., 2005, "Photon Tunnelling in One-Dimensional Metamaterial Photonic Crystals," J. Opt. A, **7**, 519-524.

[64] Lai, H. M., Kwok, C. W., Loo, Y. W., and Xu, B. Y., 2000, "Energy-Flux Pattern in the Goos-Hänchen Effect," Phys. Rev. E, **62**, 7330-7339.

[65] Alu, A., and Engheta, N., 2003, "Pairing an Epsilon-Negative Slab with a Mu-Negative Slab: Resonance, Tunneling and Transparency," IEEE Trans. Antennas Propag., **51**, 2558-2571.

[66] Cui, T. J., Hao, Z. C., Yin, X. X., Hong, W., and Kong, J. A., 2004, "Study of Lossy Effects on the Propagation of Propagating and Evanescent Waves in Left-Handed Materials," Phys. Lett. A, **323**, 484-494.

[67] Grzegorczyk, T. M., Moss, C. D., Lu, J., Chen, X. D., Pacheco, J., and Kong, J. A., 2005, "Properties of Left-Handed Metamaterials: Transmission, Backward Phase, Negative Refraction, and Focusing," IEEE Trans. Microwave Theory Tech., **53**, 2956-2967.

[68] Vaughan, J. M., 1989, *The Fabry-Perot Interferometer: History, Theory, Practice, and Applications*, Adam Hilger, Philadelphia, PA.

[69] Born, M., and Wolf, E., 1999, *Principles of Optics*, 7th ed., Cambridge University Press, Cambridge, UK.

[70] Zhang, Z. M., Fu, C. J., and Zhu, Q. Z., 2003, "Optical and Thermal Radiative Properties of Semiconductors Related to Micro/Nanotechnology," Adv. Heat Transfer, **37**, 179-296.

[71] Hu, L., Schmidt, A., Narayanaswamy, A., and Chen, G., 2004, "Effects of Periodic Structures on the Coherence Properties of Blackbody Radiation," J. Heat Transfer, **126**, 786-792.

[72] Ruan, X. L., and Kaviany, M., 2005, "Photon Localization and Electromagnetic Field Enhancement in Laser-Irradiated, Random Porous Media," Microscale Thermophys. Eng., **9**, 63-84.

[73] Palik, E. D., 1991, *Handbook of Optical Constants of Solids II*, Academic Press, Boston.

[74] Boardman, A. D., 1982, *Electromagnetic Surface Modes*, Wiley, New York.

[75] Vlasov, Y. A., Moll, N., and McNab, S. J., 2004, "Observation of Surface States in a Truncated Photonic Crystal Slab," Opt. Lett., **29**, 2175-2177.

[76] Morrison, S. K., and Kivshar, Y. S., 2006, "Tamm States and Nonlinear Surface Modes in Photonic Crystals," Opt. Commun., **266**, 323-326.

[77] Wang, B., Dai, W., Fang, A., Zhang, L., Tuttle, G., Koschny, T., and Soukoulis, C. M., 2006, "Surface Waves in Photonic Crystal Slabs," Phys. Rev. B, **74**, 195104.

[78] Lin, L. L., and Li, Z. Y., 2001, "Interface States in Photonic Crystal Heterostructures," Phys. Rev. B, **63**, 033310.

[79] Tamm, I. E., 1932, "A Possible Kind of Electron Binding on Crystal Surfaces," Phys. Z. Sowjetunion, **1**, 733-746.

[80] Lee, B. J., Fu, C. J., and Zhang, Z. M., 2005, "Coherent Thermal Emission from One-Dimensional Photonic Crystals," Appl. Phys. Lett., **87**, 071904.

[81] Lee, B. J., and Zhang, Z. M., 2007, "Coherent Thermal Emission from Modified Periodic Multilayer Structures," J. Heat Transfer, **129**, 17-26.

[82] Ramos-Mendieta, F., and Halevi, P., 1997, "Electromagnetic Surface Modes of a Dielectric Superlattice: The Supercell Method," J. Opt. Soc. Am. B, **14**, 370-381.

[83] Ho, K. M., Chan, C. T., and Soukoulis, C. M., 1990, "Existence of a Photonic Gap in Periodic Dielectric Structures," Phys. Rev. Lett., **65**, 3152-3155.

[84] Robertson, W. M., Arjavalingam, G., Meade, R. D., Brommer, K. D., Rappe, A. M., and Joannopoulos, J. D., 1993, "Observation of Surface Photons on Periodic Dielectric Arrays," Opt. Lett., **18**, 528-530.

[85] Meade, R. D., Brommer, K. D., Rappe, A. M., and Joannopoulos, J. D., 1991, "Electromagnetic Bloch Waves at the Surface of a Photonic Crystal," Phys. Rev. B, **44**, 10961-10964.

[86] Li, L. F., 1996, "Use of Fourier Series in the Analysis of Discontinuous Periodic Structures," J. Opt. Soc. Am. A, **13**, 1870-1876.

[87] Volokitin, A. I., and Persson, B. N. J., 2001, "Radiative Heat Transfer between Nanostructures," Phys. Rev. B, **6320**, 205404.

[88] Bohren, C. F., and Huffman, D. R., 1983, *Absorption and Scattering of Light by Small Particles*, Wiley, New York.

[89] Yeh, P., 1988, *Optical Waves in Layered Media*, Wiley, New York.

[90] Spitzer, W. G., Kleinman, D., and Walsh, D., 1959, "Infrared Properties of Hexagonal Silicon Carbide," Phys. Rev., **113**, 127-132.

[91] Burstein, E., Chen, W. P., Chen, Y. J., and Hartstein, A., 1974, "Surface Polaritons - Propagating Electromagnetic Modes at Interfaces," J. Vac. Sci. Technol., **11**, 1004-1019.

[92] Kollyukh, O. G., Liptuga, A. I., Morozhenko, V., and Pipa, V. I., 2003, "Thermal Radiation of Plane-Parallel Semitransparent Layers," Opt. Commun., **225**, 349-352.

[93] Gaspar-Armenta, J. A., and Villa, F., 2004, "Band-Structure Properties of One-Dimensional Photonic Crystals under the Formalism of Equivalent Systems," J. Opt. Soc. Am. B, **21**, 405-412.

[94] Palik, E. D., 1998, *Handbook of Optical Constants of Solids*, Academic Press, San Diego, CA.

[95] Marquier, F., Joulain, K., Mulet, J.-P., Carminati, R., Greffet, J.-J., and Chen, Y., 2004, "Coherent Spontaneous Emission of Light by Thermal Sources," Phys. Rev. B, **69**, 155412.

[96] Bauer, S., 1992, "Optical-Properties of a Metal-Film and Its Application as an Infrared Absorber and as a Beam Splitter," Am. J. Phys., **60**, 257-261.

[97] Shen, Y. J., Zhu, Q. Z., and Zhang, Z. M., 2003, "A Scatterometer for Measuring the Bidirectional Reflectance and Transmittance of Semiconductor Wafers with Rough Surfaces," Rev. Sci. Instrum., **74**, 4885-4892.

[98] Richter, K., Chen, G., and Tien, C. L., 1993, "Partial Coherence Theory of Multilayer Thin-Film Optical-Properties," Opt. Eng., **32**, 1897-1903.

[99] Lee, B. J., Khuu, V. P., and Zhang, Z. M., 2005, "Partially Coherent Spectral Transmittance of Dielectric Thin Films with Rough Surfaces," J. Thermophys. Heat Transfer, **19**, 360-366.

[100] Lee, B. J., and Zhang, Z. M., 2006, "Design and Fabrication of Planar Multilayer Structures with Coherent Thermal Emission Characteristics," J. Appl. Phys., **100**, 063529.

[101] Park, K., Lee, B. J., Fu, C. J., and Zhang, Z. M., 2005, "Study of the Surface and Bulk Polaritons with a Negative Index Metamaterial," J. Opt. Soc. Am. B, **22**, 1016-1023.

[102] Rytov, S. M., Kravtsov, Y. A., and Tatarski, V. I., 1987, *Principles of Statistical Radiophysics*, vol. 3, Springer-Verlag, New York.

[103] Sipe, J., 1987, "New Green-Function Formalism for Surface Optics," J. Opt. Soc. Am. B, **4**, 481-489.

[104] Pendry, J., 2000, "Negative Refraction Makes a Perfect Lens," Phys. Rev. Lett., **85**, 3966-3969.

[105] Bashevoy, M., Fedotov, V., and Zheludev, N., 2005, "Optical Whirlpool on an Absorbing Metallic Nanoparticle," Opt. Express, **13**, 8372-8379.

[106] Li, C. F., 2003, "Negative Lateral Shift of a Light Beam Transmitted through a Dielectric Slab and Interaction of Boundary Effects," Phys. Rev. Lett., **91**, 133903.

[107] Lee, B. J., Chen, Y.-B., and Zhang, Z. M., "Confinement of Infrared Radiation to Nanometer Scales through Metallic Slit Arrays," Journal of Quantitative Spectroscopy & Radiative Transfer, accepted.

[108] Yang, M. C., and Webb, K. J., 2005, "Poynting Vector Analysis of a Superlens," Opt. Lett., **30**, 2382-2384.

[109] Fu, C. J., and Zhang, Z. M., 2006, "Nanoscale Radiation Heat Transfer for Silicon at Different Doping Levels," Int. J. Heat Mass Transfer, **49**, 1703-1718.

[110] Arfken, G. B., and Weber, H. J., 2001, *Mathematical Methods for Physicists*, 5th ed., Academic Press, San Diego.

[111] Zhang, Z. M., and Lee, B. J., 2006, "Lateral Shift in Photon Tunneling Studied by the Energy Streamline Method," Opt. Express, **14**, 9963-9970.

[112] Ben-Abdallah, P., 2002, "When the Space Curvature Dopes the Radiant Intensity," J. Opt. Soc. Am. B, **19**, 1766-1772.

[113] Shvets, G., and Urzhumov, Y. A., 2004, "Engineering the Electromagnetic Properties of Periodic Nanostructures Using Electrostatic Resonances," Phys. Rev. Lett., **93**, 243902.

[114] Wang, Z. B., Luk'yanchuk, B. S., Hong, M. H., Lin, Y., and Chong, T. C., 2004, "Energy Flow around a Small Particle Investigated by Classical Mie Theory," Phys. Rev. B, **70**, 035418.

VITA

BONG JAE LEE

Bong Jae Lee attended Seoul National University in Republic of Korea and received his Bachelor degree in the School of Mechanical and Aerospace Engineering in August 2001. He came to the United States of America in August 2002 to pursue his Ph.D. degree in the George W. Woodruff School of Mechanical Engineering at the Georgia Institute of Technology. His research interests include fundamentals of near-field thermal radiation, radiative properties of nanostructured materials, and their application in energy conversion devices. He is a member of the American Society of Mechanical Engineers and the Optical Society of America.